HIGH-RESOLUTION WHOLE-HEART IMAGING AND MODELING FOR STUDYING CARDIAC ARRHYTHMIA

by

Farhad Pashakhanloo

A dissertation submitted to Johns Hopkins University in conformity with the requirements for the degree of Doctor of Philosophy.

Baltimore, Maryland

July, 2016

© 2016 Farhad Pashakhanloo

All Rights Reserved

Abstract

Cardiac arrhythmia is a life-threatening heart rhythm disorder affecting millions of people worldwide. The underlying structure of the heart plays an important role in cardiac activity and could promote rhythm disorders. Accurate knowledge of whole-heart cardiac geometry and microstructure in normal and disease hearts is essential for a complete understanding of the mechanisms of arrhythmias.

This dissertation presents novel structural data at the whole-heart level aimed at advancing knowledge of cardiac structure in normal and infarcted hearts, and at constructing whole-heart computational models. A 3D diffusion tensor MRI (DTMRI) technique was implemented on a clinical scanner to image intact large animal and human hearts with high image quality and spatial resolution *ex vivo*. This method was first applied to reconstruct the 3D myofiber organization in 8 human atria nondestructively and at submillimeter resolution. The findings showed that the main features of atrial anatomy are mostly preserved across subjects despite variability in the exact location and orientation of the bundles. Further, we were able to cluster, visualize, and characterize the distinct major bundles in the human atria. Quantitative analysis of the fiber angles across the atrial wall revealed that the transmural fiber angle distribution is heterogeneous throughout the atria.

We next studied microstructural remodeling in infarcted porcine and human hearts by combining DTMRI with high-resolution Late Gadolinium Enhancement imaging. This enabled us to provide reconstructions of both fiber architecture and scar distribution in infarcted hearts with an unprecedented level of detail, and to systematically quantify the transmural pattern of diffusion eigenvector orientation. Our results demonstrated that the fiber orientation is generally preserved inside the scar but at a higher transmural gradient of inclination angle.

Lastly, we employed the obtained data to generate whole-heart computational models of infarcted hearts with detailed scar geometry and subject-specific fiber orientation. We used these models in simulations to investigate the contribution of the infarct microarchitecture to ventricular tachycardia. The simulation results showed that the reentry circuits traverse thin viable tissues with complex geometries located inside of the infarct. The high resolution of the images enabled 3D reconstruction and characterization of such structures.

Advisors: Elliot McVeigh, PhD and Natalia Trayanova, PhD

Primary Reader: Elliot McVeigh, PhD

Secondary Reader: Natalia Trayanova, PhD

Thesis Committee: Elliot McVeigh, PhD, Natalia Trayanova, PhD, Daniel Herzka, PhD

Acknowledgements

First and foremost, I would like to thank my thesis committee members for their invaluable guidance and support during my PhD years. I would like to express my deep gratitude to Dr. Elliot McVeigh for giving me the freedom to embark on such an interesting path in my PhD, and for his unwavering support, encouragement and scientific insights throughout the years. In addition, my work would not be where it is today if not for Dr. Natalia Trayanova's careful feedback and direction. I would like to thank her for expanding the scope of my work into the realm of computational modeling. Also, I owe a debt of gratitude to Dr. Daniel Herzka for his instrumental input on the imaging section of my research. I would also like to extend my gratitude to my collaborators at the National Institutes of Health, Drs. David Bluemke and Neville Gai, for their continuing support, feedback and resources that were integral to my thesis work. I am also grateful to my collaborators at the Johns Hopkins School of Medicine, Drs. Susumu Mori, Henry Halperin, Hiroshi Ashikaga, Saman Nazarian, Ardivan Kolandaivelu and Michael Schar, for the helpful comments and assistance at different stages of my PhD.

Secondly, I would like to thank the wonderful, intelligent and caring members of the Medical Imaging Laboratory and the Computational Cardiology Laboratory for creating such a great work environment and for the personal and professional support throughout the years.

Lastly, endless thanks to all the friends and family, near and far, for the emotional support, unconditional love and patience and without whom this thesis would be impossible.

Contents

List of Tables

List of Figures

Chapter 1

Introduction and Specific Aims

1.1 Overview

Cardiac arrhythmias are strongly associated with structural remodeling in the heart. However, despite broad clinical and experimental research, the exact mechanisms by which cardiac structure contributes to function are incompletely understood in the normal state, let alone in structural heart disease. This is chiefly due to the fact that the heart is a multi-scale, structurally heterogeneous organ and that electromechanical abnormalities emerge in a complex fashion in space and time. Complete understanding of the structure-function linkage thus necessitates detailed structural data in individual hearts as well as in the population. Such data will be useful not only to advance the current knowledge of cardiac histo-anatomy, but importantly, as a basis for the generation of accurate electromechanical models of the heart. These computational models provide an unparalleled opportunity to uncover mechanistic links between structure and function and could further improve therapeutic approaches such as cardiac ablations.

Cardiac fiber architecture in normal and disease states plays a crucial role in the electrical and mechanical function of the heart. The anisotropic nature of myocardium provides a preferential direction for electrical propagation and directly influences the mechanical strain and stress. In addition, the spatial organization of myofibers in the heart has been shown to be important in the initiation of rhythm disorders in both the ventricles and atria. Diffusion Tensor Imaging (DTI) is a non-destructive tool that utilizes the restricted diffusivity of water molecules to elucidate information regarding the tissue microstructure. DTI has been widely used to explore the fiber architecture in normal and disease ventricles. Accurate assessment of microstructure using DTI necessitates an MR sequence that produces high image resolution and high image quality. This in particular is crucial for imaging regions of the heart with thin walls, complex architecture, and low structural anisotropy, such as atria and infarcted tissue.

Myocardial infarction (MI) or heart attack, is major cause of death affecting millions of people worldwide. Occurrence of MI results in structural remodeling in the infarcted tissue and could eventually lead to heart failure. While the presence of an infarct is associated with an increased risk for ventricular arrhythmia, not all patients with MI have the same risk for arrhythmias. Infarct architecture is an important determinant of electrical abnormalities. In particular, it has been demonstrated that the substrates for ventricular arrhythmias are co-localized with the surviving myocardium surrounding the infarct. These substrates are often targets of cardiac ablation therapy. However, the current techniques to image the infarct geometry and the associated electrical activity are confronted with major limitations. These shortcomings primarily include low spatial resolution of *in vivo* Late Gadolinium Enhancement (LGE) MRI and point-by-point and surface recording of activity using electroanatomical mapping techniques. Computational models of the whole heart with detailed infarct structure could create a valuable framework to study the structural contribution of the infarct to arrhythmia.

The overall goals of this thesis are to provide high-resolution structural data on intact normal and infarcted hearts and to employ that data in multi-scale computational models of the heart to obtain new insight into the mechanisms of scar-related arrhythmias. The new knowledge of cardiac structure and the mechanisms of infarct-related arrhythmia obtained in this thesis could ultimately lead to optimal design of therapies aimed at cardiac arrhythmias and improve the risk stratification for such arrhythmias in patients.

1.2 Specific Aims

The specific aims of this thesis are:

Specific Aim 1: Implement a sub-millimeter 3D diffusion tensor magnetic resonance imaging (DTMRI) technique on a clinical scanner to reconstruct whole-heart fiber orientation in large-animal and human hearts *ex vivo* with improved accuracy than before (chapter 3).

Specific Aim 2: Reconstruct the 3D myofiber architecture in human atria, characterize the major fiber bundles as well as transmural fiber orientation, and assess the inter-subject variability in the fiber structure using the method developed in Aim 1 (chapter 4).

Specific Aim 3: Apply the method developed in Aim 1 in conjunction with high-resolution *ex vivo* LGE-MRI to provide 3D reconstructions of both fiber architecture and scar distribution in intact hearts. Use this data to study the microstructural remodeling in the infarct and test the hypotheses that infarcted tissue has an anisotropic structure, and that the orientations of primary eigenvectors are preserved inside the chronic infarct (chapter 5).

Specific Aim 4: Employ the data obtained in Aim 3 to construct whole-heart computational models of infarcted hearts with detailed infarct geometry and subject-specific fiber orientation. Use these models in simulations to explore the contributions of the infarct geometry and viable tissue to ventricular tachycardia (chapter 6).

Chapter 2

Background and Significance

2.1 Cardiac Anatomy and Electrophysiology

2.1.1 Cardiac Anatomy

The heart is a muscular organ responsible for pumping blood throughout the circulatory system, supplying the body with enough oxygen and nutrients while removing metabolic waste. In humans and other mammals, the anatomy of the heart consists mainly of four chambers: the blood-receiving left and right atria and the blood-discharging left and right ventricles. The left and right chambers are divided by interatrial and interventricular septums. During the normal synchronized contraction of the heart, the blood flows unidirectionally through these chambers. Deoxygenated blood flows from the systemic circulatory system to the right atrium (RA) through the superior and inferior vena cavae. It then passes the tricuspid valve into the right ventricle (RV) where it gets pumped to the pulmonary circulation and the lungs. The oxygenated blood from the lungs returns to the left atrium (LA) via the pulmonary veins and crosses the mitral valve to the left ventricle (LV), before being discharged again to the systemic circulation and the entire body through the aorta. The blood pressure during the discharge phase is the highest in the LV chamber and as a result it contains the thickest wall among the four chambers. By comparison, atria have the smallest wall thickness due to the low blood pressure. Lastly, the heart is enclosed in the pericardium, a sac filled with pericardial fluid that fixes the heart to the mediastinum. The pericardium provides protection against infection, prevents the heart from overexpanding when blood volume increases and provides lubrication for the heart.

overexpanding when blood volume increases and provides lubrication for the heart.

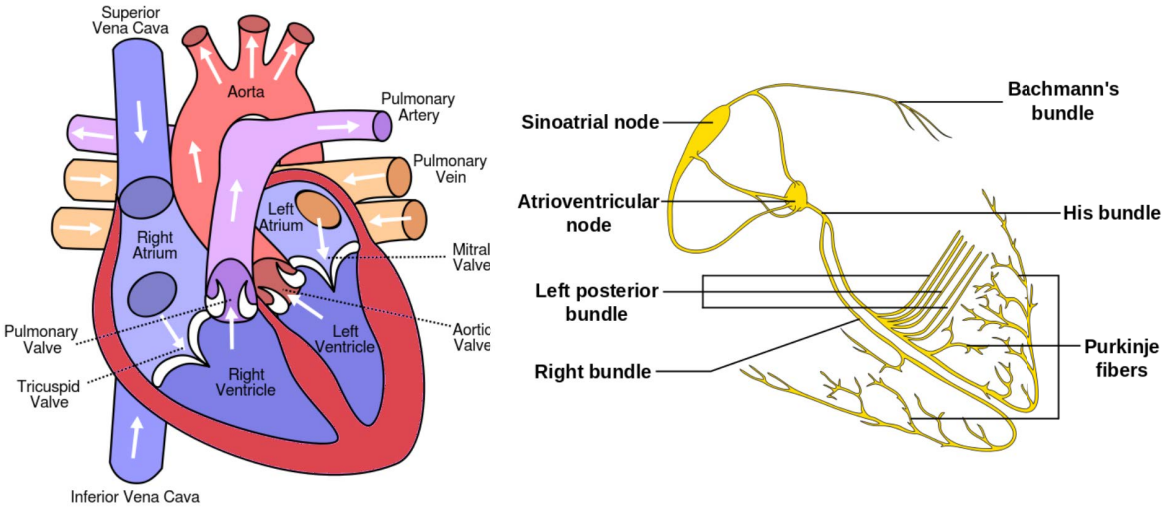

Figure 2.1: Schematic of heart anatomy (left) and conduction system (right). Reused from Wikipedia (https://en.wikipedia.org/wiki/Heart) under the Creative Commons License.

2.1.2 Cardiac Electrophysiology

The synchronous contraction of cardiac muscle is due to the underlying electrical activity in individual cardiac cells. The electrical impulse in the heart is initiated by spontaneous activity of the natural pacemaker cells or sino-atrial (SA) node located at the posterior wall of the right atrium. The spread of electrical activity in the heart occurs through a combination of passive and active electrical propagations. Cardiac myocytes are electrically connected to neighboring cells via gap junctions that passively transmit currents from one cell to another. The electrical activity of a single myocyte, however, is affected by the movement of ions through the transmembrane channels embedded in the cell membrane. This results in the generation of an action potential (AP) waveform that forms the basis for the propagation of electrical activity in the heart. A detailed review of the cardiac action potential can be found here [1]. Subsequent to the initiation of activity at the SA-node, the wave travels throughout the right and left atria and activates the cells at the atrioventricular (AV) node. The AV node is a specialized tissue located

at the posteroinferior region of the interatrial septum, and provides the only conducting pathway between the atria and the ventricles. The ventricles are otherwise electrically isolated from the atria by fibro-fatty tissues. After crossing the AV node, the electrical signal propagates through the specialized Bundle of His and Purkinje fibers to excite the ventricles. The coordinated activation of the heart leads to efficient pumping of the blood to the body.

2.1.3 Myocardial Architecture

It is well known that the muscular architecture of the heart plays a critical role in electrical wave propagation and mechanical force generation. The cardiac tissue structure leads to anisotropic electrical propagation wherein the spread of activation is fastest along the longitudinal axis of the myofiber [2–8]. Myocardial orientation has also been shown to be an important determinant of stress and strain [9–13] and therefore overall function of the heart [14, 15]. Further, the spatially varying fiber orientation in the heart directly influences whole heart activation patterns in normal and disease hearts under a variety of conditions [16–22]. Particularly, the discontinuities and abrupt changes of fiber orientation have been shown to disrupt normal conduction [23], hence promoting ventricular and atrial arrhythmias [19, 24–26].

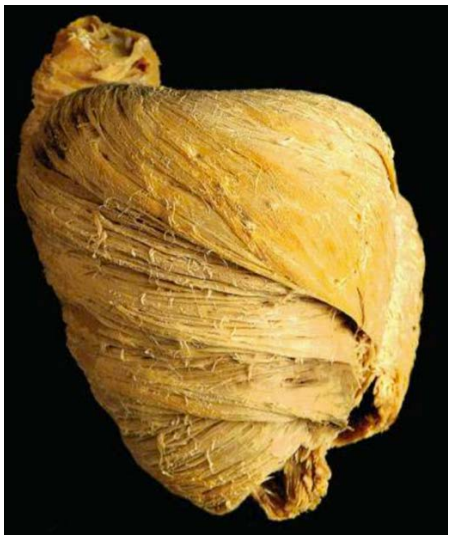

Figure 2.2: Photograph of a porcine left ventricle undergone a careful dissection process to remove the successive layers of the wall. The gradual change of fiber orientation through the wall is clear in this view. Reprinted from Anderson et al [27] with permission from John Wiley and Sons.

The knowledge of fiber architecture in the heart has been traditionally obtained using macrophotography and histological approaches. In the past several years, Diffusion Tensor MRI has been proven to be a powerful tool to image the fiber architecture in the ventricles non-destructively. The myocytes in the left ventricle follow a helical pattern around the chamber with a variable fiber orientation throughout the depth of the wall [28–30]. The fibers of the epicardial and endocardial layers of the wall are aligned obliquely and form angles of around -60° and 60° with the equator, respectively. The transition between the left-handed epicardial fibers and the right-handed endocardial fibers happens smoothly, with the fibers at the midwall being roughly circumferential. Mathematically, it has been shown that the myofiber arrangement in the left ventricle may take the form of a special minimal surface throughout the myocardium [31]. In addition, computational modeling of cardiac mechanics has demonstrated that the fiber architecture of the left ventricle may be optimally organized to achieve a uniform distribution of stress and strain throughout the heart [14].

In comparison to the ventricles, the heart atria demonstrate significant differences in the shape, dimensions, and the level of complexity of the muscular architecture. The atria are comprised of thin walls (averaging 2-3 mm) with non-uniform thickness throughout the chambers [32]. In addition, great variability in the shape and the basic anatomy of the atria has been observed in the human population. This includes inter-subject variability in the number and configuration of pulmonary veins in the left atrium [33, 34]. The muscular architecture in the atria has a complex organization with distinct bundles and structures that run at different orientations, leading to regions of overlapping fibers throughout the chambers. Despite extensive histological studies of atrial anatomy, and unlike that of the ventricles, the systematic characterization of 3D fiber architecture in the atria and its inter-subject variability is missing due to the lack of high-resolution data such as diffusion tensor MRI.

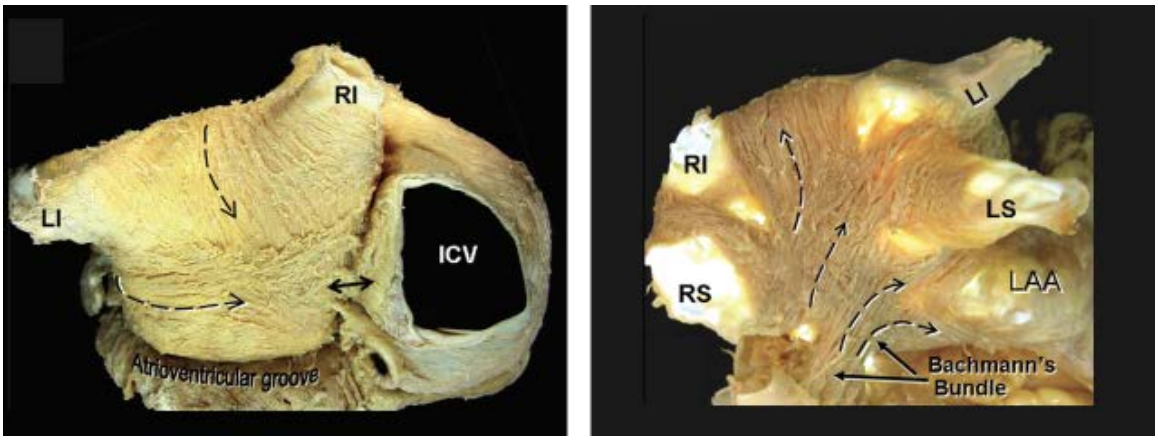

Figure 2.3: Photographs of left human atria demonstrate the atrial gross anatomy and fiber orientation at (A) posterior and inferior wall and (B) roof the left atrium. The figures are reprinted from Ho et al [35] with permission from Wolters Kluwer Health, Inc.

2.2 Cardiac Arrhythmia

2.2.1 Basic Mechanisms

Arrhythmia is a heart rhythm disorder in which the heartbeat is irregular, too slow, or too fast. Arrhythmias that lead to slower heart rates are called bradycardias while those that lead to faster rates are called tachycardias. In general, arrhythmias result from abnormalities in impulse initiation, impulse conduction, or a combination of both [36]. Abnormal impulse initiation can be caused by either automaticity or triggered activity in the heart, while abnormal impulse conduction could lead to reentry. Reentry is a condition in which the excitation travels in a circular path and re-excites the same region more than once. Reentry could have a relatively fixed reentrant pathway and persist to excite the heart at a fast rate. This condition is dangerous because it may not permit the heart to pump enough blood and often degenerates into a chaotic state called fibrillation that involves pathways that continuously change their size and location. Ventricular fibrillation is lethal as the heart loses its ability to pump sufficient blood.

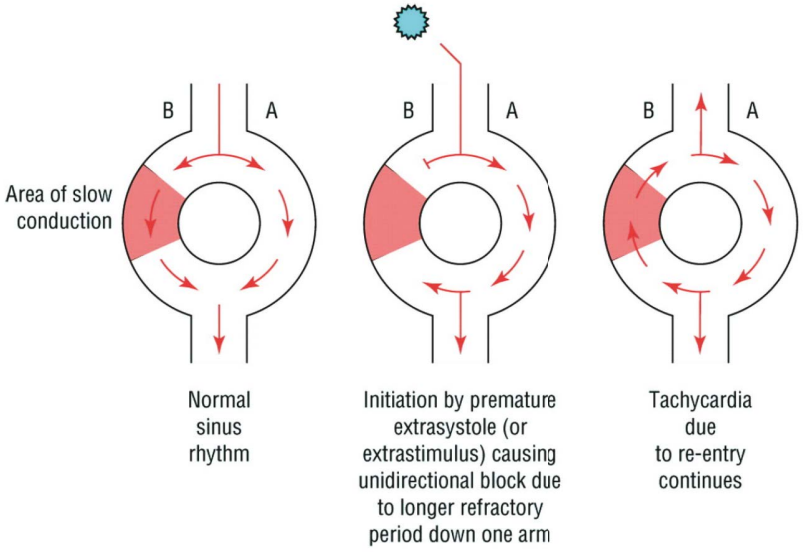

Figure 2.4: Mechanism of reentry circuit. Reprinted with permission from John Wiley and Sons: Grech [37].

Formation of a reentrant circuit requires the presence of a unidirectional block as well as a pathway that produces enough conduction delay for the wave to re-excite the tissue following the refractory phase. The latter condition implies that the pathway be greater than the wavelength, in which the wavelength is the distance traveled by the wave during the functional refractory period. In a normal heart the wavelength is often longer than any regular pathway in the heart. However, in diseased conditions, the wavelength could decrease due to electrophysiological remodeling that leads to conduction slowing, which could further lead to the formation of reentry.

2.2.2 Myocardial Infarction

Myocardial Infarction (MI) or heart attack is a result of blood blockage to the cardiac tissue. Atherosclerosis plaques in coronary arteries are the most common cause of MI. The plaque is the result of gradual buildup of fat, cholesterol, calcium and other substances in the blood that occurs in the arterial wall over time. The presence of plaque in the coronary arteries limits the flow of oxygen-rich blood to the heart. Over time, the plaque could become unstable and break up, which may lead to a clotting cascade that could result in complete occlusion of the artery. If the blood flow obstruction lasts long enough, the tissue downstream of the block at the coronary artery undergoes ischemia. This initiates a complex process of remodeling in the infarcted tissue that starts with inflammation, necrosis, and then subsequent removal of damaged muscle tissue over the following days and weeks. The lost myocytes are then gradually replaced by collagenous scar tissue.

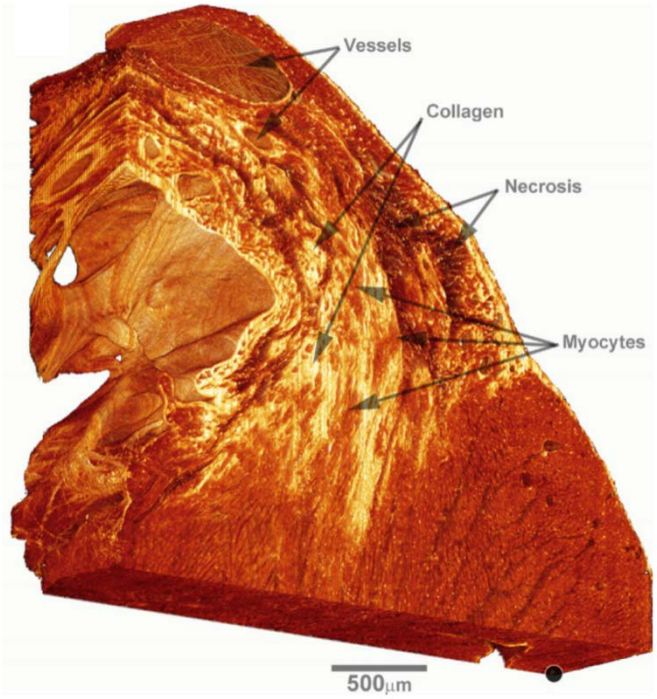

Figure 2.5 Reconstruction of a section of infarct in rat obtained from confocal microscopy. Reprinted with permission from Wolters Kluwer Health, Inc. : Rutherford et al [38].

The infarcted tissue plays an important role in the electrical and mechanical function/dysfunction of the heart post-MI. The scar tissue maintains the integrity of the heart wall even though essentially all of the muscle in the infarcted area is lost [39]. The passive stretching and bulging of the scarred tissue by the surrounding myocardium impairs the overall efficiency of the heart in pumping blood. The structural anisotropy and the mechanical properties of scarred tissue have been shown to be a significant determinant of left ventricular pump function [40–42]. However, the exact relationship between the mechanical and structural properties and cardiac function is not completely understood and is an active area of research [39].

2.2.3 Scar-Related Ventricular Arrhythmias

The presence of infarcted tissue impairs the normal conduction in the heart post-MI, which could result in ventricular arrhythmias. Sustained ventricular tachycardia (VT) is a VT that lasts longer than 30 seconds and/or requires an intervention or leads to severe hemodynamic compromise and other complications [43]. VT is classified as monomorphic if each QRS complex resembles the next. Recurrent monomorphic ventricular tachycardia (VT) is a particularly challenging scenario that cardiologists and electrophysiologists are confronted increasingly in clinical practice. Sustained monomorphic VT occurs most frequently in the setting of healed MI, and may appear in the subacute phase or long after the ischemic injury. Reentry is the mechanism underlying the VT associated with healed or healing MI in more than 95% of the cases [44, 45]. It has been widely demonstrated that slow conduction at the infarcted area could provide substrates for ventricular arrhythmias. Impaired electrophysiological properties observed at the infarct border zone [46] could lead to conduction slowing and block. In addition, it has been shown that the surviving myocardium surrounding the scar could provide tortuous zig-zag pathways for the wave, that effectively leads to conduction slowing and could result in reentry [47].

Radiofrequency ablation [48] is a procedure in which part of the cardiac tissue is ablated using the heat generated from radiofrequency current in the range of 350-500 kHz. In patients with structural heart disease, catheter ablation of VT is used to reduce the frequency of symptomatic ventricular tachycardia that triggers ICD shocks, or to control incessant or very frequent VTs. The guidance of radiofrequency ablation is performed using electroanatomical mapping techniques. Scar-related reentrant VTs can cause hemodynamic instability, which prevents extensive mapping during VT. To avoid hemodynamic collapses, substrate mapping during stable sinus rhythm is often performed to identify the regions of

scar that the arrhythmia originates from [49]. Using voltage maps and electrogram characteristics, these regions can then be detected and subsequently targeted for ablation without inducing VT. In addition, the exit site of the VT may be found by pacing around the scar and finding matches in the observed 12-lead ECG to that of the patient's clinical arrhythmia. The efficiency of cardiac ablation procedures depends on factors such as the location of the circuit (endocardial or epicardial) and the ability to induce VT in the electrophysiology lab [50]. Success rates for terminating clinical VT are close to 70%. However, recurrent VT from other reentrant circuits occurs in up to 50% of the patients over time [50]. The interplay of the activation wavefront and the infarct is a complex 3D phenomenon that occurs across the spectrum of scales ranging from molecular to whole-organ.

2.2.4 Atrial Fibrillation

Atrial Fibrillation (AF) is the most common sustained cardiac arrhythmia and is associated with significant morbidity and cost. The number of patients with AF is likely to double or triple within the next two or three decades [51]. AF is driven by high-frequency electrical activity that leads to desynchronized muscle contraction in the atria. This could further lead to slow blood flow in the atrium, and result in the formation of blood clots. If these blood clots leave the heart and travel to the brain, they can cause a stroke by blocking the blood flow through cerebral arteries. In fact, the presence of AF has been associated with an almost five-fold increase in the risk for stroke [52]. AF has been observed across patients with a variety of conditions including patients without structural heart disease ("lone AF"), patients in the postoperative settings, and patients with significant left ventricular dysfunction and advanced heart failure [53]. The mechanism of AF is not completely understood, but in general the fibrillatory behavior is thought to either be the result of triggered focal activity leading to the collision of multiple wavelets, or the result of spiraling reentrant waves also known as rotors [51]. AF is

clinically classified into different stages: paroxysmal (< 7days), persistent (> 7 days or requiring intervention to restore sinus rhythm), longstanding persistent (> 1 year) or permanent, when restoration of sinus rhythm is no longer followed [53]. At least three main therapeutic approaches are available for patients with AF: (1) drug therapy, (2) catheter ablation, and (3) surgical intervention (maze procedure). Drug therapy usually includes treatments that aim to either control the heart rate (rate therapy) or to restore the normal rhythm (antiarrhythmic therapy). Such therapies have limited efficacy (40-60%), important side effects, and in multiple studies have been shown to be less effective than catheter ablation [53]. There are multiple strategies to terminate AF using radiofrequency ablations [54]. Pulmonary vein isolation is a frequent approach in which circular lesions are created around the base of pulmonary veins to block the spontaneous ectopic beats generated in the veins [55]. Additional lesions may be delivered across the left atrial roof, between the left pulmonary veins and mitral valve, or in the regions of abnormal electrical activity such as complex fractionated atrial electrograms. Overall, the complexity of atrial activation during AF necessitates mechanistic-based approaches that take spatial organization of the structure and electrical activity into account to achieve better outcomes with catheter ablation.

2.3 Computational Cardiac Electrophysiology

The current limitations in recording the electrical activity in the heart have hindered a full understanding of cardiac arrhythmia mechanisms. Computational modeling is a powerful tool to study complex systems such as those found in the biological sciences and including cardiac research. The heart is a multiphysics and multiscale system and over decades sophisticated mathematical models have been employed to describe its behavior. In this section we will briefly review some of the fundamental methods used in mathematical modeling of the electrophysiology in the heart.

2.3.1 Single-Cell Modeling

The main component of modeling electrical activity in the heart involves the behavior of single cardiac cells and the associated action potential waveforms. This usually starts with developing a model of transmembrane currents. The cell membrane is a lipid dielectric that could be modeled as a capacitor. The ion channels embedded in the cell membrane provide pathways for the ions to cross the membrane.

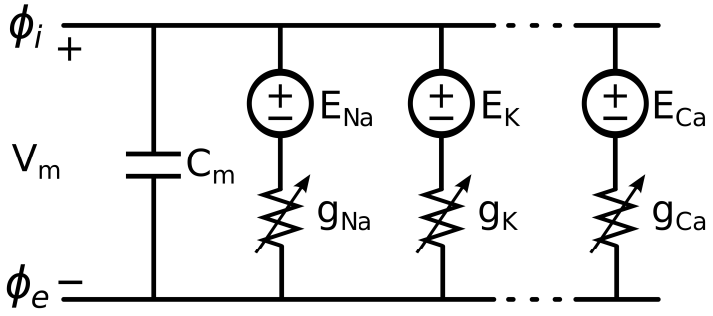

Figure 2.6: The parallel conductance model of single cell. The model consists of a capacitor associated with the membrane current, and the individual ion channels that act like variable conductances in series with equilibrium potentials for the corresponding ions.

Therefore, the total transmembrane current, I_m, can be represented as:

$$I_m = C_m \frac{\partial V_m}{\partial t} + I_{ion} - I_{stim} \tag{2.1}$$

where V_m is the transmembrane voltage $(\phi_i - \phi_e)$, defined as the difference between the intracellular and the extracellular potentials, C_m is the membrane capacitance per unit area, I_{ion} is the current density flowing through the ionic channels, and I_{stim}, if present, is the transmembrane stimulus current density as delivered by the intracellular electrode [56]. While he complexity of the chosen ionic model heavily depends on the application and the computational power, the most important ion channels are Na^+, K^+ and Ca^{2+}.

2.3.2 Modeling the Electrical Propagation in Tissue

The propagation of AP in cardiac tissue is facilitated by gap junctions that provide conduction pathways between the neighboring cells. This propagation can be represented by the bidomain model [57] that is a generalization of one-dimensional cable theory. The bidomain formalism is a continuum model meaning that it represents the average properties of many cells, as opposed to discrete models that describe each cardiac cell individually [58]. The bidomain model assumes the presence of intracellular and extracellular domains at each point in space. It consists of two coupled reaction-diffusion equations that represent the behavior of intracellular and extracellular potentials that are coupled by the membrane current:

$$\nabla.(\sigma_i \nabla \phi_i) = \beta I_m \tag{2.2}$$

$$\nabla.(\sigma_e \nabla \phi_e) = -\beta I_m$$

where σ_i and σ_e are respectively the intracellular and extracellular conductivity tensors and β is the surface to volume ratio of the cardiac cells. The media by themselves are linear, however the non-linearities arise from the current-voltage relationships across the membrane (Equation 2.1) and could be described by a set of non-linear ordinary differential equations (ODE).

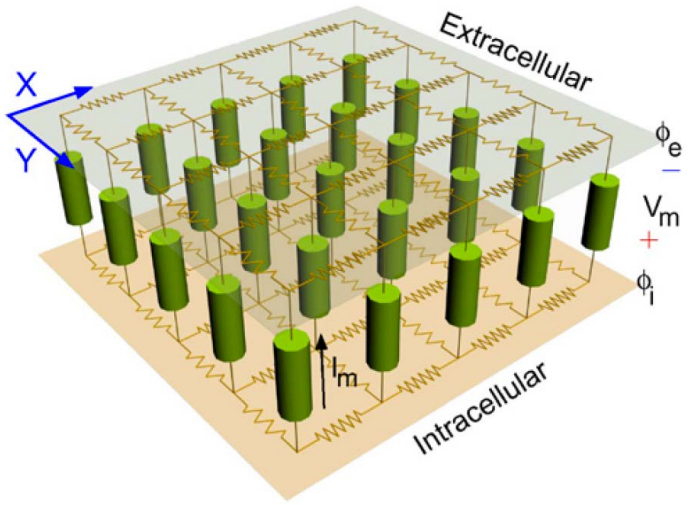

Figure 2.7: Bidomain representation of cardiac tissue in 2D. Reprinted from Vigmond et al [59] with permission from Elsevier.

The anisotropy of conduction due to myofiber and myolaminar orientations could be incorporated in the conductivity tensors. If either the extracellular electric field can be ignored, or the ratios of the longitudinal and transverse conductivities in the intracellular and extracellular spaces are equal, the above bidomain equations could be simplified to the monodomain equation [56, 60]:

$$\nabla.(\sigma_m \nabla V_m) = \beta I_m \tag{2.3}$$

where V_m is the transmembrane voltage, and $\sigma_m = \sigma_i(\sigma_i + \sigma_e)^{-1}\sigma_e$ is the monodmain conductivity tensor. It has been demonstrated that the mondomain formulation could reasonably approximate the electrical activity in the heart, with significantly less computational expenses than those associated with the bidomain model [60]. Finally, the governing monodomain or bidomain equations could be solved using finite element methods on a spatially discretized version of the heart [59].

2.4 Cardiac Imaging

2.4.1 Magnetic Resonance Imaging

Magnetic Resonance Imaging (MRI) is a non-invasive imaging technique widely used in biomedical research and clinical settings. MRI is capable of providing exceptional soft tissue contrast in the body's organs such as the brain, liver and heart. The basic principle of signal detection in MRI relies on the absorption and emission of radiofrequency (RF) energy by the atomic nuclei in the presence of an external magnetic field. The majority of the research and clinical MRI techniques use the hydrogen atoms naturally present in the water molecules inside the body to generate a radiofrequency signal. Typical MRI hardware consists of an MRI magnet to provide a strong static magnetic field, radiofrequency coils responsible for transmitting and receiving the signal from the object, and gradient coils to create a spatially variant magnetic field.

The generation of spatial images in MRI involves manipulation of nuclear magnetic spins present in the object using an external field. While the detailed interaction of the spins with other spins and the external field lies in the realm of quantum physics, macroscopic phenomenological models of spin magnetization are usually sufficient to describe such interactions in the context of MR pulse sequence design. At the equilibrium state, the magnetic spins are aligned with the direction of the external static magnetic field. The application of RF signal at the resonant Larmor frequency (127.74 MHz for a hydrogen atom in a 3 Tesla magnet) excites the spins and transfers them from a low-energy state to a high-energy state. Upon the termination of the RF signal, the spins return to their original state. This process generates time-varying changes in the magnetic flux at the receiver coil and gives rise to the MR signal. Since the precession frequency of the spins is linearly related to the local magnetic field, the application of a spatially varying magnetic

field using the gradient coils encodes the spins with their spatial location. The received signal therefore contains spatially encoded information from all across the object. An image domain signal can be generated by the application of an Inverse Fourier transform on the detected signal. By varying the parameters of the imaging sequence, different contrasts can be generated from the tissue. This makes MRI a highly versatile imaging modality in providing anatomical and functional details regarding the tissue under study.

2.4.2 Diffusion Weighted Imaging

Diffusion imaging is an MR-based imaging technique that utilizes the diffusion of water molecules to probe the microstructure of the tissue. The random movement of particles in a fluid or gas is referred to as Brownian motion and was first mathematically characterized by Einstein in 1905. The average diffusion distance of freely moving particles in a time interval is governed by the following equation:

$$< \Delta r^2 > = 6D\Delta t \tag{2.4}$$

where $< \Delta r^2 >$ is the average squared displacement of particles allowed to diffuse freely in the time interval Δt. Here D is the diffusion coefficient that depends on the temperature. At the room temperature (25°C), the self-diffusion coefficient of water is approximately 2.3×10^{-3} mm^2/s. If the water molecules were allowed to diffuse freely in the interval of $\Delta t = 50$ms (a typical measurement interval in diffusion imaging), their root-mean-square displacement would be about 26 μm. However, in a biological tissue such as cardiac tissue the dimensions of subcellular and extracellular spaces are on the order of several micrometers. This suggests that in typical diffusion MR imaging, the diffusion of water molecules is most likely impeded by cell membranes and other subcellular and extracellular obstacles. It is indeed due to the measurement of this impeded diffusivity by which diffusion

imaging is capable of probing the underlying structure in the tissue.

Diffusion MR measurement is based on the attenuation of MR signal after the application of strong diffusion sensitizing gradients. The schematic in Figure 2.7 demonstrates the basic principle that the random movement of water molecules could lead to signal attenuation in the presence of conventional Stejskal and Tanner unipolar diffusion gradients.

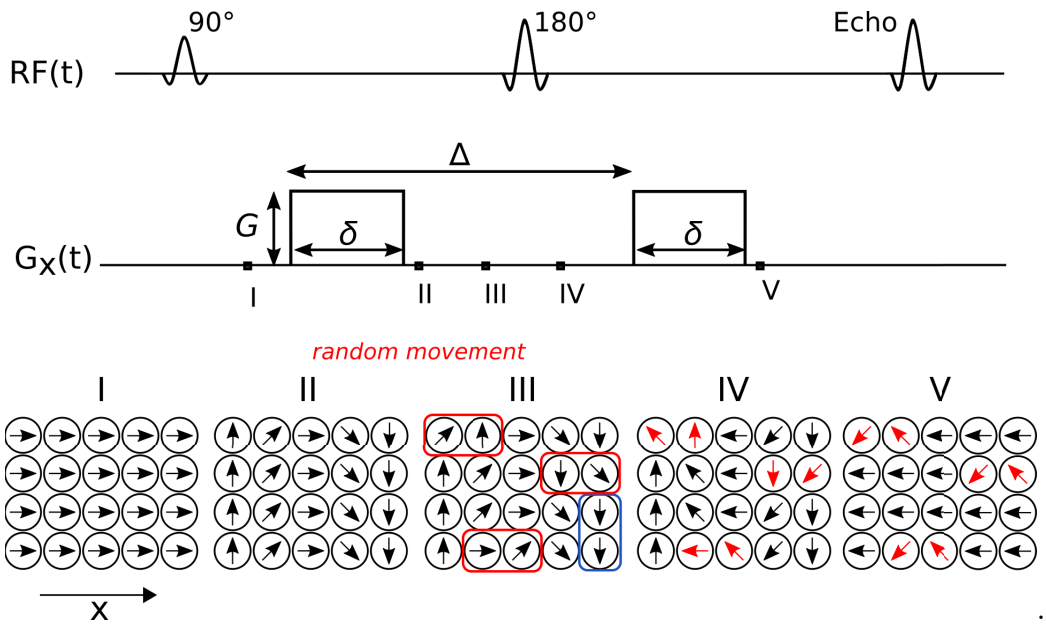

Figure 2.8: The effect of random molecular motions in the presence of a bipolar diffusion gradient. Immediately after the application of 90° RF pulse, the spins are coherently aligned (I). The first diffusion gradient de-phases the spins linearly along X (II). The random movement of the water molecules in the interval between II and III is here demonstrated by switching the location of 4 adjacent spin pairs as highlighted by the red and blue boxes. IV and V represent the time-points after the 180° and the re-phasing diffusion pulses respectively. The red spins that have undergone random movements along the gradient direction (X) do not completely return to the original state. This leads to an incoherent spin arrangement at the echo time and therefore leads to MR signal attenuation.

The signal attenuation could be described with the following equation:

$$S = S_0 e^{-bD} \tag{2.5}$$

where S is the intensity of the diffusion-weighted signal, S_0 is the non-diffusion-weighted signal that is generated using the same pulse sequence but with no diffusion-sensitizing gradients, b or b-value is a parameter that represents the extent of the applied diffusion weighting and depends on the timing, shape and the strength of the diffusion pulses and finally D is the effective diffusion coefficient. For a particular diffusion sequence, the b-value can be represented as:

$$b = \int_0^{T_E} k(t').k(t')\,dt' \tag{2.6}$$

where T_E is the echo time and $k(t)$ is the time-integral of the gradient waveforms:

$$k(t) = \gamma \int_0^t G(t')\,.\,dt' \tag{2.7}$$

For a standard rectangular bipolar diffusion gradient (Figure 2.8), the b-value can be calculated as

$$b = \gamma^2 G^2 \delta^2 [\Delta - \tfrac{\delta}{3}] \tag{2.8}$$

Therefore, D can be estimated by repeating the experiment with two different b-values:

$$D = \frac{1}{(b_2 - b_1)} \ln \left[\frac{S(b_1)}{S(b_2)}\right] \tag{2.9}$$

Often one of the b-values is set to zero, in which case b_1=0 and $S(b_1) = S_0$.

2.4.3 Diffusion Tensor Imaging

In the presence of anisotropic structure, as in the case of skeletal or cardiac muscle, the water diffusivity is not isotropic. The effective diffusivity could be represented as the second-order self-diffusion tensor **D** [61].

$$\boldsymbol{D} = \begin{bmatrix} D_{xx} & D_{xy} & D_{xz} \\ D_{yx} & D_{yy} & D_{yz} \\ D_{zx} & D_{zy} & D_{zz} \end{bmatrix} \tag{2.10}$$

The equations representing the relationship between the signal intensity and the effective diffusivity can be generalized as:

$$\ln\left(\frac{S_0}{S}\right) = \sum_{i=1}^{3}\sum_{j=1}^{3} b_{ij}D_{ij} \tag{2.11}$$

$$b_{ij} = \gamma^2 \int_0^{T_E} \left(\int_0^{t'} G_i(t'')dt''\right).\left(\int_0^{t'} G_j(t'')dt''\right)dt'$$

where i and j relate to any of the gradient directions [x,y,z]. The diffusion tensor is symmetrical i.e. $D_{ij} = D_{ji}$, therefore there are only 6 unique values in the tensor. Given this, measurements along at least 6 non-colinear diffusion gradient directions is required in addition to b=0 to determine the diffusion tensor. The acquisition of more diffusion directions leads to an over-determined system of equations and could improve the tensor estimation.

Subsequent to the calculation of the diffusion tensor, each voxel is assigned a tensor with 6 independent values that include diffusivity terms along x,y,z (i.e. D_{xx}, D_{yy}, D_{zz}) and the non-diagonal elements. Switching from the image-based coordinate system to a tissue-based frame is an efficient way to interpret the information. Mathematically, this is equivalent to diagonalization of the diffusion tensor [62]:

$$\boldsymbol{D}\vec{e}_i = \lambda_i\vec{e}_i \,, i = 1,2,3 \tag{2.12}$$

in which the eigenvalues $[\lambda_1, \lambda_2, \lambda_3]$ $(\lambda_1 \geq \lambda_2 \geq \lambda_3)$ represent the diffusivity values along the tissue-based orthogonal axes as determined by the eigenvectors orientation $[\vec{e}_1, \vec{e}_2, \vec{e}_3]$. The eigenvectors could be utilized to explore the anisotropic orientation of the tissue. In the myocardium, the first eigenvector has been shown to coincide with local myofibers [30]. The second and third eigenvectors determine the orientation of laminar structures of the cardiac tissue [63, 64]. Scalar invariant

quantities could also be derived from the diffusion tensors; these values are invariant to the choice of image coordinate system. Mean diffusivity can be defined as below:

$$MD = \bar{\lambda} = \frac{\lambda_1+\lambda_2+\lambda_3}{3} = \frac{D_{xx}+ D_{yy}+ D_{zz}}{3} \tag{2.13}$$

In addition, Fractional Anisotropy (FA) is a useful measure that represents the degree of diffusion anisotropy in a tissue:

$$FA = \sqrt{\frac{3}{2}.\frac{(\lambda_1-\bar{\lambda})^2+(\lambda_2-\bar{\lambda})^2+(\lambda_3-\bar{\lambda})^2}{{\lambda_1}^2+{\lambda_2}^2+{\lambda_3}^2}} \tag{2.14}$$

FA value of 1 corresponds to an idealized anisotropic diffusivity, and FA of 0 represents a complete isotropic diffusion. In a highly anisotropic tissue in the human body such as brain white matter, FA could reach 0.7. In a normal human heart FA~0.4 has been reported.

Chapter 3

High-Resolution 3D Diffusion Tensor Imaging to Reconstruct Whole-Heart Fiber Orientation in Large Animal and Human Hearts *ex vivo*

3.1 Introduction

The imaging of large animal and human hearts that is required for accurate reconstruction of fiber architecture demands an MR pulse sequence that produces images with high resolution, high signal-to-noise ratio (SNR) and few image artifacts. To achieve these goals one is confronted with several trade-offs arising from fundamental MR physics as well as practical limitations such as total scan duration and cost. A major physical trade-off comes from the fact that image SNR is positively related with imaging voxel size and total scan duration; SNR deteriorates as the spatial resolution increases, and it improves at longer scan times. The increased scan time could present additional technical challenges such as instability in the sample's physical condition (e.g. position and temperature) and in the MR imaging hardware, not to mention the increase in the cost associated with the scan. Adoption of fast imaging techniques with the goal of shortening the total scan time could generally lead to unwanted image artifacts.

In addition to the imaging parameters directly influencing the image resolution, quality and SNR, accurate reconstruction of diffusion tensors demands optimal strategies in regard to the selection of DTI-specific parameters. These parameters should be taken into account for the optimization of the overall imaging sequence and include: the extent of diffusion sensitivity determined by the strength and the timings of the diffusion gradients, the number of diffusion directions, and the angular distribution of diffusion gradients. Finally, another major constraint comes from the fact that whole-heart imaging of intact large animal and human hearts is not possible in high magnetic field animal scanners with small bore dimensions. Therefore, the imaging needs to be performed on scanners with large bores such as a clinical scanner to accommodate the whole heart.

In this chapter we will present the methodology developed in this thesis to

reconstruct fiber architecture in large animal and human hearts using *ex vivo* 3D DTI, along with the results obtained from this technique.

3.2 Pulse Sequence Design

A diffusion-weighted pulse sequence is mainly comprised of a diffusion preparation phase followed by an imaging phase. While the former sensitizes the signal to water diffusivity in a particular direction, the latter is responsible for spatial encoding and acquisition of the signal. We implemented a customized 3D Fast Spin Echo sequence with two symmetric unipolar diffusion pulses around a 180° refocusing pulse, as first proposed by Stejskal-Tanner (ST). This diffusion pulse scheme has the advantage of having the highest diffusion sensitization factor (b-value) given a total diffusion time and maximum gradient strength, and therefore reduces the echo time (TE) given a fixed b-value. Achieving minimal TE is particularly important for cardiac tissue with a high signal decay rate due to a short T_2. The ST diffusion pulses are most frequently used in *ex vivo* experiments, when there is no motion present in the object. Other diffusion schemes such as Stimulated Echo and an asymmetric twice-refocused version of ST are less sensitive to the bulk motion and therefore are mostly used in imaging of the beating heart.

The 3D Spin Echo (SE) sequence is the most advantageous choice for the imaging part of the pulse sequence in terms of SNR and image artifact. Other fast imaging techniques such as EPI are more prone to distortions in the presence of eddy currents, chemical shift, B0-field inhomogeneity and off-resonance effects due to magnetic susceptibility variations (e.g. tissue- air/liquid interface). The majority of the clinical diffusion imaging is performed in 2D or multi slice scheme. Although such methods could provide improved scan time by imaging a section of the heart, they suffer from lower SNR and produce image artifacts due to slice-cross talk or slice selection profile. Therefore, 3D imaging sequence is necessary to avoid such

artifacts and to achieve high image SNR and quality. We therefore used a 3D Fast Spin Echo DTI sequence on a Philips clinical scanner (3T Achieva TX; Philips Healthcare, Best, the Netherlands). In order to implement this sequence we used pulse-programming approach to modify the existing 2D Spin Echo diffusion sequence on the scanner. The schematic of the customized pulse sequence in this thesis is presented in Figure 3.1.

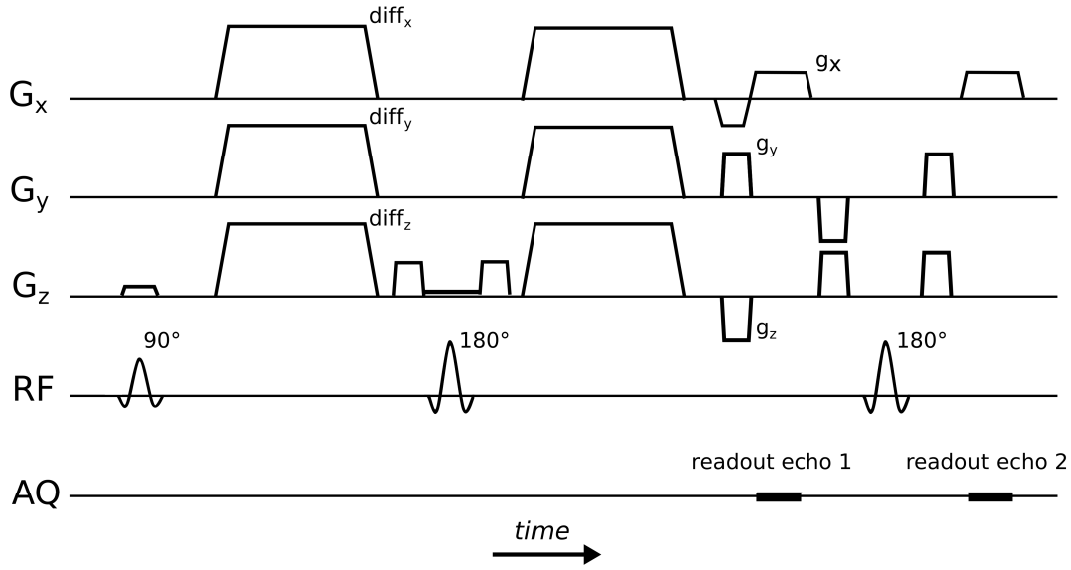

Figure 3.1: Schematic of the 3D diffusion-weighted Fast Spin Echo pulse-sequence used to measure fiber structure in all the hearts in this thesis.

The signal readout was performed using two acquisition echoes. Each echo covered the k-space with full coverage along kx and ky axes and partial coverage in kz direction. The partial scan factor (PSF) determines the ratio of kz-dimension that is covered by each echo and varied from 0.6 to 1 for different experiments. The echoes had opposite kz polarities and both covered the k-space center. Therefore, for a given PSF, the kz coverage interval of each echo was: $kz_1 = [-1{,}2(PSF - 0.5)].k_{max}$ and $kz_2 = [-2(PSF - 0.5), 1].k_{max}$ in which kz_1 and kz_2 represent the k-space coverage intervals for echo 1 and echo 2 respectively and k_{max} is the maximum kz value in k-space ($PSF = 1$ leads to the full coverage of k-

space by both echoes). The short T_2 of the myocardial tissue fixed in formaldehyde (~40ms) did not justify using a higher number of echoes in the sequence. Finally, the imaging parameters were optimized to image a whole animal or human heart (average dimension of a human heart ~ 6x9x12 cm^3) over 40-60 hours of scan time at a sub-millimeter resolution. In preliminary design of the pulse sequence, we found, through trials, that diffusion gradient amplitudes and imaging gradients needed to be adjusted to a level that was below the maximum capability of the scanner in order to achieve long-term stability. Imposing these constraints limited the achievable diffusion b value and spatial resolution, and added to the scan duration by increasing the minimum Repetition Time (TR). The duty cycle of the final sequence was < 15%. The imaging parameters specific to each imaging application are provided in future chapters, but typical values (for whole human heart imaging) include: TE = 60 ms, TR = 625 ms, bandwidth = 289.8 Hz per pixel, number of echoes = 2, partial echo factor = 0.6, diffusion gradients duration = 22.9 ms, time gap between diffusion pulses = 12.5 ms, maximum gradient strength = 60 mT/m, number of diffusion encoding directions = 15, maximum b value = 800 s/mm^2 , field of view: 110×90×120 mm^3 (covering the whole heart), acquired voxel dimension = 0.5×0.5×1.0 mm^3 and reconstructed voxel dimension = 0.4×0.4×0.4 mm^3.

3.3 Image Reconstruction and Tensor Calculation

The raw MRI data was exported from the scanner and a customized image reconstruction was performed offline in MATLAB (The MathWorks Inc, Natick, MA). The reconstruction took advantage of two echoes to increase the SNR; images from each echo were reconstructed separately and were averaged in image-space. In the case of partial echo (PSF<1), a 3D homodyne reconstruction method was used to reconstruct the full 3D image for each echo. Prior to the diffusion tensor calculations, the images were interpolated to an isotropic voxel size using

zero-padding. Figure 3.2 presents short-axis views of non diffusion-weighted image (b0) and a diffusion-weighted image acquired using the developed DTI sequence in a normal porcine heart. The myocardial SNR, the ratio of the mean signal to the Gaussian converted (x0.65) standard deviation of the background noise in the b0 image was ~120.

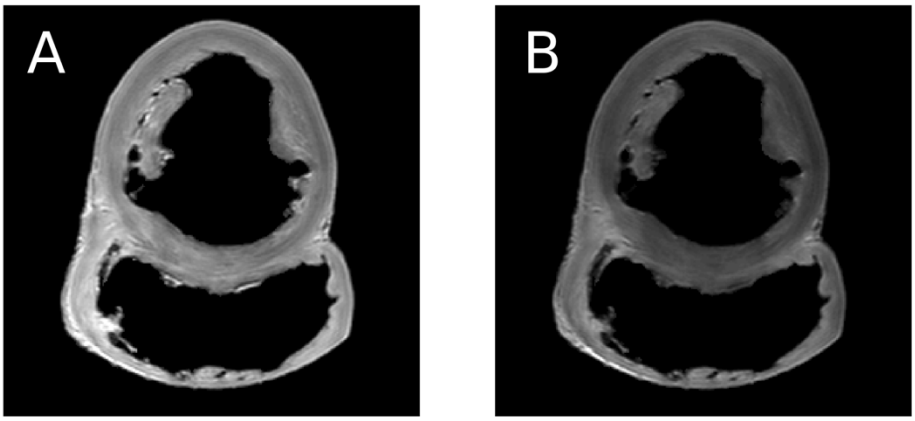

Figure 3.2: Short-axis slices of **(A)** the non-diffusion weighted image (b0) and **(B)** a diffusion-weighted image in a normal porcine heart.

From the 15 diffusion-encoded images and the b0 image, diffusion tensors were calculated using DTI Studio [65] software. Subsequently, tensor diagonalization was performed in MATLAB to calculate diffusion eigenvectors and eigenvalues. Primary eigenvectors were used to obtain the fiber orientation.

3.4 Fiber Angle Measurement

The primary diffusion eigenvector angles were measured in a local coordinate system that is tangential to the LV endocardial surface (Figure 3.3). The three orthogonal axes (unit vectors) of this coordinate system $\mathbf{n}$, $\mathbf{t}$ and $\mathbf{f}$ were defined as follows: $\mathbf{n}$: the normal vector to the endocardial surface, $\mathbf{t}$: circumferential axis, such that $\mathbf{t} = \mathbf{n} \times \mathbf{z}$ (where $\mathbf{z}$ is the longitudinal axis of the heart that is directed from apex to base), and $\mathbf{f} = \mathbf{n} \times \mathbf{t}$. As demonstrated in Figure 3.3, the orientation

of the primary eigenvector could be uniquely determined by two fiber angles measured in this coordinate system. The inclination angle was defined as the angle between the projection of the primary eigenvector onto the tangential plane (plane made up by $\mathbf{t}$ and $\mathbf{f}$) and the local circumferential axis ($\mathbf{t}$). Likewise, the imbrication angle was defined as the angle between the circumferential axis ($\mathbf{t}$) and the projection of the eigenvector onto the plane defined by $\mathbf{t}$ and $\mathbf{n}$. In a normal LV wall, the inclination angle changes smoothly from the epicardium with fibers having negative inclination angle (aka left-handed fibers) to the endocardium with fibers having positive inclination angle (aka right-handed fibers). The circumferentially running fibers at the midwall have an inclination angle close to zero. In addition, imbrication angle is, on average, close to zero in a normal LV wall. Inclination and imbrication angles were measured at all myocardial voxels throughout each heart. For the purpose of visualization the vector field associated with the primary eigenvector was rendered in TrackVis and the fibers were color-coded using inclination angles.

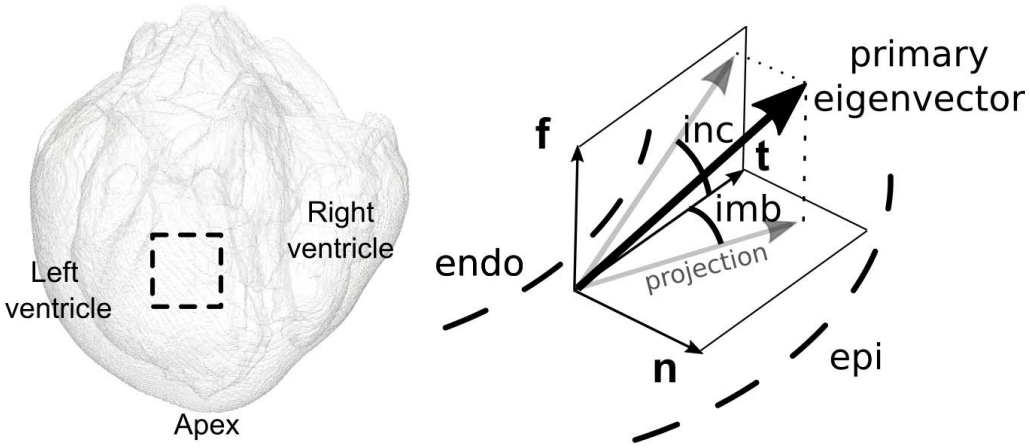

Figure 3.3: Measurement of primary eigenvector angle in a local heart coordinate system that is tangential to the endocardial surface. The inclination angle (inc) is defined by projecting the eigenvector onto the tangential plane formed by vectors $\mathbf{f}$ and $\mathbf{t}$. Similarly the imbrication angle (imb) is measured by projection onto the plane defined by $\mathbf{n}$ and $\mathbf{t}$.

3.5 Fiber Tractography

For the purpose of visualization, fiber tracking was performed on the principal eigenvector using the Fiber Assignment by Continuous Tracking algorithm (FACT) in DTI Studio [65]. This algorithm works by growing tracts from the center of individual voxels in such a way that the local orientation of the tracts coincides with the local eigenvector axis. This process is performed for all the voxels with FA greater than a user-defined threshold (starting criteria). The tracts are terminated if either the voxel FA value falls below the user-defined stopping threshold, or the angle between two eigenvectors to be connected is greater than a user-defined angle threshold (angle deviation). Tractography has been used extensively in brain research to elucidate the anatomical connectivity in the white matter [66]. In the heart, the resulting tracts are a macroscopic manifestation of fiber architecture and are locally aligned with the myofibers. Notably, despite the usefulness and efficiency of the tractography method to visualize and explore the organ level fiber architecture in the heart, the single tracts do not have a physical embodiment in the myocardial tissue. This needs to be considered for an accurate interpretation of tractography results.

3.6 Validation Using Phantoms

To assess the accuracy and the precision of the diffusion estimates obtained from the DTI sequence, we performed an experiment with a circular DTI phantom previously constructed by winding polyamide fibers around an acrylic glass spindle [67]. This phantom was imaged consecutively three times with the following imaging parameters: acquired resolution = 1.15×1.15×1.20 mm^3, TE = 62 ms, TR = 536 ms, b-value = 1000 s/mm^2, number of diffusion directions = 15, scan duration for each acquisition = ~15 hours, total continuous acquisition time for three scans = ~45 hours. Figure 4.4 presents the fiber orientation maps obtained

from the DTI sequence in this phantom, indicating that the eigenvectors have circular orientation (Figure 3.4A) and virtually run in the xy-plane (Figure 3.4B) with a very low out-of-plane angle in the image (median = 0.40°, 25-75% percentile = [0.13, 0.91]°).

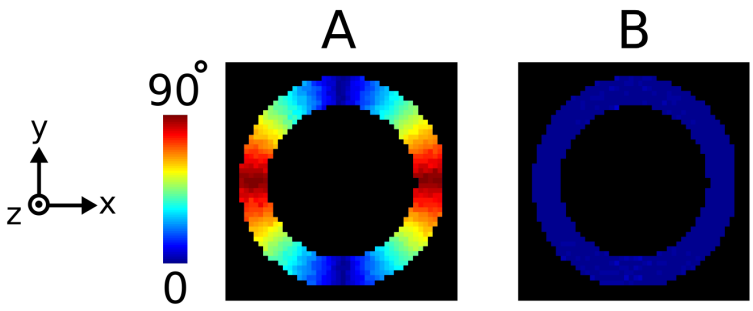

Figure 3.4: DTI results in a circular phantom. The tensors are reconstructed from the first (of three) image acquisition. **(A)** In-plane angle (angle between the projection of eigenvectors onto the xy-plane and the x-axis, i.e. blue: horizontal, red: vertical) and **(B)** out-of-plane angle (angle between the eigenvectors and the xy-plane).

Further, to determine the uncertainty in the estimation of the diffusion eigenvectors, a bootstrapping method was performed on the data retrospectively [68]; from all the diffusion volumes (total of 15×3=45 DWs and 1×3=3 b0s volumes), N=1000 bootstrap datasets (b0 + 15DWs volumes) were created by random selection of the volumes (with replacement). At each voxel, the average primary eigenvector from all the bootstraps was calculated using the dyadic tensor approach [68]. This method handles the problem of antipodal symmetry, i.e. the diffusion eigenvectors do not contain directional information and are only defined along their axis. Further to quantify the dispersion of eigenvectors around the calculated mean eigenvector, the 95% confidence interval (CI) of the minimum angle between the individual eigenvectors and the average eigenvector was calculated. The 95% CI in fiber orientation over the image slice had a median value of 2.3° (25-75% percentile = [1.8, 3.0]°).

In addition to the cylindrical phantom experiment, the stability of the imaging system over the long duration scan was assessed in a porcine heart imaged at a sub-millimeter resolution. The b0 (non-diffusion weighted) images were acquired at the beginning ($b0_1$, t=0 hours) and the end of the scan ($b0_2$, t=~50 hours) in this heart. These two image stacks were compared for spatial registration and SNR consistency. Further, two separate DTI tensors were reconstructed from these data using first, the $b0_1$ volume with the 15 diffusion-weighted images, and second, the $b0_2$ as the non-diffusion weighted volume. The resulting angle difference in the fiber orientation reconstructed using $b0_1$ and $b0_2$, was insignificant inside the myocardium (<0.25 degrees), indicating that there was virtually no effect of the long scan duration on the acquired images.

3.7 Results in Large Animal and Human Hearts

Figure 3.5 presents the fiber orientation maps in a normal porcine heart. The images are color-coded with the longitudinal component of the primary eigenvector (v_z) to distinguish the epicardial, circumferential and endocardial fibers. As demonstrated in the figure, the papillary muscles and the trabecular structures in the heart have primarily longitudinal (apex-to-base) orientation. Figure 3.6 presents the fiber tractography visualizations of the same porcine heart.

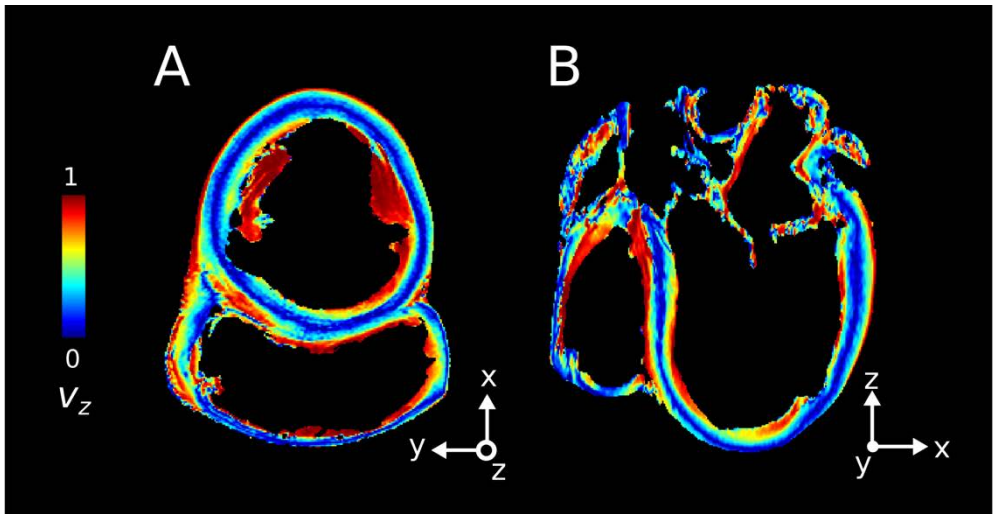

Figure 3.5: Fiber orientation maps in a normal porcine heart in a **(A)** short-axis and **(B)** long-axis slices. The voxels are color-coded based on the z-component of the primary eigenvector (v_z), i.e. red is longitudinal (apex to base) and blue is circumferential orientation.

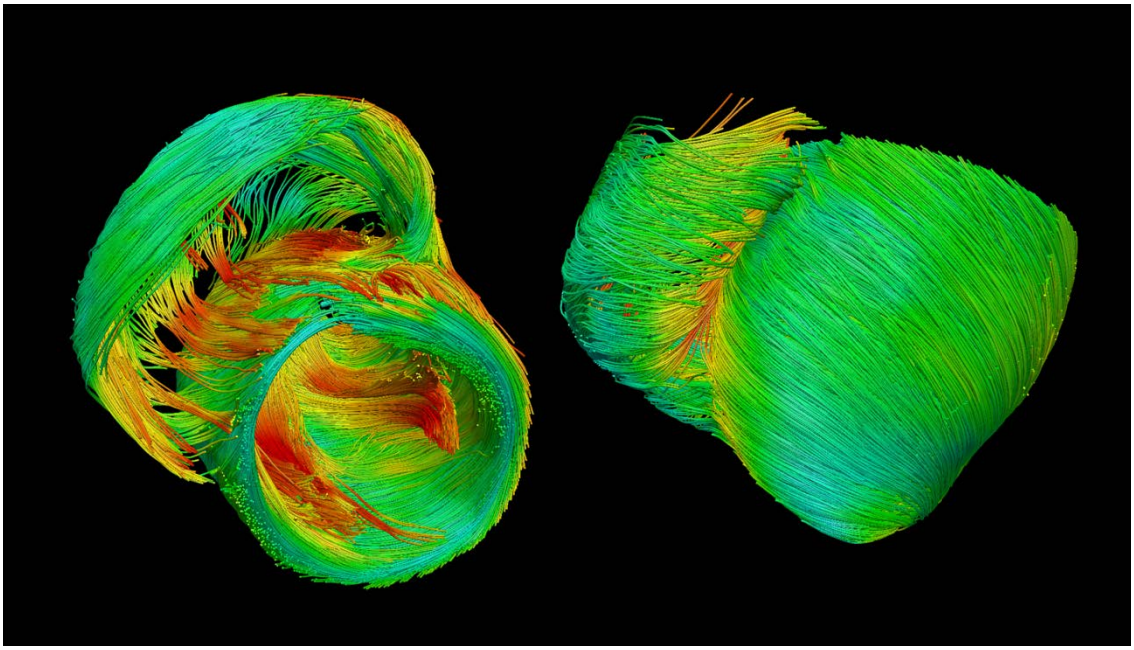

Figure 3.6: Fiber tractography visualizations in a normal porcine heart. Left: view from the base to apex represents the longitudinally-running papillary muscles and trabecular structures distinguishable by yellow and red colors. Right: the anterior view demonstrates the oblique left-handed fibers at the epicardium of LV.

This technique was further applied to multiple species to generate high-resolution datasets of whole-heart fiber orientation in normal and diseased hearts. Figure 3.7 illustrates the eigenvector maps in canine, porcine and human heart LVs. The fibers are color-coded with the inclination angle calculated as described in Section 3.4. The canine datasets generated here were used in multiple studies to perform image-based reconstructions of ventricular geometry [69] and myocardial infarction [70], and to estimate ventricular fiber orientation in infarcted hearts [71] for patient-specific modeling of cardiac electrophysiology.

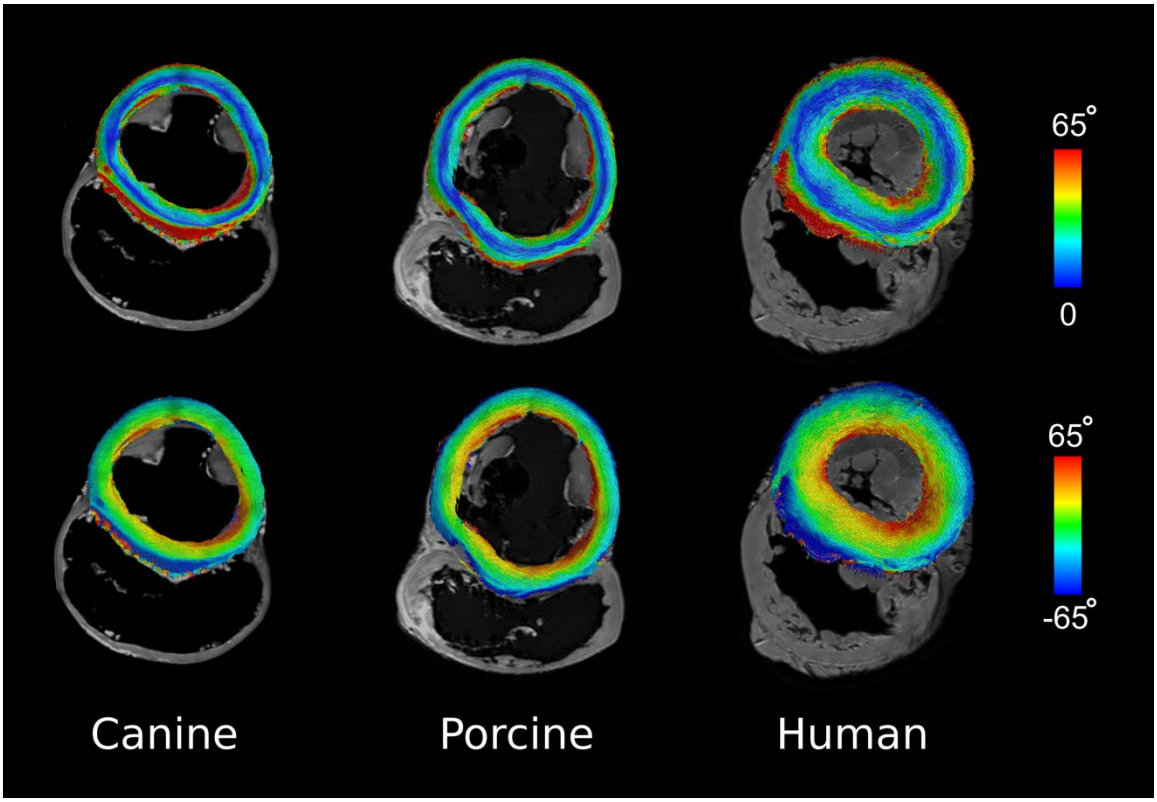

Figure 3.7: Primary eigenvector maps obtained in large animal (canine and porcine) and human hearts at a submillimeter resolution. The fibers in the left-ventricles are demonstrated with color-coding based on the inclination angle (bottom row), and the absolute value of inclination angles (upper row). The blue bands in the upper row images delineate the circumferentially running fibers of the midwall.

Finally, we imaged whole human hearts consisting of ventricles and atria using the developed DTI sequence. Figure 3.8 illustrates whole-heart tractography in a human heart. Detailed reconstruction of fiber architecture in the atria has been presented in Chapter 4.

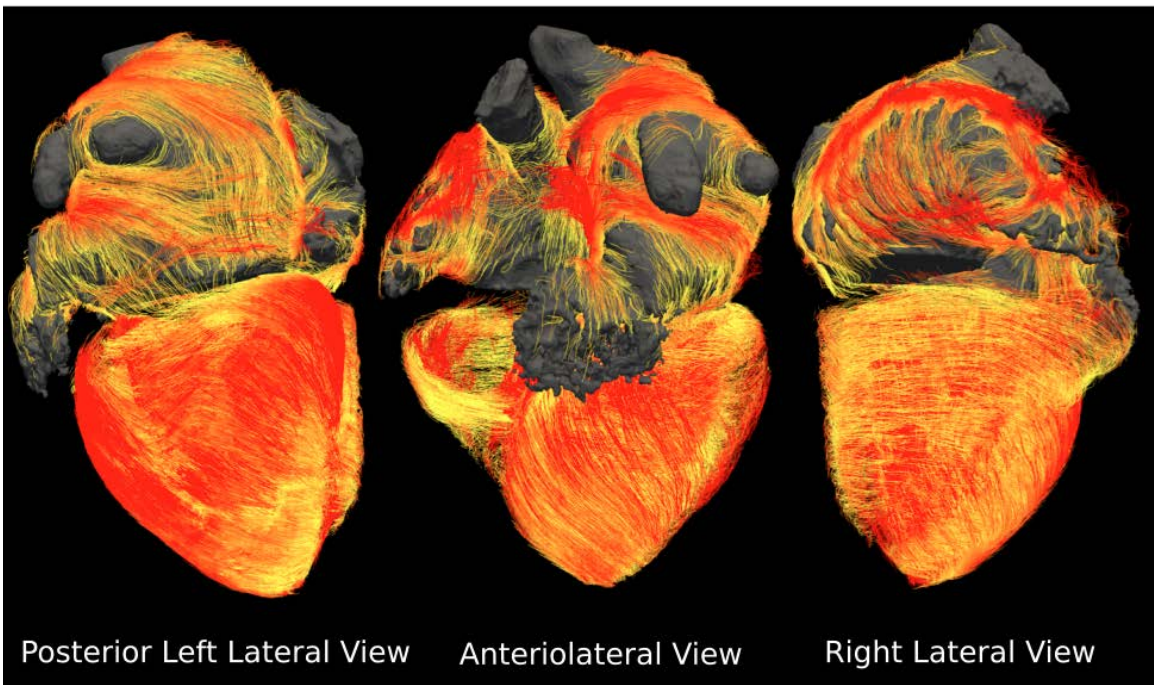

Figure 3.8: Whole-heart fiber tractography in a human heart obtained from the DTI technique in this thesis.

3.8 Conclusions

The 3D DTI technique presented here provides promising results to image the whole-heart specimens at a high image quality and resolution. In the next chapters of this thesis, we will utilize this methodology to investigate the microstructural characteristics of porcine and human hearts in normal and disease states.

Chapter 4

Myofiber Architecture of the Human Atria as Revealed by Sub-Millimeter Diffusion Tensor Imaging

This study has been published in *Circulation: Arrhythmia and Electrophysiology* [72].

4.1 Introduction

The exact relation between atrial structural pathways and electrical function/dysfunction in normal and diseased human atria has not been fully charactrized [51]. Atrial muscular architecture has a direct effect on atrial electrical activity by creating a preferential direction for excitation wave propagation [73] and has been shown to promote rhythm disturbances under a variety of conditions [16, 18, 74–77]. Therefore, accurate knowledge of the human atrial fibrous structure is important in understanding human atrial arrhythmia mechanisms; such knowledge could contribute significantly towards the improvement of strategies for treating atrial rhythm disorders [78].

Existing information regarding atrial fiber orientation has been acquired from photography and tracings of visually observed tracts after sectioning the atria [35, 79–81]. In addition to being destructive to the tissue and thus possibly introducing measurement biases, such methodologies involve the cumbersome task of reconstructing the 3D atrial structure from piece-wise data [82]; this task is particularly difficult for the large human atria. Furthermore, such acquisition methods render the systematic inter-subject comparison nearly impossible. Consequently, in contrast to the ventricles, there is a paucity of data regarding atrial fiber architecture variability in the human population. The need for such data is underscored by the fact that atrial anatomy varies greatly in the human population, as documented by *in-vivo* imaging [33, 34].

Diffusion Tensor Magnetic Resonance Imaging (DTMRI) is a non-invasive technique that uses water diffusion as a probe to image fiber orientation in tissue [83, 84]. DTMRI has been widely utilized to study fiber architecture in the brain

and other organs [85, 86]. Importantly, it has been successfully applied to acquire ventricular fiber orientations in normal and diseased hearts, both in animal species and in the human [87–91]. Ventricular fiber maps derived from DTMRI have been shown to correspond well to histological measurements of fiber angles [30, 64, 92, 93]. Acquiring DTMRI atrial fiber architecture, however, has proven extremely challenging. Difficulties arise from the fact that the atrial wall is significantly thinner than the ventricular wall, and from the high complexity of atrial fiber architecture, consisting of overlapping and interconnected bundles running throughout the chambers. Successful acquisition of atrial fiber architecture thus necessitates very high DTMRI image resolution and quality.

In this study, we present the first DTMRI acquisition of fiber architecture in the human atria. We have developed a customized 3D DTMRI sequence on a clinical scanner that makes it possible to image an entire intact human heart specimen *ex vivo* (Chapter 3). We have optimized the MRI sequence so that the scan can be performed over a long period of time without deterioration in image stability. The method yields both high image signal-to-noise ratio (SNR) and resolution, which are essential for capturing details in atrial structure. Here, we applied this new technique to reconstruct the 3D fiber orientation in eight human atria at a sub-millimeter resolution, providing an unprecedented level of information regarding both human atrial structure as well as its inter-subject variability. The information obtained in this study could lead to an enhanced understanding of atrial rhythm and pump disorders and thus improvements in their targeted treatment. The new DTMRI methodology is also expected to have broad utilization in acquiring the structure of other large specimens at sub-millimeter resolution.

4.2 Methods

4.2.1 Specimen Acquisition and Preparation

Human hearts (including the intact atria) were procured through the National Disease Research Interchange (NDRI, Philadelphia, PA). The hearts were from donors between the ages of 50 and 100 years (n=8, see Table 1 for donor characteristics). The tissue post mortem recovery interval was 12 hours. Diffusion imaging over a long time interval demands specimen preparation that ensures minimal artifact as well as sample stability during acquisition. In this study, the hearts were fixed in 10% buffered formaldehyde post recovery and were submerged in a buffer prior to imaging. In order to assure complete fixation of the whole heart, the specimens were scanned at least 40 days after the onset of the fixation in the formaldehyde. The atria were carefully filled and shaped, without damaging the tissue, to be close to the LV end-systolic state (maximum atrial filling) using compressed cotton absorbent. During acquisition, to obtain zero background signal from the heart chambers while avoiding specimen dehydration and susceptibility artifacts generated from the a tissue-air interface, the hearts were submerged in a perfluorocarbon solution (3M, Maplewood, Minnesota). Test scans were performed to detect and eliminate any air bubble artifact inside the atria. The images from the beginning and the end of the experiment were compared to confirm the negligible change in the level of the tissue signal and in the specimen position over the long duration of scan (see Section 3.6).

Heart	Age/Sex	Cardiac disease	Angle mean (°)	Angle spread (°)
Heart 1	93/F	MI	97	27
Heart 2	67/F	MI	98	26
Heart 3	90/F	Normal	168	36
Heart 4	76/M	MI	105	28
Heart 5	76/F	Normal	95	27
Heart 6	94/F	AF	100	19
Heart 7	86/M	AF	99	12
Heart 8	55/M	Normal	101	18

Table 4.1: Subject characteristics and measured fiber angles on the roof of the left atria for the post-mortem heart samples used in this study. The statistics were calculated based on the fiber angles measured within the patch shown in Figure 4.2. The "angle spread" is the root mean square deviation of the fiber angles (AF: Atrial Fibrillation, MI: Myocardial Infarction, M: Male, F: Female).

4.2.2 Imaging

The primary challenge for this project was to create a pulse sequence with sufficient resolution and diffusion sensitivity to image detail within the atrial wall, while retaining the imaging stability over the MRI scan time which averaged approximately 50 hours per specimen. The large specimen size of the *ex vivo* heart required a clinical scanner (3T Achieva TX, Philips Healthcare, Best, Netherlands). The RF coil used in this study was Philips 8-Channel head coil. The balance between high gradient amplitudes, and optimized imaging bandwidth for artifact reduction was found through a series of iterative trials. The final sequence used was a 3D Fast Spin Echo: TE = 60ms, TR = 625 ms, BW = 289.8Hz/pixel, number of echoes = 2, partial echo factor = 0.6, diffusion gradients duration = 22.9 ms, time gap between diffusion pulses = 12.5 ms, max gradient strength = 60 mT/m, number of diffusion encoding directions = 15, maximum b-value = 800

s/mm^2, FOV: 110x90x120 mm^3 (covering the whole heart), acquired voxel dimension: 0.5x0.5x1.0 mm^3. The images were reconstructed with 0.4mm^3 isotropic voxels by using zero padding. The measured SNR for the non-diffusion weighted images (b0) was ~120 (+/- 20). The 1.0 mm "slice" direction of the voxels was aligned with the longitudinal axis of the heart.

To achieve high accuracy in the segmentation of the thin atrial wall, specimens were additionally imaged using a 3D T1-weighted gradient echo MRI at an isotropic resolution of 0.25mm^3 (TE=2.3ms, TR=12ms, scan duration: 1hr). These higher resolution images were used to guide the segmentation process.

4.2.3 Post Processing

Raw MRI data were exported from the scanner and a customized image reconstruction was performed offline using MATLAB (The MathWorks Inc., Natick, MA) scripts. The reconstruction took advantage of the two spin-echoes to increase the SNR of the final diffusion images (Chapter 3). From the 15 diffusion encoded images and the b0 image, diffusion tensors were calculated using DTI Studio [65]. The atrial myocardium was segmented semi-automatically using manual thresholding and masking of the b0 image in combination with the T1 weighted image. Fractional Anisotropy (FA) is a scalar measure of diffusion anisotropy pattern in the tissue and ranges between 0 (fully isotropic diffusion) and 1 (fully anisotropic diffusion). Low and high cut-off thresholds were applied to the FA map (inclusion range: 0.01 - 0.45) to exclude the low-quality voxels (e.g. voxels with partial volume artifact, fat, tissue decomposition) that generate extreme FA values. These segmentation masks defined the boundaries for the measurement of fiber angles and other structural properties in the atrium.

4.2.4 Fiber Angle Measurement

A contribution of this work is the discovery of a reproducible coordinate system to express the relative fiber angles of the myocardial tracts on the roof of the LA. To do so, the origins of the 4 pulmonary veins were used as the reference points within the highly complex geometry of the atria. A "horizontal" vector was defined, connecting the median points of the left (inferior and superior) and right (inferior and superior) PVs, as shown in Figure 4.2. Once this coordinate system was established for each atrium, the principal eigenvectors were projected onto the local plane that is tangential to the atrial surface at the closest point. The fiber angles on the roof of the left atria were defined as the angle between the projected eigenvector and the projection of the horizontal vector onto the same tangential plane. In this coordinate system the fibers with an angle of 0° run left to right on the roof of the LA, and fibers extending in the anterior-posterior direction have fiber angle of 90°, as shown in the cartoon at the bottom right of Figure 4.2. For each heart, a ~2x2 cm patch was defined at the center of the atrial roof to measure the mean fiber angle on the roof (see schematic at bottom of Figure 4.2).

Maps of transmural fiber angle dispersions were created by calculating the angular deviations of local fiber angles inside a disk with diameter 4mm that goes through the entire atrial wall, regardless of wall thickness.

4.2.5 Tractography

For the purpose of visualization, fiber tracking was performed on the principal eigenvector using the Fiber Assignment by Continuous Tracking (FACT) algorithm [65] (stopping criteria: FA = 0.065, angle deviation = 45 degrees) in DTI Studio (see also Section 3.5). The resulting tracts are a macroscopic manifestation of fiber architecture and are locally aligned with the myofibers. The fibers were rendered using Trackvis software [94]. The original tracking algorithm (FACT)

that generated tracts from each voxel in the atria produced very dense fiber maps (~1M tracts in the whole atria). Showing all of the generated tracts would have made the visual tracing of the distinct bundles impossible, and obscured the endocardial layer of fibers. Thus, to achieve visualization appropriate for the goals of the study, we implemented a two-step process. In the first step, we performed a pre-selection on the original tractography results: We initially calculated the regional tracts' density by counting the number of tracts passing through each voxel. We then assigned a density score to each tract, which is the median of the densities of all the voxels that the tract passes through. Further, we grouped all the tracts into N=50 distinct bins, based on their density scores. Following that, a random sampling process was applied to each bin to select a pre-calculated number of tracts for the visualization. This number was inversely proportional to the bin density. This processing step resulted in a better visualization with fewer gaps in regions with lower density of tracts. In the second step, the resulting tracts were culled down by uniform sub-sampling of the list of the selected tracts from the previous step. This culling down process was performed progressively in TrackVis until we achieved a visualization that captures the major features of the atria. The individual points on the fibers tracts were then color-coded based on their absolute distance from the endocardial shell (red: epicardial, yellow: endocardial).

In order to group the fiber tracts into the new basis set of "bundles" that are common to all atria, semi-automatic clustering was performed based on the similarity in the orientation of the neighboring tracts. An initial k-means algorithm was applied to regroup the tracts into a number of clusters (n>50), each containing adjacent tracts with similar fiber orientations. These clusters were then manually selected in TrackVis, by placing seed points on the atria and finding the tracts that intersect them. Total of 15 "basis" bundles were selected using this technique, each with a distinct orientation and spatial extent.

4.3 Results

As described in the Methods, all images were acquired with voxel resolution of 0.5x0.5x1.0mm^3 and reconstructed to 0.4x0.4x0.4mm^3. The average thickness of the atrial wall across the eight human atria was 2.73mm (5-95% quartiles: 0.98-4.38mm), which corresponds to 4.34 voxels (5-95% quartiles: 1.56-6.96 voxels). The mean Fractional Anisotropy (FA, see Methods) and Mean Diffusivity (MD) in the sampled atria were 0.18 (25-75% quartiles: [0.12-0.22]) and 8.5×10^{-4} mm^2/s (25-75% quartiles: $[6.8\text{-}10.1]\times10^{-4}$ mm^2/s) respectively. The corresponding values for FA and MD measured in LVs of the same hearts were 0.20 (25-75% quartiles: [0.15-0.23]) and 7.3×10^{-4} mm^2/s (25-75% quartiles: $[6.3\text{-}8.1]\times10^{-4}$ mm^2/s). Figure 4.1A,B presents data from two samples, illustrating the complexity of human atrial geometry. Figure 4.1A shows a short axis slice (b0 image, non-diffusion weighted) with the superimposed segmentation of atrial tissues (left and right atria, and the inter-atrial bundle). In Figure 4.1B, atrial geometry is rendered by the grey volume of the lumen. All main features of atrial structure, including the pulmonary veins (PVs) and the trabeculated surfaces of left and right atrial appendages have been captured at this resolution.

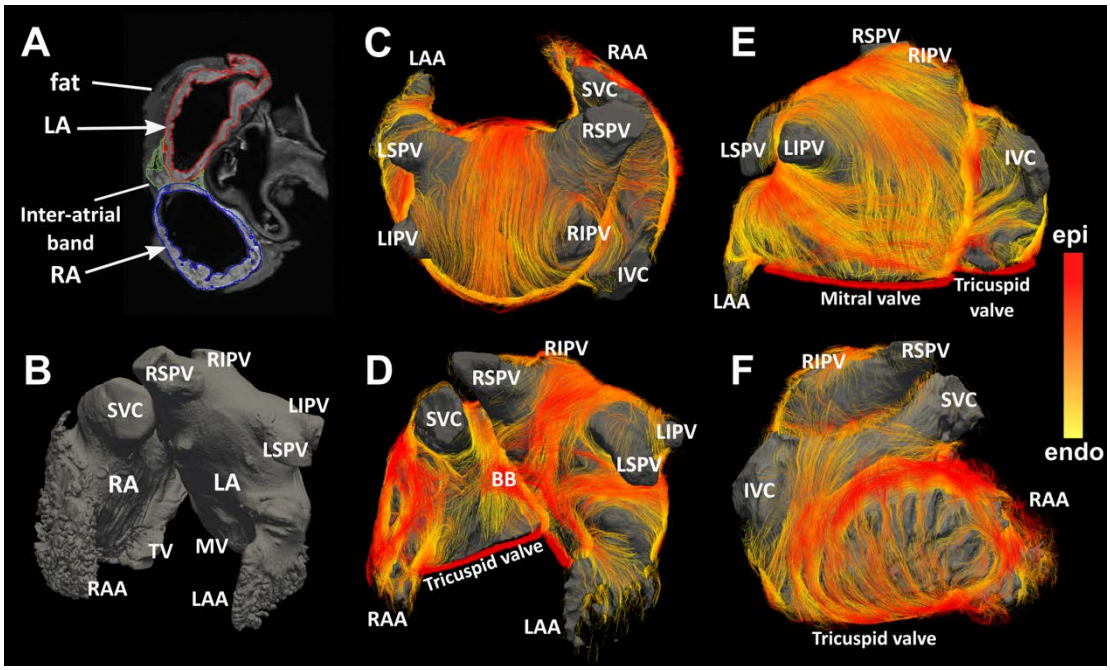

Figure 4.1: Acquired geometry and fiber visualization results in human atria specimens. (Left panel) Atrial geometry: (**A**) Short-axis view of a non-diffusion weighted image (b0) with superimposed segmentation of left atrium (LA, red), right atrium (RA, blue) and inter-atrial bundles (green). Fat tissue surrounding the atria is excluded from the segmentation. (**B**) Anterior view of left and right atria created from T1-weighted images; the dark grey volume represents lumen. (Right panel): Fiber visualization using tractography. (**C**) Posterior view of atrial roof. (**D**) Anterior view. (**E**) Inferior and left lateral view. (**F**) View of right atrium. Color encodes the local distance to the endocardial shell: yellow is the endocardial layer, and red is the epicardial layer. (LIPV: Left inferior pulmonary vein, LSPV: Left superior pulmonary vein, RIPV: Right inferior pulmonary vein, RSPV: Right superior pulmonary vein, LAA: Left atrial appendage, RAA: Right atrial appendage, IVC: inferior vena cava, SVC: superior vena cava, MV: Mitral valve, TV: Tricuspid valve, BB: Bachman bundle)

The 3D spatial organization of myofiber architecture was visualized using fiber tractography (see Methods). Figure 4.1C-F presents renderings of the fiber architecture in the same human atrial specimen from different anatomical viewpoints. The color at each point on the tract represents the shortest local distance to the endocardial shell and is used to illustrate the depth of the fiber tracts across the atrial wall (yellow on the endocardium, red on the epicardium).

Fiber tracts were found to have varying lengths and local densities (see Methods), and to be at different distances from the lumen. As the Figure 4.demonstrates, fibers traveling in different directions cross over or transition into each other throughout the atrial wall. The presented images illustrate the complexity of atrial fiber architecture in the three-dimensional (3D) organ.

Fiber tractography results were obtained for all 8 human atrial specimens, as described in Methods. Figure 4.2 presents tractography for the roof of each left atrium (LA, posterior aspect). To assess inter-subject variability in fiber orientation in this region of the atria, fiber angles were measured using a coordinate system constructed from the 4 origins of the pulmonary veins, as described in Methods (see schematic at bottom of Figure 4.2). Results (Table 1) reveal a dominant longitudinal orientation of fibers at the LA roof in 7 of the 8 specimens; the average fiber angle for the 7 specimens (excluding Heart 3) was 99 degrees, with a *very* small standard deviation of 3 degrees. Heart 3 is uniquely different from the other samples. It contains a mixture of longitudinal and oblique fibers at the LA roof (mean angle of 168 degrees).

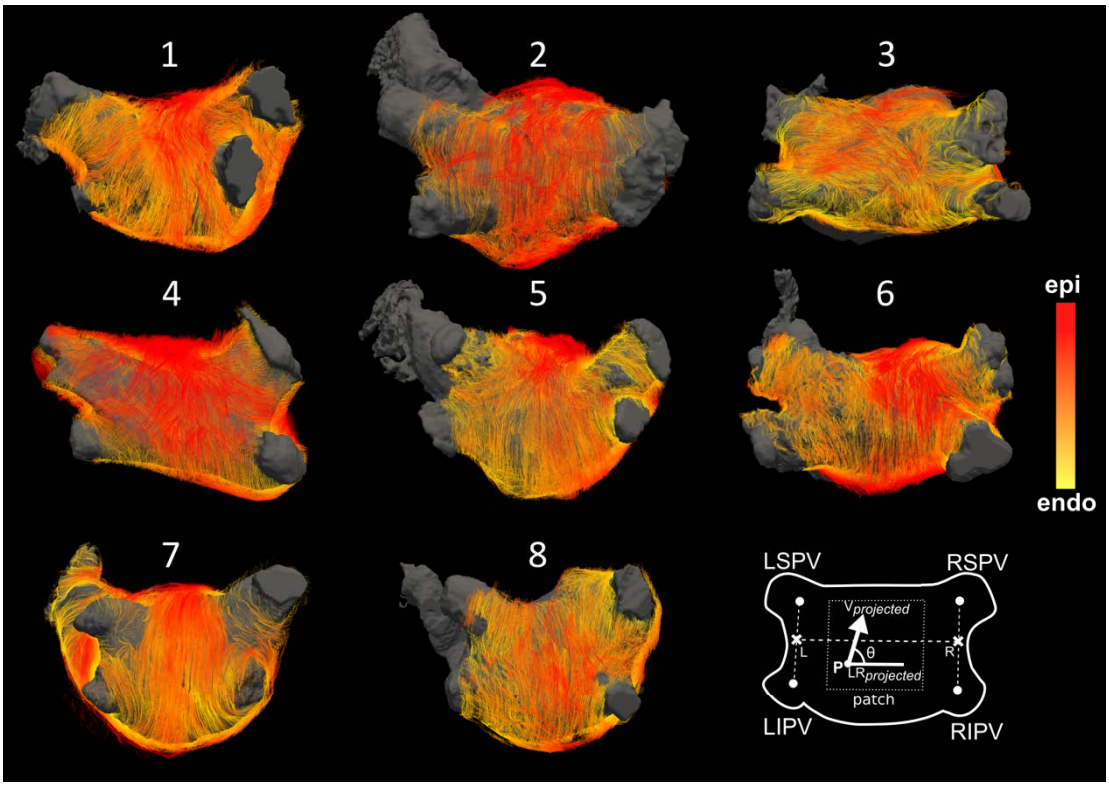

Figure 4.2: Fiber tractography in eight hearts as viewed posteriorly over the roof of the LA. The lumen of each atrium is colored gray. Color-coding is as in Figure 4.1C-F. The schematic at the bottom right shows the "horizontal" direction defined by the four origins of the PVs, as described in Methods. Fiber angles on the roof of the posterior wall are measured with respect to that horizontal (marked LR in schematic). Average fiber angles at the roof were calculated in the region outlined by the dashed box.

We next studied the fiber architecture across the depth of the atrial wall. Figure 4.3 demonstrates the fibers at different transmural layers of human atria as viewed from posterior and anterior sides, using sub-endocardial and sub-epicardial cuts. Further characterization of regional changes in fiber orientation across the atrial wall in 8 specimens is presented in Figure 4. Fiber tractography in posterior and anterior views of specimen 4 and 1 are shown in Figure 4.4A,C, respectively. In Figure 4.4A, top, two regions of interest (ROI), each of radius 4mm, are delineated; they are ~16mm apart. Histograms display the *transmural* distribution of fiber angles in each ROI (Figure 4.4A, middle row). The bimodal distribution of angles

in ROI A (located closer to the left inferior PV) demonstrates the presence of two layers of distinct local fiber orientations across the wall -- the fiber layers run in perpendicular directions. This change in fiber angles in direction from epi- to endocardium takes place abruptly at the midwall (Figure 4.4A, bottom). ROI B shows a unimodal distribution of fiber angles that is mainly oriented along the medial axis of the posterior wall. Similar findings are presented in Figure 4.4C,D.

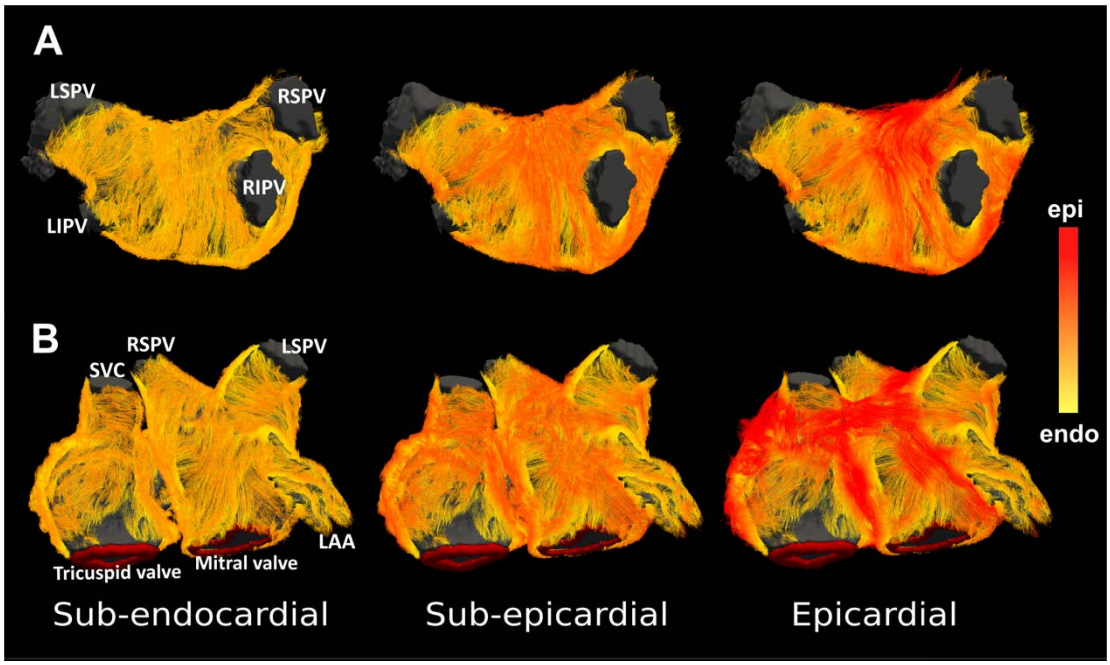

Figure 4.3: Fiber tractography of human atria (specimen 1) at different transmural layers as viewed from the Posterior (A) and Anterior (B) sides. The right column presents the original tracts. Left and middle columns represent the same results with sub-endocardial and sub-epicardial cuts, such that the outer layer fibers (at higher distances from the endocardium) have been removed from the visualization. The tracts have been visualized at a higher density (less culling down – see Supplementary Methods) in comparison to Figures 4.1 and 4.2. The color-encoding is based on the distance from the endocardial shell.

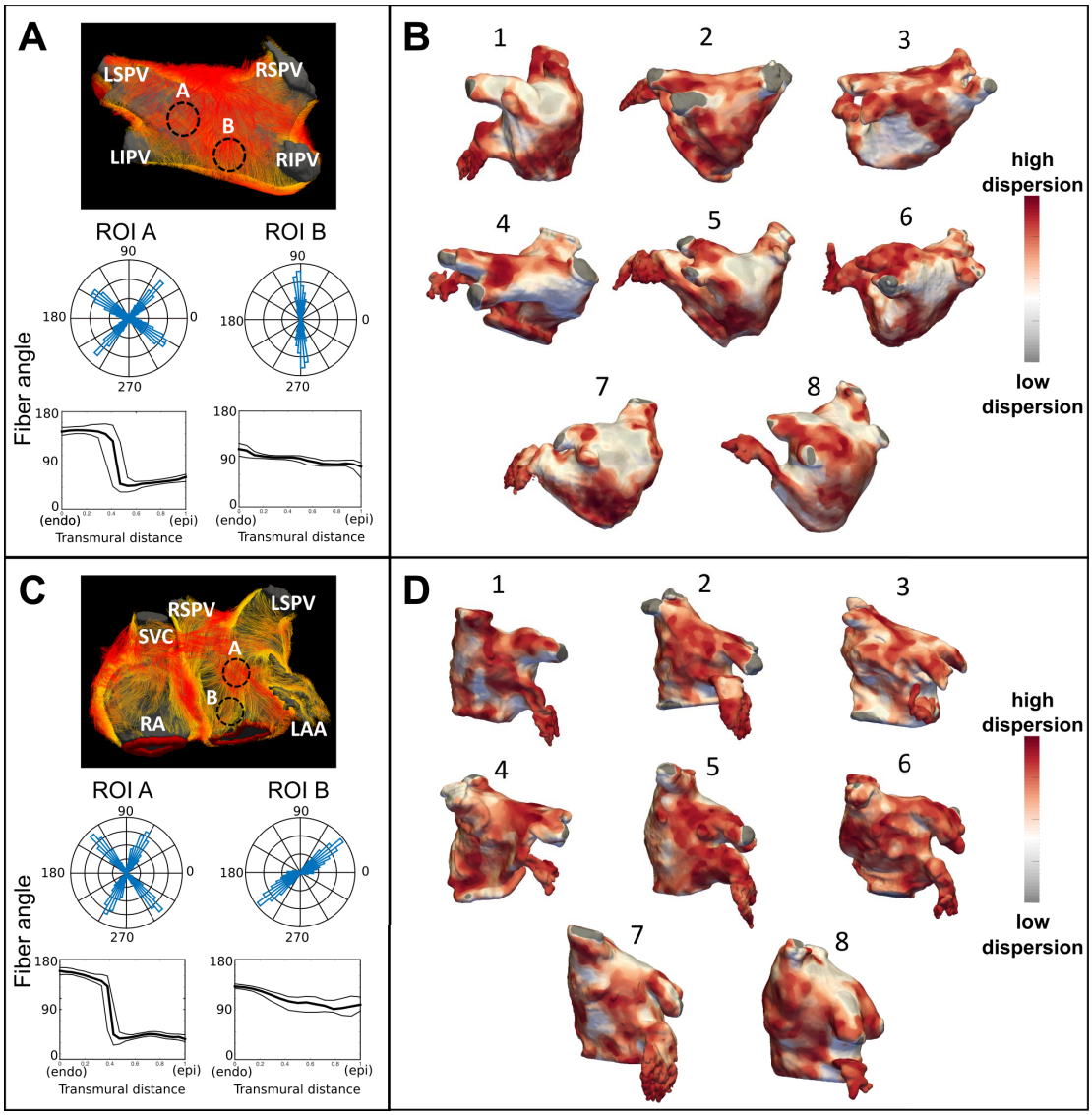

Figure 4.4: Regional changes in fiber orientation across the atrial wall. (A) (top) posterior view of the LA of specimen 4; (middle), a histogram of the transmural distribution of fiber angles from two ROIs; and (bottom), the transmural profile of fiber angles as a function of atrial wall depth in ROIs A and B. (B) Posterior lateral view of the maps of transmural angle dispersion for the eight specimens. (C) Same as (A) in sample 1. (D) Anterior view of the maps of transmural angle dispersion.

The pattern of fiber architecture with two distinct layers of different (nearly perpendicular) orientations across the wall was observed at several locations in the atria. To better assess fiber structure in the depth of the atrial wall, we quantified

the transmural fiber dispersion throughout the atrial wall in each specimen by the angular deviation of the local fiber angles (see Methods). The angular deviation was color-coded and mapped onto the corresponding atrial lumen surface (Figure 4.4B,D). There was a dominant unimodal transmural fiber pattern at the LA roof of 4 of the atria (specimens 1,5,6 and 7). The remaining specimens were characterized with fiber patterns of higher transmural dispersion in orientation, particularly near the PVs. In all samples, the inferior and anterior sides of the left atria exhibited a high dispersion in transmural fiber angles, while the lateral wall of the left atria below the left PVs had consistently a unimodal transmural fiber distribution.

As demonstrated above, tractography results revealed the presence of fiber tracts with varying spatial extent and orientation throughout the atria. Our analysis demonstrated that groups of neighboring tracts running in the same direction tend to form major bundles that in some cases constitute distinct anatomical features of atrial muscular architecture. We used a semi-automatic algorithm to cluster distinct bundles from the full tractography data (see Methods). The results for specimen 7 are presented in Figure 4.5, demonstrating 15 distinct major bundles (labeled a-l). *Importantly, presence of these major bundles was consistent across most of the specimens despite variation in cardiovascular clinical status of the subjects*. For instance, two of the patients in this study had recorded history of atrial fibrillation (Hearts 6 and 7); our measurements showed larger left atrial blood volumes for these two patients in comparison to the rest of the population. Despite this, we did not find any conspicuous differences in the fiber architecture of these two specimens when compared to the rest of the hearts; the general patterns of major fiber bundles (Figure 4.5) were observed in these two samples as well. The description of the major bundles follows below, *presented in the context of their place within the overall 3D atrial architecture*, and in relation to known atrial structures [35, 80].

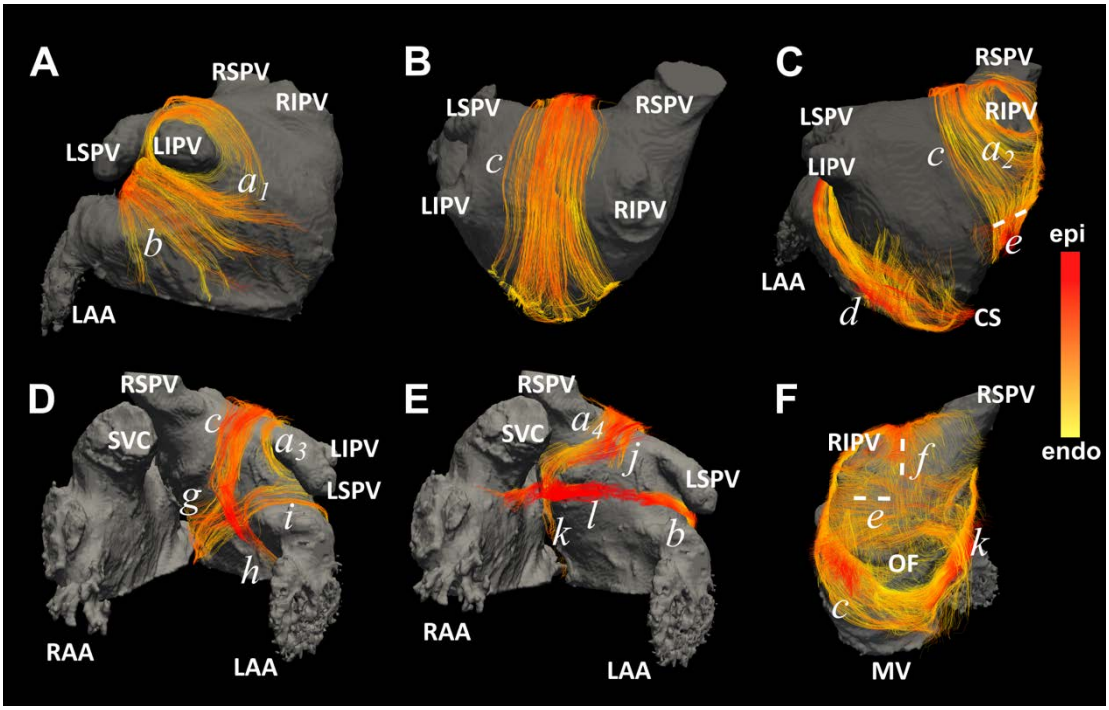

Figure 4.5: The major fiber bundles in the human LA. (**A-C**) Posterior; (**D**,**E**) Anterior view, and (**F**) Septum. The individual bundles are denoted a-l in heart 7.

The major fiber orientation on the posterior wall of the left atria was found to be posterior-to-anterior (Figure 4.1C and Figure 4.5B - bundle **c,** recognized in the literature as Septopulmonary bundle [95]). On the left and the right, this bundle transitions toward the bundles that encircle the base of each PV (bundles a_1 through a_4). A group of fibers on the inferior-posterior and lateral side of left atrial wall (bundles **b** and **d** in Figure 4.5A,C) run circumferentially around the "waist" of the LA, crossing, on the posterior wall, over the Septopulmonary bundle (see also Figure 4.1E).

A pattern of overlapping fiber bundles was observed consistently on the anterior side of all the human atrial specimens (Figure 4.1D, Figure 4.5D,E) [80]. One dominant fiber bundle on this side was the inter-atrial band, which originates below the superior vena cava (SVC) in the right atrium (RA) and bridges the LA

(known as Bachman Bundle [96], Figure 4.5E bundle **l**). The extension of the Bachman Bundle on the left side of the LA splits into two bands that run around the LAA (Figure 4.4D bundle **h** and Figure 4.5E bundle **b**). The inferior part of the anterior wall in proximity to the mitral valve consists of oblique and circumferential bundles (Figure 4.5D,E). These bundles represent extensions of fiber tracts from the LA roof and lateral wall (Figure 4.5D bundles **g** and **i**, respectively). The superior side of the anterior wall contains another oblique bundle that originates from the base of the left superior pulmonary vein (LSPV) and runs toward the septum below the right superior pulmonary vein (RSPV, Figure 4.5E, bundle **j**). The extension of this bundle continues through the inferior septum (bundle **k** in Figure 4.5E,F).

The septal wall incorporates circumferentially-running fibers that extend from the posterior wall (Figure 4.5F, bundle **e**), as well as obliquely-running fibers originating between the right PVs (Figure 4.5F, bundle **f**). Depicted in Figure 4.5F, the Oval Fossa (OF) is a known distinct structural feature of the septal wall [80]. Fibers run circumferentially inferior to OF and extend to the posterior and anterior walls via the extension of bundles **c** and **k,** respectively (Figure 4.5F). There is also a distinct group of fibers from the RA that run circumferentially around the OF center (Figure 4.5F).

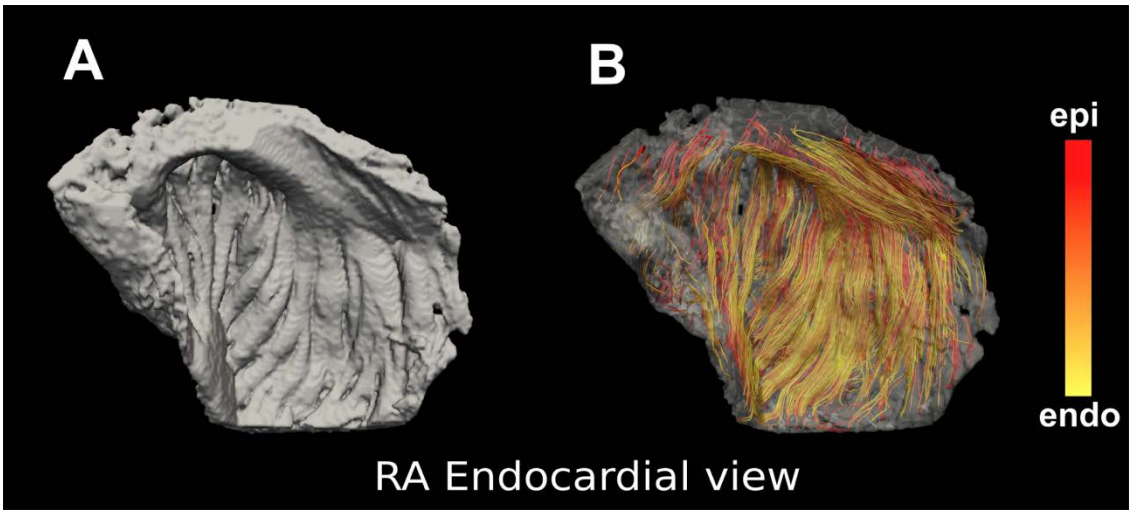

Figure 4.6: Endocardial view of the right atrium of specimen 4. (**A**) 3D rendering of trabeculated structure reconstructed from non-diffusion weighted MR images and (**B**) the corresponding fiber tracts overlaid on top. The pectinate muscles and crista terminalis of the right atrium are manifested as dense tracts in tractography results. The orientation of these fiber tracts follows the trabeculated structure of the endocardial wall (**A**).

The right atrial wall contains the specialized structures of the crista terminalis (CS) and pectinate muscles (PM) [80]. These structures manifest themselves in the tractography results as dense parallel bundles (Figure 4.1F and Figure 4.6B). As seen in Figure 4.1F, PMs run longitudinally throughout the wall and transition into CS bundles. The CS bundles are oriented in the inferior-to-superior vena cava direction and extend below SVC on the anterior side. The orientation of these fiber tracts generally follows the trabeculated structure of the endocardial wall (Figure 4.6).

4.4 Discussion

In this study we reconstructed the 3D myofiber organization in human atria non-destructively and at sub-millimeter resolution. To do so, we developed a high-resolution optimized 3D diffusion tensor MR technique on a clinical scanner (to accommodate the large specimens) and imaged the fiber architecture in eight

human hearts *ex vivo*. The novel sequence and sample preparation allowed us to acquire the data over long scanning times with high image stability and high SNR. Using the technique, we were able to trace and characterize major bundles individually, and importantly, to present the relation between the various structures in the context of the overall 3D atrial fiber architecture. The sub-millimeter resolution of the data provided information regarding local myofiber orientation across the atrial wall as well as the spatial heterogeneity of transmural fiber angle dispersion throughout the whole atria. The data presented in Figures 4.1 and 4.2 portray the first complete maps of atrial fibers in the entire atria. Furthermore, acquiring data on eight human atrial specimens allowed us to study the variability and similarity of the observed patterns across subjects.

The inter-subject analysis of the fiber architecture demonstrated that the main features of atrial anatomy are mostly preserved across subjects, although the exact location and the orientation of the bundles vary from heart to heart. *The dominant feature on the roof of the atria is the longitudinal fibers that transition to a circular pattern encircling the four pulmonary veins* (Figure 4.1C and Figure 4.2). These "vertical" bundles were clearly observed in 7 of the 8 hearts of the study. However, in one of the hearts a mixed pattern of oblique and horizontal fibers was present on the roof (Figure 4.2 – Heart 3). Nathan et al [79] studied variability of superficial fibers at the junctions of the PVs in 16 postmortem hearts using dissection and visual tracing in the 1960s. They also observed the presence of mixed and oblique pattern of fibers in their population and reported that the most frequent fiber pattern on the roof was longitudinal, which is consistent with our findings. The systematic measurement of myocardial architecture properties such as fiber angles requires the definition of a coordinate system (or systems) in the atria that is reproducible across subjects with various atrial morphologies. This has been suggested previously for the ventricles [97] but is particularly difficult for the atria

due to their complex shape. Our findings show that in 7 of the 8 specimens there exists a coordinate system in each LA that is based on the origins of the PVs, and in which major fiber bundles runs in the same orientation (within 3 degrees) on the roof and posterior wall. These findings suggest that this PV-based coordinate system (or a variation of it) could be an intrinsic choice for systematic measurements in the atrium.

The atrial wall has been previously suggested to have a bilayer structure, with fibers in the epicardial and endocardial layers running in nearly perpendicular directions. Evidence for this comes from either measurements undertaken at the tissue level [18] or qualitative descriptions at the organ level [35]. The data obtained from DTMRI here enabled us to "see through" the atrial wall (Figure 4.3) and perform quantitative measurement and characterization of the local transmural fiber distribution throughout the atria. Bilaminar muscular architecture was indeed documented by DTMRI in the posterior-inferior and anterior regions; however, in the lateral wall and the roof of the LA the fiber angles were essentially constant from endocardium to epicardium (Figure 4.4). This analysis demonstrated that the transmural fiber angle distribution in the atria is regionally heterogeneous.

The new knowledge obtained from this study can help interpret with greater accuracy experimental and clinical findings about the functioning of the atria and help better elucidate the link between electrophysiological and electromechanical activity, and the structural features in the normal and diseased atria. Of particular importance is the role of atrial structural organization and heterogeneous fiber orientation in rhythm disorders, as explored by a number of experimental and clinical studies [73, 75–77, 98–101]. For instance, characterization of left atrial activation in human subjects has revealed that the change in fiber orientation and wall thickness at the boundary of the Septopulmonary bundles in the posterior could lead to conduction block during sinus rhythm propagation [99]. The same

structural features have been shown to be substrate for atrial fibrillation initiation following rapid burst pacing at the PVs in normal sheep hearts [76]. In the right atrium, the branching sites of the CT and PM were found to cause frequency-dependent breakdown of wave propagation into fibrillatory conduction [77]. The results of our study could be employed to gain further insights into the structural contributions of atrial activity in health and disease. For instance, we can speculate that the spatial variation of transmural dispersion (Figure 4.4) could promote local conduction disturbances as the wave travels from a region with a more uniform transmural fiber orientation to a region with a bimodal distribution, particularly under conditions of decreased excitability. Such spatial heterogeneity in fiber orientation could also modulate the dynamics and localization of atrial rotors underlying human atrial fibrillation [102, 103].

Accurate human atrial fiber orientation data is essential for the construction of computational models of the whole human atria [82, 104, 105], and the need for it has been acknowledged in numerous studies [106–110]. The DTMRI results presented here provide unprecedented detail about fiber architecture that can easily by incorporated in atrial models by co-registration and morphing methodologies [91, 111]. The presented set of the major bundles (Figure 4.5) in combination with information about wall-thickness and transmural distribution of fiber orientation could form the basis for an accurate mathematical reconstruction of atrial fiber architecture (i.e. a rule-based approach, comprising of fiber orientation "rules" based on the present data) thus enabling atrial model construction from purely geometrical data (e.g. CT or MRI scans) of individual patient atria. The discovery of a common coordinate system and set of reproducible fiber bundles among specimens, as demonstrated here, could facilitate this approach. The integration of detailed structural data into computational models of whole human atria could further help identify the role of individual atrial

structures in human arrhythmogenesis under various conditions. Furthermore, patient-specific atrial models are being constructed with the goal of identifying the optimal ablation targets for atrial flutter and fibrillation in an individualized way [108]. Incorporation of accurate fiber orientation will ensure improved accuracy in these clinical translation-bound modeling efforts.

The present study could have important implications for the design of methodologies for the acquisition of atrial fiber architectures in patients. Despite the increasing number of attempts at *in vivo* DTMRI for assessing myofiber structure in the left ventricle, diffusion imaging of a beating heart remains extremely challenging, with many co-founding factors, such as bulk motion and myocardial strain, that can affect the measured signal [112–114]. The thin wall and the complex pattern of fibers in the atria present additional challenges to this task as compared to the ventricles. However, we can speculate that given a strong baseline knowledge of the fiber patterns in the human atrium, such as obtained in the present study, one could design a diffusion weighted sequence to detect those patterns in selected regions of the atria *in vivo*. This would require the rational design of imaging volumes and voxel orientations to include resolvable sections of the atria in each patient. The *ex vivo* data obtained in this study would inform the definition of those resolvable sections, and therefore, would facilitate a targeted imaging of the atrial fiber structure in patients.

Limitations: Despite the sub-millimeter resolution of our DTMRI imaging, with ~4.5 voxels across the atrial wall in most sections, those sections with thickness less than 0.5 mm could not be reliably imaged; these very thin areas were usually located in the extension of the veins and occasionally in portions of the right atrial wall. Furthermore, while we were able to characterize consistent fiber orientation patterns across the atrial specimens, the advanced age of the donors (55-94 years) and their history of cardiac disease may render our findings not entirely applicable

to the atria structure of the general population. Finally, the number of subjects studied here is small and thus the findings may not reflect the true population diversity. The limited number of donor hearts also limited our ability to study the link between structural properties and disease state; however, we believe this study sets the groundwork for such investigations in the future.

Chapter 5

Diffusion Tensor Imaging of Myocardial Infarction

5.1 Introduction

Myocardial Infarction (MI) is a major cause of death, affecting millions of people worldwide [115]. The occurrence of MI initiates a complex process of cardiac remodeling that leads to changes in tissue composition, geometry and the function of the heart [116]. While it is clear that MI can lead to heart failure and arrhythmia, the exact linkage between post-MI structural remodeling and the electromechanical functioning of the heart is not completely understood. Accurate knowledge of infarct structure and fiber orientation remodeling in the intact heart is essential for understanding MI pathophysiology. The need for such data is underscored by the fact that infarct structural remodeling is complex and three-dimensional in nature, which is reflected mechanistically in the associated changes in cardiac function. However, there is little data published regarding the detailed three-dimensional scar geometry and the corresponding fiber orientation remodeling in intact large animal and human hearts.

Early renditions of myocardial fiber structure were based on sectioning approaches [29]. These methods produce excellent high-resolution data of local tissue structure [38]; however, combining these measurements together into a registered whole organ data set is extremely difficult. Diffusion Tensor Imaging (DTI) is a non-destructive tool that utilizes the restricted diffusivity of water molecules to assess the tissue microstructure [84]. DTI yields data on the mean diffusivity of water molecules, quantified by Mean Diffusivity (MD), as well as the directional variability of the water diffusion measured by Fractional Anisotropic (FA). Importantly, calculation of the principal diffusion eigenvector allows tracking of the underlying fiber orientation in the tissue. DTI has been utilized in infarcted animal and human hearts to characterize the microstructure using diffusivity measures such as FA and MD [117–119], and to assess the remodeling in fiber arrangement remote from and at the infarct [120–125]. However, reliable imaging of

the fiber orientation at and near the infarct has proven challenging [121]. This is mainly due to the fact that the infarcted region is often associated with significant wall thinning and hence a higher image spatial resolution is required to reliably track the fiber angles across the wall. In addition, the low diffusion anisotropy in the infarct increases the measurement uncertainties in determining the principal eigenvectors of the diffusion tensors, particularly in a low image signal-to-noise (SNR) regime [62]. Accurate reconstruction of fiber orientation in infarcted hearts thus necessitates DTI sequences that produce high image spatial resolution and high SNR. Our group has recently developed such methodology that has proven successful in imaging myofiber orientation in the thin atrial walls [72].

In this study, we employed the previously developed [72] 3D DTI sequence on a clinical scanner (Chapter 3) and applied it to image *ex vivo* intact chronically-infarcted porcine and human ventricles at a sub-millimeter resolution. We used this technique in conjunction with high-resolution T1-W Gadolinium-Enhanced MRI, as the gold standard for imaging myocardial fibrosis, to reconstruct the ventricular fiber organization and scar geometry in eight porcine hearts at image resolution and signal-to-noise ratio (SNR) higher than previously achieved. The detailed knowledge of infarct structure and fiber orientation obtained in this study is expected to enhance our understanding of post-infarction remodeling and the associated rhythm and pump disorders, and thus lead to improvements in the their targeted therapies.

5.2 Methods

5.2.1 Specimen Acquisition and Preparation

Anteroapical infarction was created under an IACUC-approved protocol, by occluding the mid–left anterior descending (LAD) coronary artery in Yorkshire porcine for 120 min using a balloon angioplasty catheter (n = 8). The hearts were

excised at least 3.5 months after the induction of the MI (average MI age: 6.7 ± 2.9 months). As a gold standard for MI imaging, Gd-DTPA (Magnevist®) was injected (0.2 mmol/kg) 20 minutes before animal sacrifice. After the excision, the ventricles were filled with rubber (Task5™) to keep the heart in the natural unloaded shape. To avoid sample dehydration and susceptibility artifacts generated from the tissue-air interface, the hearts were submerged in perfluorocarbon, (Fluorinert-77, 3M) prior to subsequent imaging. To serve as controls, 4 normal porcine hearts were harvested from animals with no prior MI and prepared in a similar fashion. In addition to the porcine hearts, one intact human heart was procured through the National Disease Research Interchange (NDRI, Philadelphia, PA). This heart was from a donor with a history of MI (93 years old female).

5.2.2 Image Acquisition; Late Gadolinium Enhancement (LGE) MRI

For the infarcted porcine hearts, a Late Gadolinium Enhancement (LGE) MRI was performed using a T1-Weighted Gradient Echo sequence immediately after the excision, to image the enhanced infarcted region. The imaging was performed with the following scan parameters: acquired resolution 0.25x0.25x0.50 mm^3, echo time (TE)=2.3 ms, repetition time (TR)=12 ms, scan duration: 1hr. Subsequently, the specimens fixed in 10% buffered formaldehyde (>40 days) for the diffusion imaging session. The normal porcine hearts had no prior MI and the single human heart were not administered contrast agent subsequent to excision. Therefore, they did not undergo LGE imaging but were fixed in the same way as the infarcted porcine hearts. Time from harvest to fixation of the human heart was ~12 hours.

5.2.3 Image Acquisition; Diffusion Tensor Imaging (DTI)

The 3D Fast Spin Echo DTI sequence previously developed [72] was used on 3T clinical system (Achieva TX, Philips Healthcare, Best, The Netherlands) to image

the whole hearts *ex vivo* (n=4 control porcines, n=8 infarcted porcine and n=1 human heart). Typical imaging parameters were: TE = 63 ms, TR=504 ms, bandwidth = 290.0 Hz per pixel, number of echoes: 2, diffusion gradients duration: 22.8 ms, time gap between diffusion pulses=12.6 ms, maximum gradient strength = 60 mT/m, RF coil: Philips 8-Channel head coil, number of diffusion encoding directions: 15, maximum b-value = 800 s/mm^2, typical field of view: 110x115x130 mm^3, acquired voxel dimension: 0.6x0.6x1.2 mm^3, reconstructed voxel dimension (using zero-padding): 0.4-mm^3 and total scan duration ~ 42 hours. The human heart was imaged using the same imaging sequence but at the resolution of 0.5x0.5x1.0 mm^3.

5.2.4 Image analysis; Tensor Calculation and Tissue Segmentation

Raw MRI data were exported from the scanner and a customized image reconstruction was performed offline, using MATLAB (The MathWorks Inc., Natick, MA). Diffusion tensors were calculated using DTI Studio [65] and subsequently, the diffusion eigenvectors and eigenvalues were calculated in the normal porcine hearts and the human heart (Figure 5.1A,B). For the infarcted porcine hearts, the DTI tensor volumes were first co-registered to T1-W LGE data (Figure 5.1C) using 3D affine transformations. This spatial registration enabled us to reconstruct the fiber structure as well as scar geometry, when applicable, in the same coordinate system in each heart (Figure 5.1E), and to also correct for the slight shrinkage of the heart tissue due to the fixation process. Further, the endocardial and epicardial surfaces of the left ventricle (LV) were contoured to delineate the LV in each heart. In this process, the papillary muscles and trabecular structure on the left and right ventricles endocardial surfaces were excluded from LV segmentation (Figure 5.1A,E).

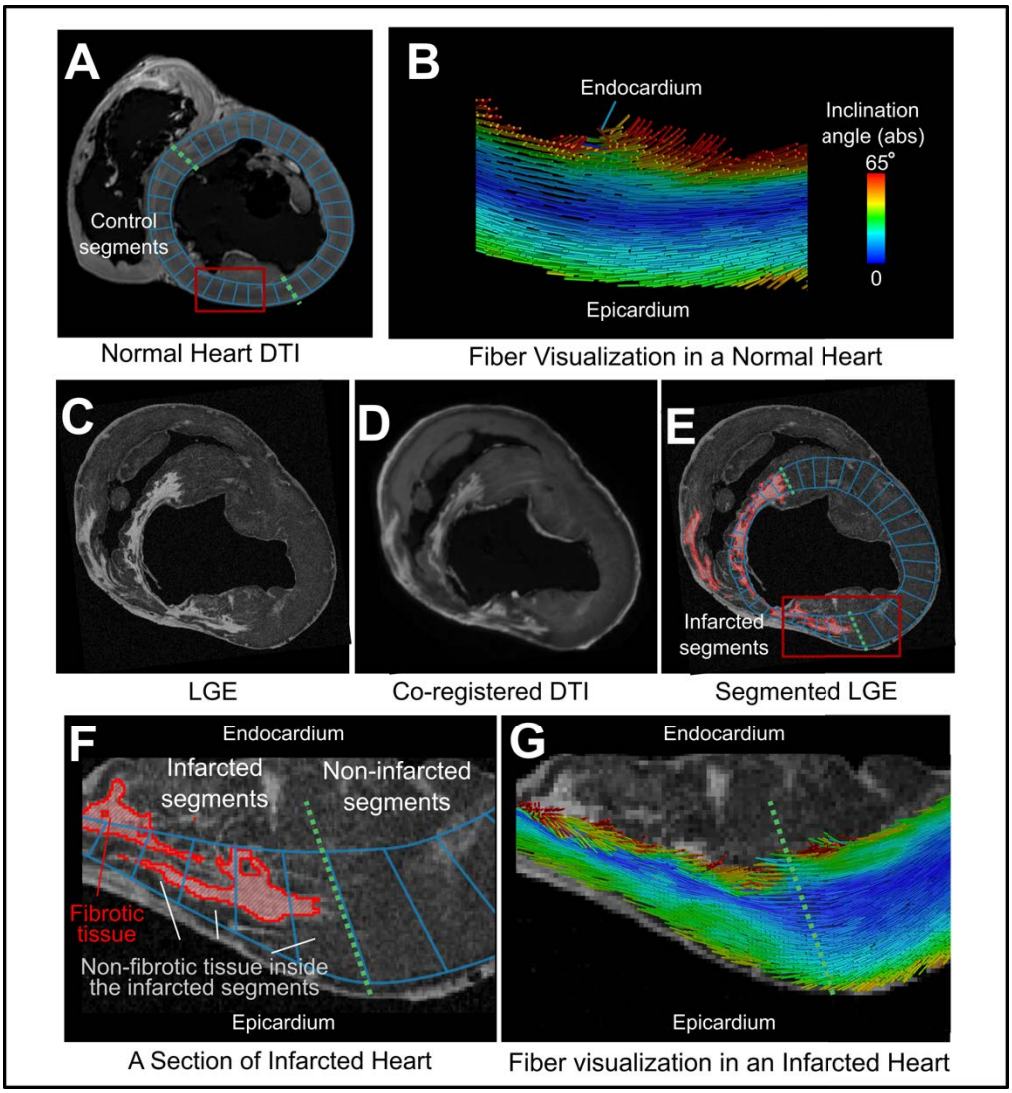

Figure 5.1: Pipeline for the analysis of structural remodeling at the infarct and border zone **(A)** A short-axis slice of a normal heart with the LV segments overlaid in blue. The area between the two dashed green lines delineates the control segments. **(B)** Eigenvector visualization of a section from anterior wall of the same normal heart (red box in A). The fibers are color-coded based on their absolute inclinations angles, i.e. the blue represents the circumferential fibers. **(C)** Short-axis slice of LGE-MR image in an infarcted heart **(D)** Co-registered non-diffusion weighted image. **(E)** The same slice as (D) and (C) but with LV segments and fibrosis mask overlaid in blue and red respectively. **(F)** Zoomed-in view of the red box in (E) illustrating the fibrotic and non-fibrotic tissues inside the infarcted segments. The green dashed line represents the boundary of infarcted and non-infarcted segments. **(G)** The fiber visualization in the same region as (F) showing the transition from the non-infarcted to infarcted tissue with the same color-coding as (B).

Next, an Otsu thresholding (n = 2) followed by a level-set segmentation was applied on the LGE images to classify ventricular tissue into two regions, fibrotic (enhanced) and non-fibrotic (Figure 5.1)

5.2.5 Fiber Angle Measurement

In all the hearts, the primary diffusion eigenvector angles were measured in a local coordinate system that is tangential to the LV endocardial surface (Figure 3.3). Detailed description of fiber angle measurement is provided in Section 3.4. In summary, the imbrication and the inclination angles were calculated for each voxels in the hearts. Note that although the term 'fiber' is used interchangeably here with the primary diffusion eigenvectors, it carries different physical meanings inside and outside the scar; 'fiber' in the non-fibrotic tissue refers to the myofiber structure, but in the fibrotic tissue it is reflective of the underlying scar structure, such as collagen bundles.

5.2.6 Analysis of Regional Remodeling; Definition of LV Segments in Porcine Hearts

To characterize the regional structure of the wall and systematically study the infarct remodeling in 3D, the LVs in the normal and infarcted porcine hearts were partitioned into small transmural segments as shown in Figure 5.1A,E. To do so, for each short-axis slice of 1.2 mm thickness (excluding the apical slices), a polar coordinate system was defined with an origin located at the center of the blood mass. In this coordinate system, the LV myocardium was divided circumferentially into 36 segments of 10° angular width per segment. This resulted into about N~1000 segments per heart.

Infarcted segments were defined as the LV segments that contained fibrotic tissue (Figure 5.1E,F). These segments were located at the anteroseptal wall, consistent with the LAD infarction protocol. The corresponding segments from the

same anatomical locations in the normal hearts were selected as control segments (spanning 180 degrees of the LV anteroseptal wall as delineated by the green dashed lines in Figure 5.1B). Moreover, due to the presence of viable tissue surrounding the scar and the complex scar geometry, the transmural infarcted segments could contain fibrotic as well as non-fibrotic tissues. These regions are highlighted in Figure 5.1F.

5.2.7 Analysis of Regional Remodeling; Quantification of Local Segment Structure in Porcine Hearts

Subsequent to defining the LV transmural segments, the voxel data from individual infarcted and control segments were analyzed with respect to the local fiber angles, wall thickness, and the extent of the fibrosis obtained from LGE images. The following metrics were defined for each segment: *wall thickness*, the wall thickness of the segment; *scar transmurality*, the ratio of the fibrosis volume to the total volume of the segment; *slope and intercept*, the slope and the intercept of a linear model fitted to the inclination angle transmural profile data (angle vs. the depth of the wall as measured from the epicardium); r^2, the coefficient of determination for the regression model of the inclination angle profile; *(epi-to-endo) inclination angle range*, the range of inclination angle within each segment as calculated from the [1-99]% of the inclination angle distribution; *imbrication angle mean*, the average of the imbrication angles within a segment; *left-handed ratio (LH ratio),* the ratio of the number of voxels in which the inclination angle $< -15^{\circ}$ to the total number of voxels within a segment; *circumferential ratio*, same ratio but calculated for the voxels with $-15^{\circ} <$ inclination angle $< 15^{\circ}$; and *right-handed ratio (RH ratio)*, same ratio but for voxels with inclination angle $> 15^{\circ}$.

In addition, to quantify local incoherency in fiber arrangement as an independent measure, individual normal and infarcted LV segments were divided into 10 sub-segments equally spaced through the depth of the wall. Each sub-

segments contained a small pool of voxels. The standard deviation of the inclination and imbrication angles in each sub-segment was calculated and then the results were averaged over the 10 sub-segments to arrive at an incoherency metric for each LV segment. This calculation was performed for inclination and imbrication angles separately and yielded two measures of fiber incoherency for each segment that together quantified the extent of local incoherency of the diffusion vector field. In comparison to direct calculation of local fiber angle gradient with a fixed kernel [117], the calculation of incoherency metrics in sub-segments with radial dimensions normalized to wall thickness, as presented here, is less sensitive to uniform changes in the radial gradient of fiber angles resulting purely from changes in local wall thickness.

5.2.8 Statistical analysis

Unpaired Student t-test statistics was performed on the quantities obtained from the infarcted and control segments throughout the porcine hearts to study the microstructural differences between these regions ($n_{control} = 2432$, $n_{infarcted} = 3344$). Further, Pearson correlations were calculated to study the pair-wise associations of slope, inclination angle range, wall thickness and scar transmurality in the infarcted segments from porcine hearts. All the data is presented as mean ± standard deviation.

5.3 Results

5.3.1 LV Characteristics in Porcine Hearts

The infarcted porcine hearts demonstrated significant global remodeling with changes in LV mass and LV blood volume (LV mass: 121 ± 47 gr MI vs. 70 ± 9 gr normal hearts, LV blood volume: 81 ± 26 cm^3 MI vs. 41 ± 25cm^3 normal hearts). The normal hearts had an average wall thickness of 7.86 ± 2.4 mm. By

comparison, the average wall thickness in the infarcted porcine hearts was 5.06 ± 2.99 mm for the infarcted segments and 9.57 ± 2.57 mm outside the infarcted segments. The scar volume comprised 10.1 ± 7.6 % of the LV myocardial volume in the eight infarcted porcine hearts.

5.3.2 Measures of Diffusivity in Porcine Hearts

To investigate the microstructural remodeling and particularly the extent of anisotropy in infarcted tissue, diffusion scalars were measured in the fibrotic tissue and the values were compared to non-fibrotic tissue from the infarcted hearts and tissue from the control hearts. Figure 5.2 presents the pooled distributions of FA and MD in all porcine hearts. Accordingly, Table 5.1 summarizes the diffusivity measures of FA, MD and the diffusion eigenvalues in the fibrotic, non-fibrotic and normal regions. Fibrotic tissue exhibited a lower mean FA value (0.228 ± 0.092) compared to non-fibrotic (0.309 ± 0.094, $p<0.001$) and normal tissue (0.379 ± 0.091, $p<0.001$). The MD value was higher in the fibrotic regions (9.3 ± 2.4 $\times 10^{-4}\,mm^2/s$) as compared to non-fibrotic (6.7 ± 1.5 $\times 10^{-4}\,mm^2/s$, $p<0.001$) and normal tissue (6.3 ± 1.6 $\times 10^{-4}\,mm^2/s$, $p<0.001$). In addition, as presented in Table 5.1, fibrotic tissue showed a greater dispersion of diffusion eigenvalues than non-fibrotic and normal tissues. Despite the lower diffusion anisotropy observed in the infarct, the FA inside the majority of the infarct was greater than that of an isotropic liquid (0.029 ± 0.008, $p<0.001$).

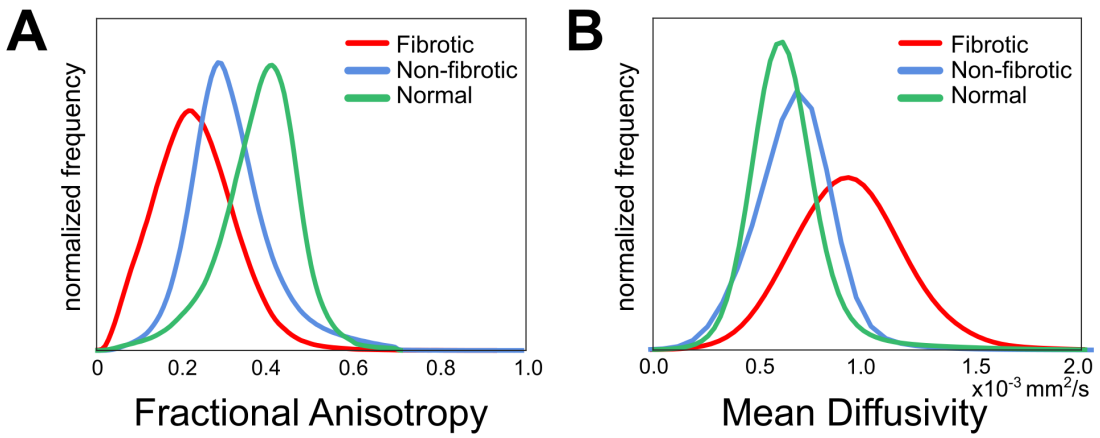

Figure 5.2: Pooled distributions of **(A)** Fractional Anisotropy (FA) and **(B)** Mean Diffusivity (MD) in the fibrotic (red) and non-fibrotic (blue) voxels from the infarcted hearts, and normal voxels from the control hearts (green). The fibrotic tissue was segmented from the LGE images as demonstrated in Figure 5.1F.

	Mean ± STD		
Quantity	Fibrotic	Non-fibrotic	Normal
e1 ($\times 10^{-4}$ mm^2/s)	11.28 ± 2.34	8.97 ± 1.62	8.90 ± 1.77
e2 ($\times 10^{-4}$ mm^2/s)	9.30 ± 2.56	6.27 ± 1.61	5.66 ± 1.75
e3 ($\times 10^{-4}$ mm^2/s)	7.36 ± 2.59	4.97 ± 1.50	4.24 ± 1.58
MD ($\times 10^{-4}$ mm^2/s)	9.31 ± 2.41	6.74 ± 1.49	6.27 ± 1.61
FA	0.228 ± 0.092	0.308 ± 0.094	0.379 ± 0.091

Table 5.1: Diffusion scalars measured in fibrotic and non-fibrotic tissue in MI hearts and normal tissue from control hearts. P<0.001 for all the pairwise Student T-tests. e1,e2,e3 : primary, secondary and tertiary diffusion eigenvalues respectively. MD: Mean diffusivity, FA: Fractional Anisotropy.

5.3.3 Diffusion Eigenvector Orientation in Porcine Hearts

The 3D organization of diffusion eigenvectors in the LV of an infarcted porcine heart is presented in Figure 5.3 with anterior (A,B), septal (C,D) and apical (E,F) views. The infarct geometry (grey volume) is obtained from LGE images and is overlaid over the diffusion vector field.

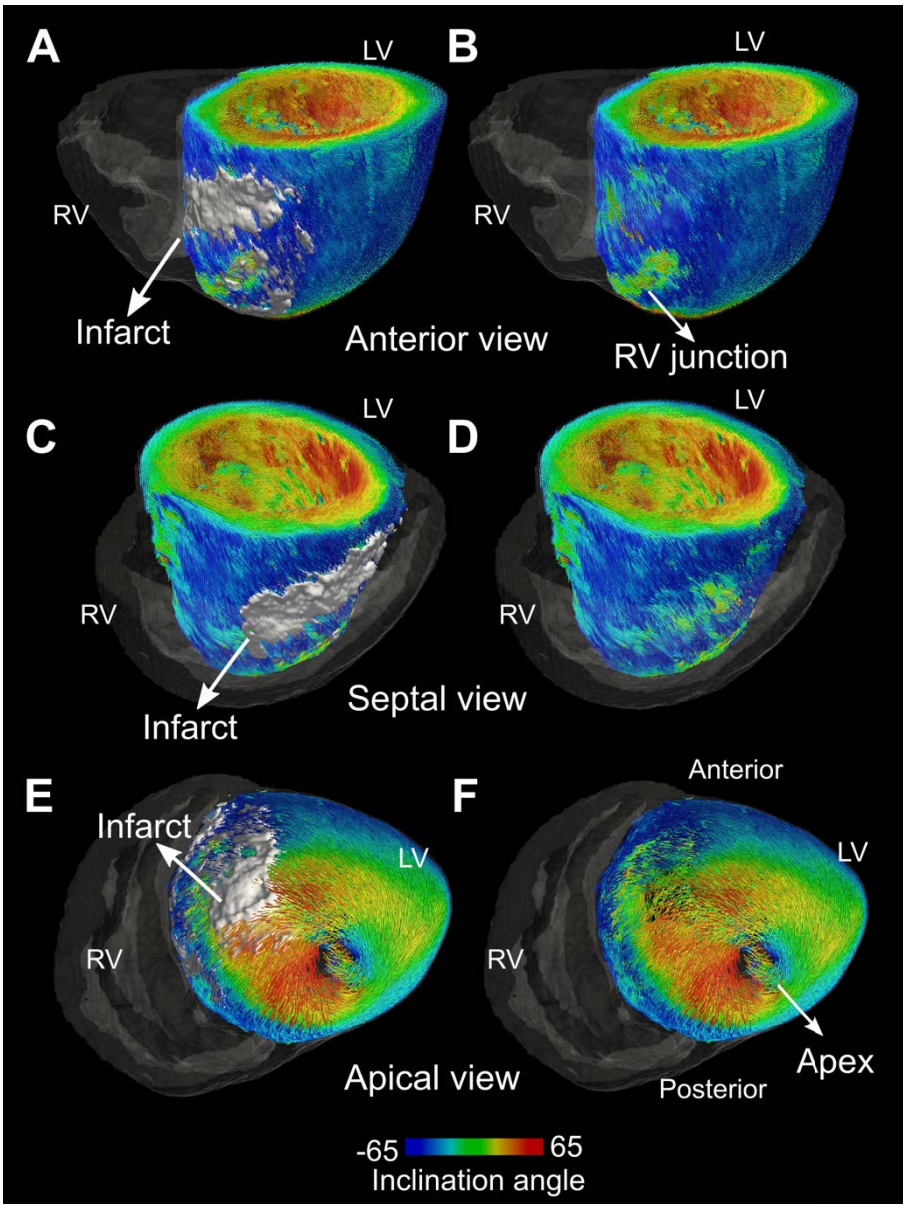

Figure 5.3: 3D visualization of primary eigenvectors in the LV of an infarcted porcine heart. (A-B) Anterior view, (C-D) Septal view and (E-F) Apical view. The fibers are color-coded based on the inclination angle. The transparent gray volume represents the right ventricle. The infarct volume is reconstructed from LGE-MRI and is rendered in gray in (A,C,E). The right panels (B,D,F) show the same views but without the infarct volumes, to visualize the underlying eigenvectors in the infarct.

As the figure demonstrates, the epicardial fibers at the infarct and in its surroundings are on average characterized with the original left-handed orientation (i.e. negative inclination angle). This was a consistent finding among all eight infarcted porcine hearts.

In Figure 5.4, the primary eigenvectors are visualized in a short-axis slice. The infarct is identifiable by the enhanced area in the LGE image (Figure 5.4A). Figure 5.4B shows the eigenvectors visualization in the same slice with color-coding based on the inclination angle. Three representative regions of interest have been selected in Figure 5.4A and their corresponding eigenvectors are presented in Figure 5.4C: (I) an infarcted wall, (II) a transition region between the infarcted and non-infarcted portions of the wall, and (III) a region remote from the infarct. The thinned infarcted wall (I) demonstrates the presences of epicardial, circumferential (blue band) and endocardial fibers that are arranged at a higher transmural gradient of inclination angle across the depth of the wall when compared to the section remote from the infarct (III). The middle panel in Figure 5.4C (II) presents the anterior region between infarct and non-infarct, highlighting the transition of eigenvectors from a non-infarcted region with a lower transmural angle gradient to the infarcted region with a higher angle gradient. The deflection of the circumferential blue band toward the endocardium in the middle of this region suggests that there is an immediate increase in the proportion of the left-handed fibers in the wall (LH-ratio), in transition from non-infarcted segments to infarcted segments. However, this observation was not consistent across all the transition zones in the porcine hearts as we also observed transition regions that had no deflection of the blue band toward the endocardium. An example of such transition zone is presented in Figure 5.1G.

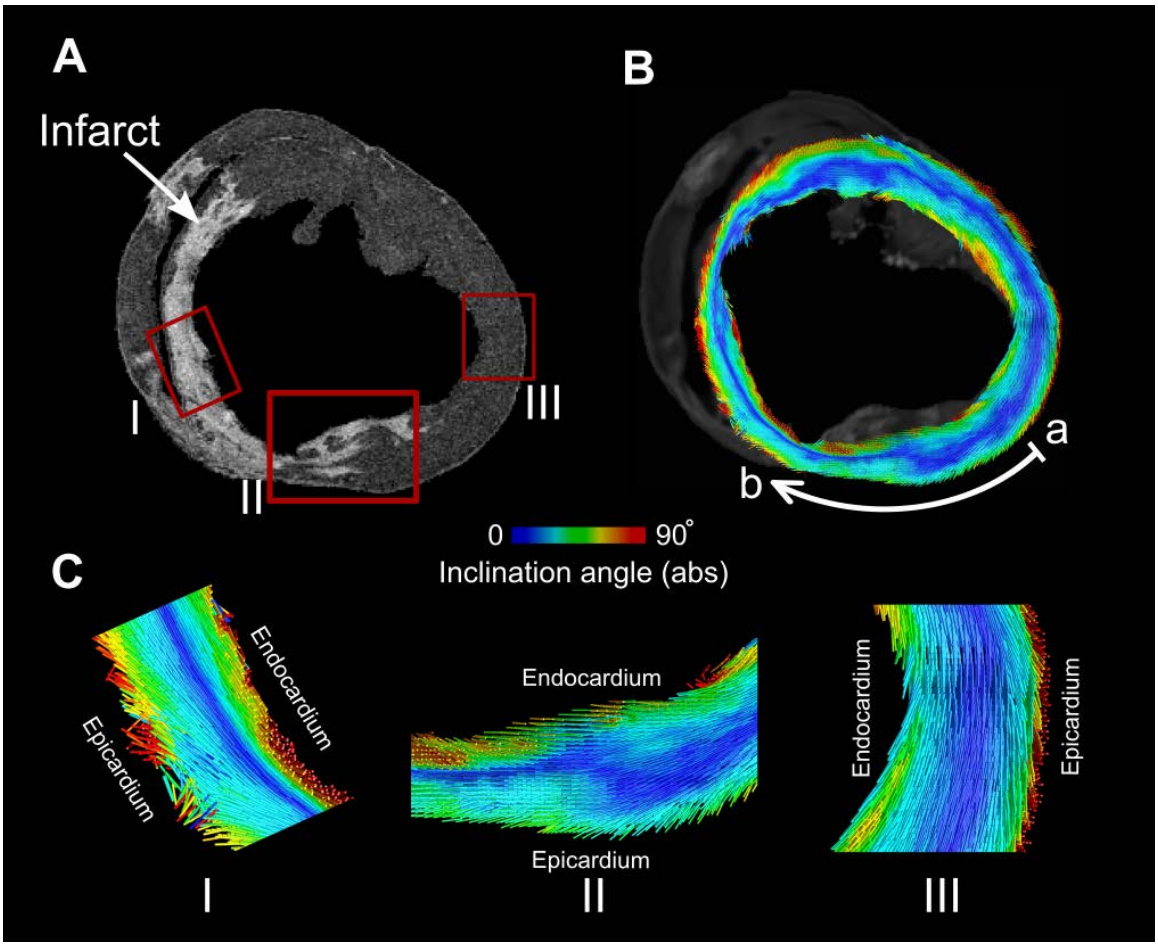

Figure 5.4: Visualiation of primary eigenvectors in a short-axis slice of an infarcted porcine heart. **(A)** A slice of LGE-MRI. The infarcted region is delineated by the enhanced image intensity. **(B)** (similar view as A) LV map of primary eigenvectors color-coded by the absolute value of the inclination angle **(C)** Eigenvector visualization in three regions of interest corresponding to the red boxes in A. I: Infarcted wall in septum, II: transition zone between infarcted and non-infarcted portions of the wall in anterior wall, and III: non-infarcted region in lateral wall. The original inclination angle is preserved inside the infarcted wall but the fibers are arranged at a higher transmural gradient of inclination angle.

Figure 5.5 presents the quantification of the inclination angle profiles for the heart in Figure 5.4. In Figure 5.5A, the profiles of the inclination angle vs. the wall depth have been plotted for 11 consecutive segments covering the non-infarcted and infarcted regions in the anterior wall (points a to b in Figure 5.4B). These

profiles reveal an increase in the transmural gradient of the inclination angles in the thinned wall of the infarct, confirming the observation in Figure 5.4C. The corresponding structural metrics (described in Methods) have been calculated for each segment and plotted in Figure 5.5B. As the plots demonstrate, there is an increase in the slope and a decrease in the intercept of the fitted linear models in the infarcted segments. In addition, the proportion of left-handed fibers, as quantified by LH-ratio, increases in the infarcted segments (Figure 5.5B). Finally, the infarcted segments exhibit an increase in local incoherency of inclination angles as indicated by the larger error bars (higher variance) in the angle profiles in the infarcted segments (Figure 5.5A,B). We also found significant preservation of trabeculae and papillary muscles at the anterior and septal regions of the infarcted walls. These structures had extreme value of inclination angles (closer to -90° or 90°) indicating apex-to-base fiber orientation.

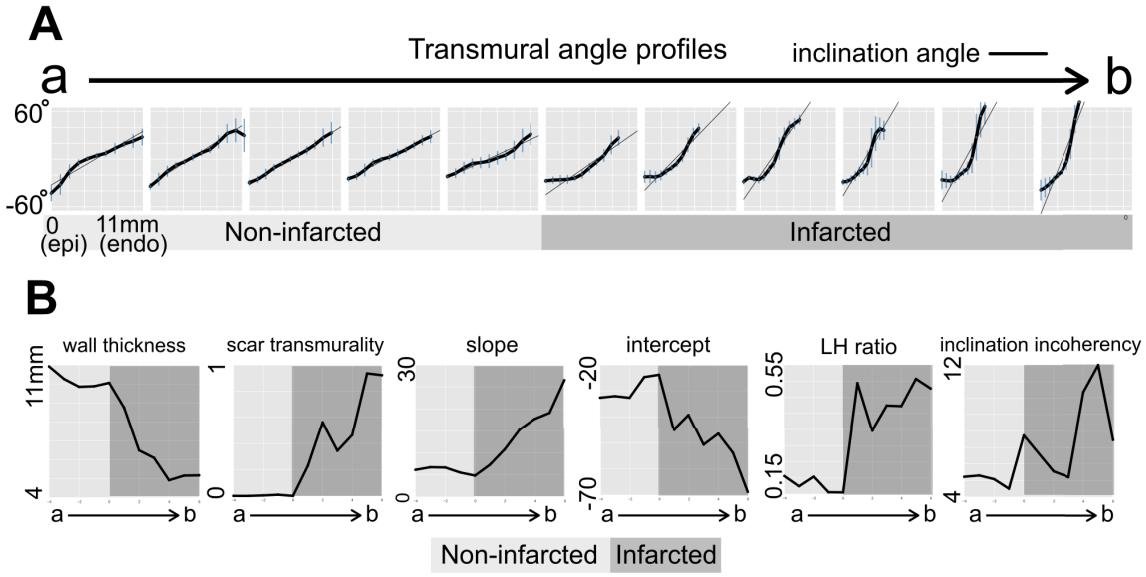

Figure 5.5: Structural remodeling in a section of LV wall from Figure 5.4 containing infarcted and non-infarcted segments **(A)** Inclination angle profiles for 11 consecutive segments corresponding to the region delineated by the white arc in Figure 5.4B. The horizontal axis for each plot represents the depth through the wall as measured from the endocardium. The profiles demonstrate an increase in the transmural gradient of inclination angle. **(B)** Corresponding structural metrics calculated for the 11 segments in panel A and plotted as a function of segment location (a: outside the infarct, b: inside the infarct). The shaded dark area in each plot represents the infarcted segments. The vertical axes for the plots in B represent (from left to right): wall thickness, scar transmurality, slope, intercept, LH (left-handed) –ratio, and inclination incoherency)

Characteristics of microstructural remodeling in the infarcted segments are presented in Table 2. The average and standard deviation values of the structural metrics were computed over 3344 infarcted and 2432 control segments. These results show that the epi-to-endo range of inclination angle profile is predominantly preserved inside the infarcted segments ($109.92 \pm 26.15^{\circ}$ infarcted vs. $113.94 \pm 16.96^{\circ}$ control, $p < 0.001$) and that on average, the fibers run parallel to the wall with a small mean imbrication angles ($1.08 \pm 16.63^{\circ}$ infarcted vs. $1.69 \pm 8.18^{\circ}$ control, $p < 0.001$). In addition, there is an increase in both the inclination incoherency ($9.61 \pm 3.19^{\circ}$ infarcted vs. $6.27 \pm 1.90^{\circ}$ control, $p < 0.001$) and the

imbrication incoherency metrics (8.14 ± 3.67° infarcted vs. 6.17 ± 3.28° control, $p < 0.001$) at the infarcted regions. The transmural slope of the inclination angle showed a significant increase inside the infarcted segments (21.42 ± 18.65 °/mm infarcted vs. 15.21 ± 4.72 °/mm control, $p < 0.001$) confirming our observation from Figure 5.4. Additionally, in comparison to the control segments, the infarcted segments demonstrated a 37% increase in LH-ratio (52 ± 0.22 infarct vs. 0.38 ± 0.14 control, $p < 0.001$), as well as a 16% decrease in circumferential-ratio and a 32% decrease in RH-ratio (Table 5.2).

	Mean ± STD	
Quantity	Infarcted Segments	Control Segments
Wall thickness (mm)	5.06 ± 2.99	7.50 ± 2.27
Scar transmurality	0.47 ± 0.30	0
Inclination Angle Span°	109.92 ± 26.15	113.94 ± 16.96
Slope (°/mm)	21.42 ± 18.65	15.21 ± 4.72
Intercept°	-60.85 ± 28.56	-53.86 ± 14.80
r^2	0.69 ± 0.23	0.91 ± 0.09
Imbrication Angle Mean°	1.08 ± 16.63	1.69 ± 8.18
Inclination incoherency°	9.61 ± 3.19	6.27 ± 1.90
Imbrication incoherency°	8.14 ± 3.67	6.17 ± 3.28
LH-ratio	0.52 ± 0.22	0.38 ± 0.14
Circumferential-ratio	0.26 ± 0.17	0.31 ± 0.11
RH-ratio	0.21 ± 0.18	0.31 ± 0.11

Table 5.2: Characterization of the structural remodeling in infarcted and control segments. See the Methods for the definition of the parameters. P<0.001 for all the pairwise Student T-tests.

Next, we studied the relationship between the level of structural remodeling and the extent of the infarct. Figure 5.6A presents the association of wall thickness with the scar transmurality, as obtained from all infarcted segments. This figure

demonstrates significant wall thinning in the segments with scar transmurality greater than ~30%. The scatter plot in Figure 5.6B shows that the inclination angle range correlates weakly with scar transmurality (correlation coefficient r = 0.18). Finally, slope correlated with scar transmurality (r=0.36) and importantly, it demonstrated a stronger linear correlation with the inverse of wall thickness (r = 0.59, Figure 5.6D,E) than scar transmurality.

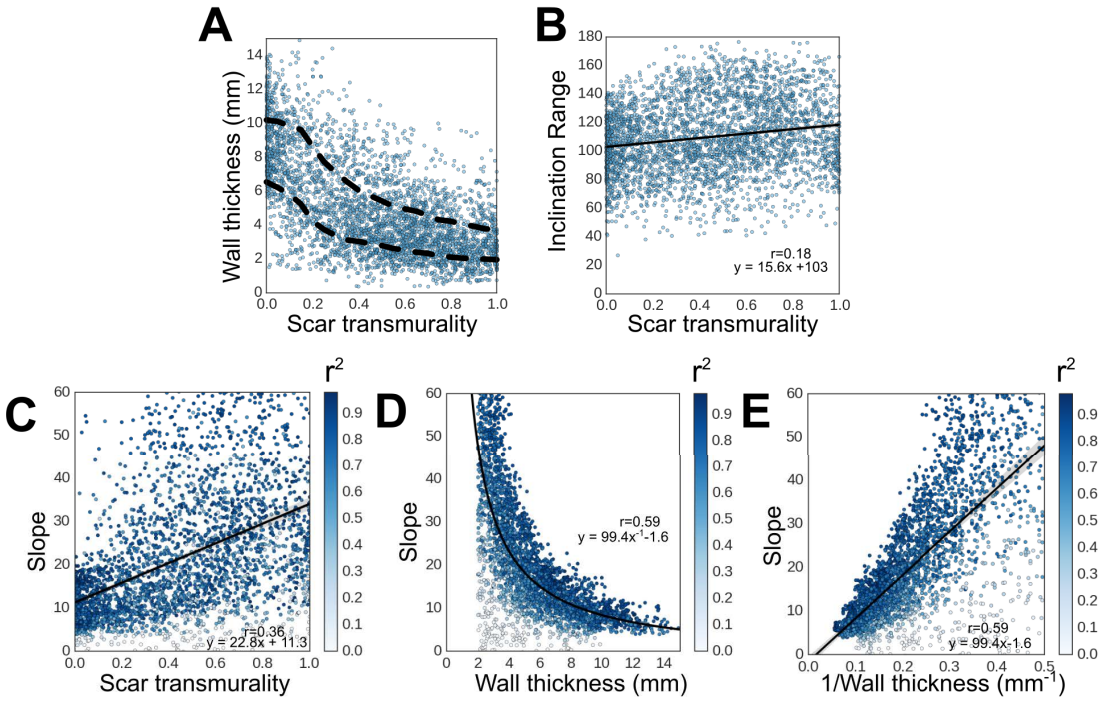

Figure 5.6: Association of the level of structural remodeling with the extent of the infarct. The scatterplots represent the pair-wise relations of the metrics calculated from n ~ 3,700 infarcted segments (see Methods). Each segment is represented by a data point on the plots. In (A), the dashed black lines represent the 25-75 percentile region and in (B-E) the solid dark lines represent the fitted models to each plot. The points in (C-E) have been color-coded based on r^2 (coefficient of determination of the fit for calculation of slope for each data point). Slope correlates inversely with the wall thickness (correlation coefficient r = 0.59 in D and E).

When all voxels were classified as fibrotic ($n \sim 6.5\times10^5$), non-fibrotic inside the infarcted segments ($n \sim 1.4\times10^6$), or control ($n \sim 1.2\times10^6$) and plotted together as a function of *normalized* wall depth, an interesting trend appeared: the fibrotic voxels tend to cluster within the endocardial half of the wall (Figure 5.7A) and non-fibrotic fibers inside the infarcted segments tend to cluster within the epicardial and midwall portion of the wall (Figure 5.7B). Importantly, the transmural epi-to-endo inclination angle function within the infarcted segments (Figure 5.7D) is very similar to that of the control segments (Figure 5.7C), indicating a preservation of the underlying structural anisotropy within the infarcted segments. Finally, the plot constructed from the data in the infarcted segments demonstrates a higher variance around the average at each point across the wall, and has a slightly lower inclination angle at the endocardium in comparison to the corresponding plot from control segments (Figure 5.7C,D).

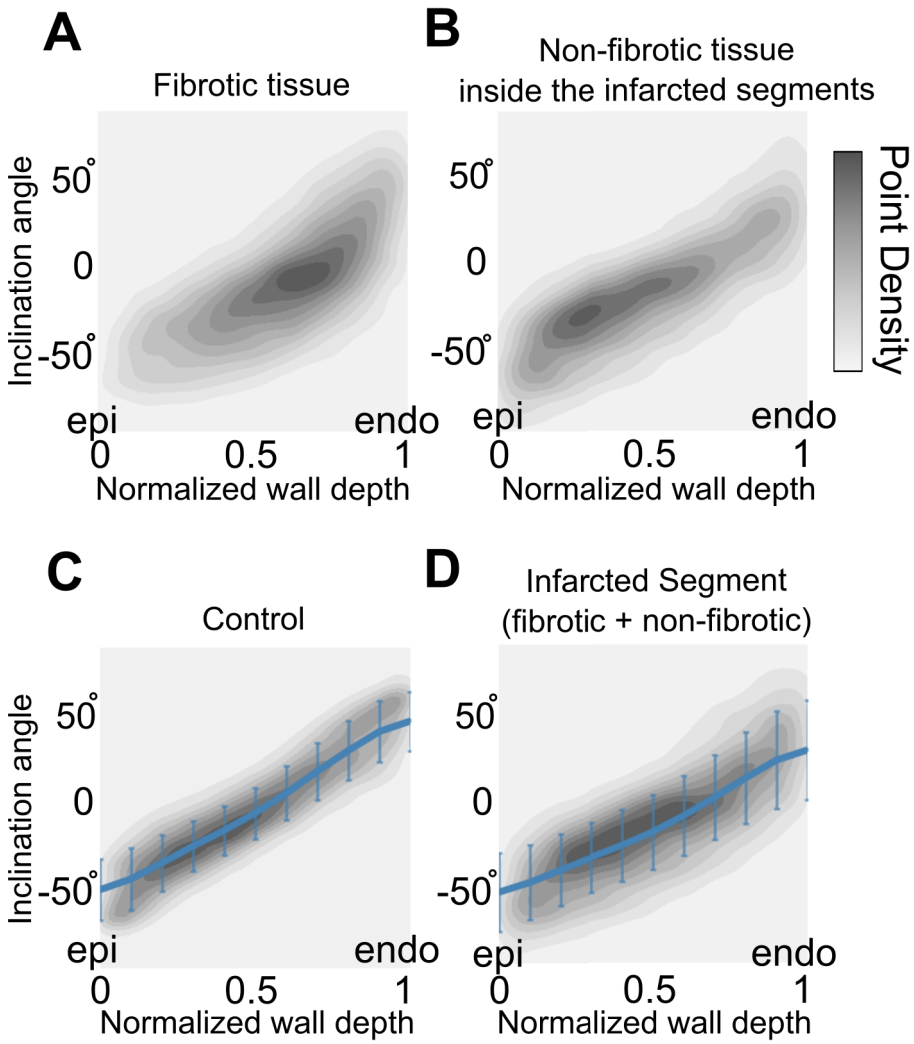

Figure 5.7: Average inclination angle profiles as a function of normalized wall depth (0: epicardium, 1: endocardium). The voxel data corresponding to different tissue types (A-D) are aggregated and plotted in each panel, with the gray-maps representing the point density: **(A)** Fibrotic tissue inside the infarcted segments, and **(B)** non-fibrotic tissue inside the infarcted segments. The point density of the fibrotic tissue is localized at the sub-endocardium. **(C)** Control segments from the normal hearts and **(D)** infarcted segments (include both fibrotic and non-fibrotic voxels). In (C) and (D), the average of the inclination angles have been calculated at different wall depths and represented by blue lines with the error bars illustrating the standard deviation. The control and infarcted segments demonstrate similarities in the inclination angle profiles.

5.3.4 Diffusion Eigenvector Orientation in the Infarcted Human Heart

To examine infarct remodeling in the human heart with prior history of MI, fiber visualization was performed in a similar way as in the porcine hearts. Figure 5.8 presents a short-axis (A) and a long-axis (B) view of the non-diffusion weighted image (left) as well as the fiber visualization (middle and right) in this heart. In these views the infarcted area is identifiable by the significant wall thinning at the anteroapical LV region (left panels). As seen in the middle and right panels, the diffusion eigenvectors inside the thinned wall of the infarct demonstrate preservation of the original epi-to-endo transmural fiber angle pattern, but with a higher gradient. These observations are further confirmed by the angle profiles calculated from two segments selected inside and outside the infarct (Figure 5.8C). The finding of preservation of the structure in the infarcted wall in this human heart is consistent with that from the infarcted porcine hearts.

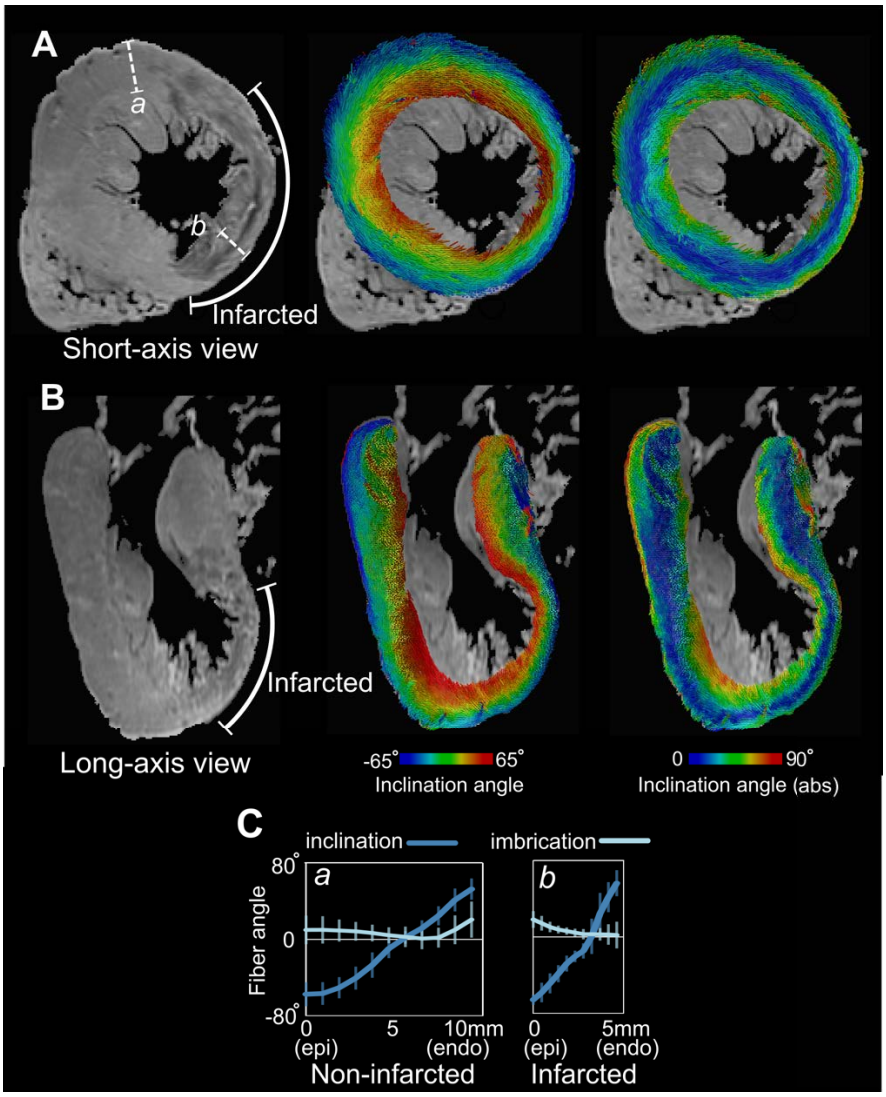

Figure 5.8: Fiber visualization in a human LV with myocardial infarction. **(A)** short-axis view and **(B)** long axis view of (left) the non-diffusion-weighted image, and eigenvector visualizations color-coded with (middle) inclination angle and (right) absolute value of inclination angle. The infarcted wall is identifiable with wall thinning at the anterioapical region of the LV as is demarcated in the non-diffusion-weighted images. The eigenvector maps show preservation of the original orientiation inside the infarct. **(C)** Transmural angle profiles measured in two segments selected in non-infarcted and infarcted regions (*a* and *b* in panel A left). The local wall thickness in these two segments are ~10mm and ~5mm respectively. The plots reveal an increase in the transmural gradient of inclination angle inside the thinned wall of infarct.

5.4 Discussion

In this work, we studied the microstructural remodeling in infarcted porcine hearts and in a human heart non-destructively at sub-millimeter resolution. To do so, we used a customized DTI sequence on a clinical scanner (to accommodate the large specimen) that allowed acquisition of data over long scanning times with high image stability. This, in addition to the high SNR and low artifact characteristics of the 3D spin echo sequence used here, resulted in high image quality and high spatial resolution. By combining this technique with high-resolution LGE imaging, we were able to provide reconstructions of both fiber architecture and scar distribution in intact hearts with an unprecedented level of detail. The sub-millimeter voxel size of the data (voxel volume: 0.432 mm^3) resulted in an average of 8 voxels across the infarcted wall, allowing for the measurement and characterization of the structural remodeling in the zone of infarct, a task that has previously been particularly challenging for DTI due to significant infarct wall thinning and limited image resolution [121]. Importantly, it enabled us to systematically quantify the transmural pattern of diffusion eigenvector orientation in eight porcine infarcts and to study the association between the level of structural remodeling and the extent of the infarct. Finally, we applied this technique to a human heart specimen to assess the remodeling at the thinned infarcted wall in a human heart.

The measurement of diffusion scalars in infarcted porcine hearts demonstrated a 48% increase in MD and a 40% decrease in FA inside the scar. Similar changes in MD and FA have been reported in DTI studies of myocardial infarcts in various species [89, 118, 119, 121, 126]. The increase in MD is indicative of less restricted diffusivity and hence, a larger diffusion volume for water molecules inside the scar. Myocyte death and subsequent collagen deposition following MI could explain the

increase in diffusion volume. Further, these changes lead to alterations in the relative degree of diffusion anisotropy in the tissue, and therefore could be a factor in the reduction of FA. Note that that the dispersion of diffusion eigenvector angles within a voxel could alone lead to a decrease in the measured FA due to an averaging effect. While fiber dispersion exists in a normal LV due to the epi-to-endo transition of inclination angle, an increase in this coherent dispersion (such as that shown in Figure 5.5A) could in principle reduce the FA. This would be particularly true for lower image resolution estimates of FA. In addition to this, incoherent dispersion of fibers at the infarct (fiber disarray) could have a significant role in the reduction of FA inside the infarct. Using histological characterization of rat infarcts, Chen et al [89] found a good correlation between the amount of fiber disarray and the decrease in FA value. The extent to which factors like fiber dispersion and morphological changes in tissue composition contribute to the measured FA value is unknown and requires further investigation. In our study, despite the lower anisotropy inside the infarct, the measured FA in the majority of infarct regions was greater than that of the isotropic water, which revealed that the chronic scar was mostly comprised of anisotropic structures.

The presence of diffusion anisotropy allowed for studying the diffusion eigenvectors in the collagenous scar. The visualization results showed a considerable coherency in the alignments of diffusion eigenvectors in the scar tissue. This is in agreement with histological studies demonstrating that the scarred tissue in the porcine heart has a high content and high alignment of collagen [127]. However, we also found that the coherency of the vector field in the infarct was lower than that of normal tissue, as quantified by the angle incoherency metrics. Furthermore, the orientation of the eigenvectors at the infarct was found to generally follow the pattern of the original fiber orientation, i.e. left-handed fibers at the epicardium to right-handed fibers at the endocardium. The wall thinning at

the infarcted segments led to an increase in the average epi-to-endo gradient of fiber angle (slope in Table 2, and Figure 5.5A). This result is generally consistent with the previous findings in rats [89] and sheep [123] and is in contrast to another study in rats that reported perturbation of the infarct structure [128]. In the current study, we provided further evidence for the preservation of fiber angles and the increase in the slope in chronic porcine infarcts and a human infarct. Finally, the investigation of structural remodeling at different levels of wall thickness (2-12 mm) and scar transmurality (0-1) in our study indicates that the inclination angle range is primarily preserved in the infarcted regions and the increase in the slope is mainly due to geometric changes after wall thinning.

In this study, we found an increase in the proportion of left-handed fibers inside the infarcted segments of porcine hearts, which had also been observed in two previous studies of human hearts [120, 125]. We can speculate that this could be due to non-uniform wall thinning across the wall; the sub-endocardial wall and midwall are more likely to be affected by ischemia and undergo more thinning. Using high-resolution LGE imaging, we indeed observed non-uniform distribution of scar across the wall with fibrosis more concentrated at the sub-endocardial and midwall sub-layers of the infarcted wall in porcine (Figure 5.7A). In general, despite slight differences in the shapes of the angle profiles, there was a remarkable similarity in the trend of inclination angle between the control and infarcted segments. The preservation of the trend of inclination angle profile was also observed in the thinned wall of the single human heart in the study.

The organization of collagen fibers in the scar is influenced by structural and mechanical factors after MI [129]. The original extracellular matrix (ECM) acts as scaffold for the deposition of the new collagen after MI [129]. In addition, the passive stretch of the infarcted tissue by the surrounding myocardium could influence the collagen alignment and hence the anisotropic structure of the scar [130]. The extent to which these factors contribute to the scar structure is not

known. Our observations in porcine and human heart suggest that the existing ECM might play a significant role in the alignment of the collagen fibers, as the general transmural patterns of fiber angles are preserved inside the scar. This information could guide therapeutic attempts such as tissue engineering and regenerative medicine approaches in treatment of infarct, as the ECM orientation is likely to determine the orientation of the regenerative myocytes [39].

Accurate structural data is essential for the construction and validation of whole-heart computational models [105, 131–135]. These models have enabled advancements in the understanding and treatment of cardiac function/dysfunction. The DTMRI-derived data of normal hearts has been utilized by many groups to accurately and non-destructively represent the fiber orientation in cardiac models [136]; however, there is paucity of such data in infarcted hearts, particularly in large animal and human hearts [136]. The data presented here provides unprecedented detail about myofiber orientation and scar geometry in infarcted hearts. This data could be employed to construct high-resolution image-based models to investigate the mechanistic links between infarct-related arrhythmias and the structural remodeling such as fibrosis geometry and fiber arrangement [137]. In addition, the 3D information regarding the collagen fiber orientation in the intact scar as provided here could improve the accuracy of the modeling approaches aimed to understand the mechanical role of passive scar on post-MI ventricular function [40, 42]. These could ultimately lead to optimal design of therapies aimed at modifying the electromechanical properties of infarct [39, 41].

Limitations: This study has a few limitations. First, although the main findings from the analysis of the porcine hearts were generally in agreement with the fiber orientation pattern in the human heart in this study, the single human specimen was not sufficient for a full characterization of infarct remodeling in human hearts. Second, despite sub-millimeter resolution of the imaging with average of ~8 voxels across the wall in the infarct, we excluded the regions with wall thickness less than

2 mm to ensure reliable measurement of transmural angle profile with at least ~4 voxels across the wall; this excluded less than 2% of the total infarcted wall. Finally, the fixation process could have affected the baseline values of diffusivity such as FA and MD in our study [138]. However, it has been shown that it does not change the eigenvector orientation significantly after infarction [138], so we do not believe it has affected the main findings of the study.

Chapter 6

High-Resolution Computational Modeling to Investigate the Role of Scar Geometry in Ventricular Tachycardia

6.1 Introduction

Ventricular arrhythmia is a leading cause of morbidity and sudden death in the industrialized world [115]. Ventricular tachycardia (VT) is a life-threatening rapid heart rhythm disorder that frequently occurs in the presence of myocardial infarction (MI) [139]. Structural and electrophysiological remodeling at the infarcted tissue causes conduction irregularities that could lead to the formation of reentrant circuits at the whole heart level [140, 141]. In particular, it has been shown that surviving myocardial fibers within the infarct could facilitate such arrhythmias by providing tortuous conducting pathways for the electrical activation [47]. However, the detailed mechanisms in which these complex structures contribute to reentry circuits at the whole heart level are incompletely understood, due to lack of detailed knowledge about the 3D architecture of the infarct in intact hearts. Such information obtained from high-resolution structural data could enhance the understanding of the infarct-related arrhythmias and thus lead to improvements in the detection of optimal targets for therapies such as cardiac ablations.

Late Gadolinium Enhanced (LGE) MRI is the gold-standard technique for non-invasive imaging of myocardial infarct in patients [142]. The location and distribution of the infarct obtained from LGE-MRI has been previously correlated with the global risk for arrhythmia. For example, the extent of the Gray Zone (GZ), the intermediate intensity regions in the LGE images, has been associated with increased susceptibility to ventricular arrhythmias [143, 144] and post-myocardial infarction mortality in patients [145]. Further, it has been shown that the critical isthmus sites of ischemic VTs are located at the regions of tissue heterogeneity as characterized by GZ in MRI [146]. Despite the exceptional capability of LGE-MRI in imaging 3D infarct structure, the current clinical LGE-

MRI is limited in providing details regarding small features of infarct and surrounding viable tissue due to low image resolution.

In this study, we provide a novel structural data on the infarct geometry using 3D high-resolution ex vivo LGE imaging of eight chronically infarcted porcine hearts. This data was obtained in the study in Chapter 5. Using this data we identify and systematically characterize the detailed geometry of the infarct and viable tissues surrounding the infarct at a voxel size more than two orders of magnitude smaller than that of a typical clinical LGE imaging. Further, to study the infarct geometrical contributions to VTs, we employ these data and the corresponding subject-specific fiber orientations from DTMRI acquisitions to construct biophysically and anatomically detailed models of infarcted hearts. These models were used in simulations to demonstrate the morphology of reentrant circuits in the context of detailed scar geometry. Further analysis of VT morphologies enabled us to characterize the viable tissues that contribute to the reentry circuits. The new insights obtained from this study could have significant implications for the identifications of the structural substrates for VTs.

6.2 Methods

6.2.1 Induction of MI and Specimen Preparation

In n=8 porcines, the mid-left anterior descending coronary artery (LAD) was occluded for 120 mins to create anteroapical infarction. As a gold standard for MI imaging, Gd-DTPA (Magnevist®) was injected 20 minutes before animal sacrifice. Detailed description of the sample acquisition and preparation has been provided in the Methods section of Chapter 5. The average age of the infarction in the animals was 6.9±2.9 months.

6.2.2 Image Acquisition; Late-Gadolinium Enhanced (LGE) MRI

To image the infarct architecture at a high-resolution, Late-Gadolinium Enhancement (LGE) MRI was performed *ex vivo* using a T1-Weighted Gradient Echo sequence immediately after the excision (Chapter 5). The imaging was performed with the following scan parameters: acquired resolution 0.25x0.25x0.50 mm^3, reconstructed voxel size: 0.25x0.25x0.25 mm^3, echo time (TE)=2.3 ms, repetition time (TR) = 12ms, scan duration: 1hr. Subsequently, the specimens were fixed in 10% buffered formaldehyde (>40 days) for future diffusion imaging

6.2.3 Image Acquisition; Diffusion Tensor Imaging

Subject-specific fiber orientation was obtained for all the hearts using Diffusion Tensor Imaging technique as developed previously in Chapter 3 and was applied to infarcted hearts in Chapter 5. Typical MR imaging parameters were: TE = 63 ms, TR = 504 ms, number of diffusion encoding directions = 15, maximum b-value = 800 s/mm^2, acquired voxel dimension = 0.6x0.6x1.2mm^3, reconstructed voxel dimension (using zero-padding) = 0.4 mm^3 and total scan duration = ~ 42hrs. Diffusion tensor calculation was performed in DTIStudio and subsequently the tensors were co-registered to LGE images using 3D affine transformation. This spatial registration enabled us to reconstruct the fiber structure and scar geometry in the same coordinate system in each heart. Further, the primary eigenvectors were calculated to represent the local orientation of the myofibers in the model. Detailed imaging parameters and sample preparation have been presented previously in Chapter 5.

6.2.4 Whole-Heart Model Construction

The myocardial tissue including the left and right ventricles were segmented from LGE images using thresholding technique to suppress the dark background. Due to the high resolution of the images, the boundary between the enhanced scar tissue and the non-scar tissue was more easily distinguishable than lower resolution clinical LGE images. An Otsu thresholding (n=2) followed by a level-set segmentation algorithm was applied to divide the myocardial tissue into two regions of (enhanced) scar and non-scar based on the differences in voxel intensity (Figure 6.1A). In addition, the scar boundary voxels (a layer of one voxel outside the segmented scar) were defined as the scar border using morphological dilation. The epicardial fat tissue and other artifacts such as the remaining blood in the chambers were removed manually from the segmentations. Following the segmentation process, 3D finite-element mesh with tetrahedral elements was constructed from the segmented myocardial images using ScanIP software (Simpleware Ltd, United Kingdom). This process yielded volumetric meshes with locally adaptive spatial resolution to preserve the fine details of the scar boundary accurately (Figure 6.2B). A typical generated mesh had ~ 4 millions nodes and ~ 20 millions tetrahedral elements. Subject-specific fiber orientation was mapped onto the mesh from the DTMRI dataset acquired for each heart as described above.

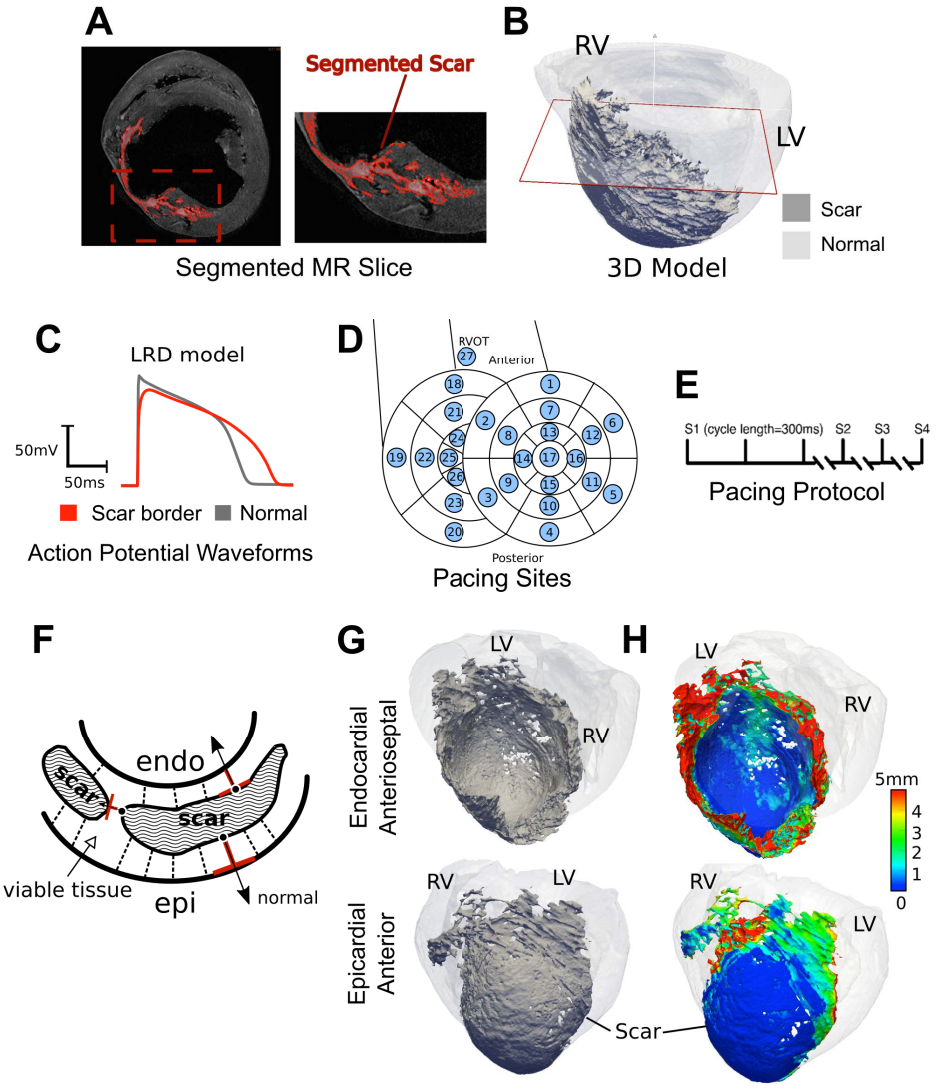

Figure 6.1: Pipeline of the study including imaging, model construction, *in-silico* VT simulation and viable tissue quantification. **(A)** A short-axis slice of T1-W Late-Enhanced MRI acquired at the voxel size of 0.25x0.25x0.5mm^3 .The segmented scar is highlighted in red. **(B)** 3D reconstructed mesh in the same heart as (A) with the scar highlighted in dark grey **(C)** The action potential waveforms used in the simulations for the normal regions (grey) and 250 µm border of the scar (red). **(D)** The pacing sites for the induction of the arrhythmia (27 sites based on modified AHA segmentations). **(E)** The pacing stimulus protocol applied at each site in (C). S2 to S4 are premature stimuli. **(F)** Schematic of a section of the wall illustrating the measurement of the minimal dimension of the viable tissue (MDVT). The MDVT values are mapped onto the scar nodes. **(G)** 3D rendering of the scar as viewed endocardially (top) and epicardially (bottom) in an infarcted heart. **(H)** The same as (G) but with the MDVT color-coded on the scar volume.

6.2.5 Modeling cardiac electrophysiology

Myocyte membrane kinetics in the non-infarcted porcine tissue was represented by the Luo-Rudy dynamic model (LRd) [147], a generic mammalian membrane model used in numerous studies of arrhythmia behaviour [141, 148–150]. Given the medium-to-low complexity of the LRd model, it is a reasonable trade-off in large-scale models such as our whole porcine heart. The same membrane model was used with modifications based on the experimental data from the epicardial border zone of infarcted canine hearts to represent the electrophysiology of the scar border cells (layer of one voxel outside the scar). In particular we modified the normal LRd model with a reduction of 38% in peak sodium current [151], 31%, in peak L-type calcium current [152], and 30% and 20% in peak potassium currents IKr and IKs respectively [153]. Effectively, this led to a longer action potential duration, a smaller upstroke velocity and lower peak action potential amplitude in scar border compared to that of the normal myocardium, consistent with experimental recording of the infarct border zone [46]. Simulated action potential waveforms associated with normal and modified border zone single cells are presented in Figure 6.1C. Finally, the scar region was effectively modeled as electrically inactive by removing the inner scar nodes from the mesh prior to the simulation.

6.2.6 Simulation Protocol and *in-silico* VT Induction

Electrical wave propagation was modeled by the monodomain formulation, and the simulations were performed using the software package CARP (Johns Hopkins University and University of Bordeaux) on a parallel computing platform; numerical details of the finite-element simulations have been described in previous publications [56, 154]. In attempt to induce arrhythmia in each model, 27 pacing sites were selected uniformly throughout the heart according to the modified AHA segmentation (Figure 6.1D), and a programmed electrical stimulation was

performed from each site (Figure 6.1E). The sequence of stimulation comprised of three beats of S1 at the cycle length (CL) of 300 ms, followed by premature stimuli S2. The timing between S1 and S2 were progressively shortened until VT was induced. If VT was not induced at S2, a second premature stimulus (S3) was delivered after S2 in a similar way. If an induced VT was self-sustained for 2s after the last stimulus, it was defined as sustained VT and considered for further analysis.

6.2.7 Quantification of the Spatial Extent of Viable Tissues Surrounding the Scar

To systematically identify and characterize the extent of the surviving tissue surrounding the scar, we measured the minimal dimension of the viable tissue (MDVT) surrounding the scar, and incorporated that information onto the 3D scar geometry to create new scar maps (Figure 6.1F-H). To make this measurement, first a distance map was created on the non-scar nodes by calculating the distance of each node to the closest boundary surface (i.e. the boundary surfaces between scar and non-scar or tissue and bath). Second, for each node on the scar surface, the normal vector to the surface was extended outward from its origin on the scar boundary to the closest intersecting boundary (either another scar boundary or tissue-bath boundary). This led to a line that traversed non-scar tissue with end-points on scar and another boundary surface (red lines in Figure 6.1F). Finally, MDVT was defined on the scar boundary nodes using the following formula: $min(l,2d_{max})$, where l represents the 3D length of the normal line described above and d_{max} is the maximum value of the pre-calculated distance map along the normal line. MDVT value thus reflects the spatial extent of the viable tissue at the thinnest direction. When the 3D scar geometry (Figure 6.1G) is color-coded with the MDVT values, the spatial distribution of the surviving myocardium surrounding the infarct is revealed (Figure 6.1H). We used MDVT to identify the

complex viable tissue surrounding the scar and to quantify the spatial extent of such tissue.

6.2.8 Characterization of Reentry Pathways

The sustained VT circuits were analyzed in the spatiotemporal domain to obtain information on the VT type (single reentry or figure of eight), location across the wall (epicardial, transmural or endocardial) and VT cycle length. In addition, the reentry circuit was localized by spatially tracking the excitation wavefront in one cycle of reentry. This process was performed by manually placing seed points along the fastest route of the reentry based on the activation contours and voltage maps, followed by cubic interpolation to achieve 100um distance between adjacent points on the pathway. In the case that multiple fastest routes were found in a section of reentry circuit (e.g. when the wave is traveling outside the scar and a large mass of normal tissue is activated simultaneously leading to activation contours with low curvature), the route that formed the smallest reentry loop was selected. For the figure of eight reentries, only one loop of the circuit was chosen. This process was repeated for all the simulated reentries with unique morphologies.

We next characterized the viable tissues contributing to the reentry pathways, by measuring the MDVT values on the pathways. To do so, for each point on the pathway, the closest node on the scar border was found and the MDVT value of that point was assigned to the pathway point. As a result, each point on the pathway had a corresponding value of MDVT representing the minimal dimension of the local viable tissue at that location on the reentry circuit.

6.3 Results

6.3.1 Characteristics of Simulated VTs

From total of 216 programmed pacing simulations in eight hearts, 72 VTs were successfully induced. 23 unique morphologies were identified from the above VTs and were studied further (2.9 ± 1.8 unique morphologies per heart, mean cycle length of 196 ± 62 ms).

Reentries traversed thin viable tissues surrounding the scar with complex geometry. The location and the geometry of these viable tissues varied among hearts. Figure 6.2 presents the induction of a sub-epicardial reentry in an infarcted heart (CL = 220 ms). The reentry was initiated by unidirectional block at the entrance of a tube-like channel of viable tissue that runs inside the infarct sub-epicardially (Figure 6.2A). Following the block, the wave enters the channel from the distal side (Figure 6.2B,C) and propagates inside the channel. The channel has an irregular zig-zag shape with total length of about 30 mm (Figure 6.2D). The exit site of the wave is located at the proximal end of the channel.

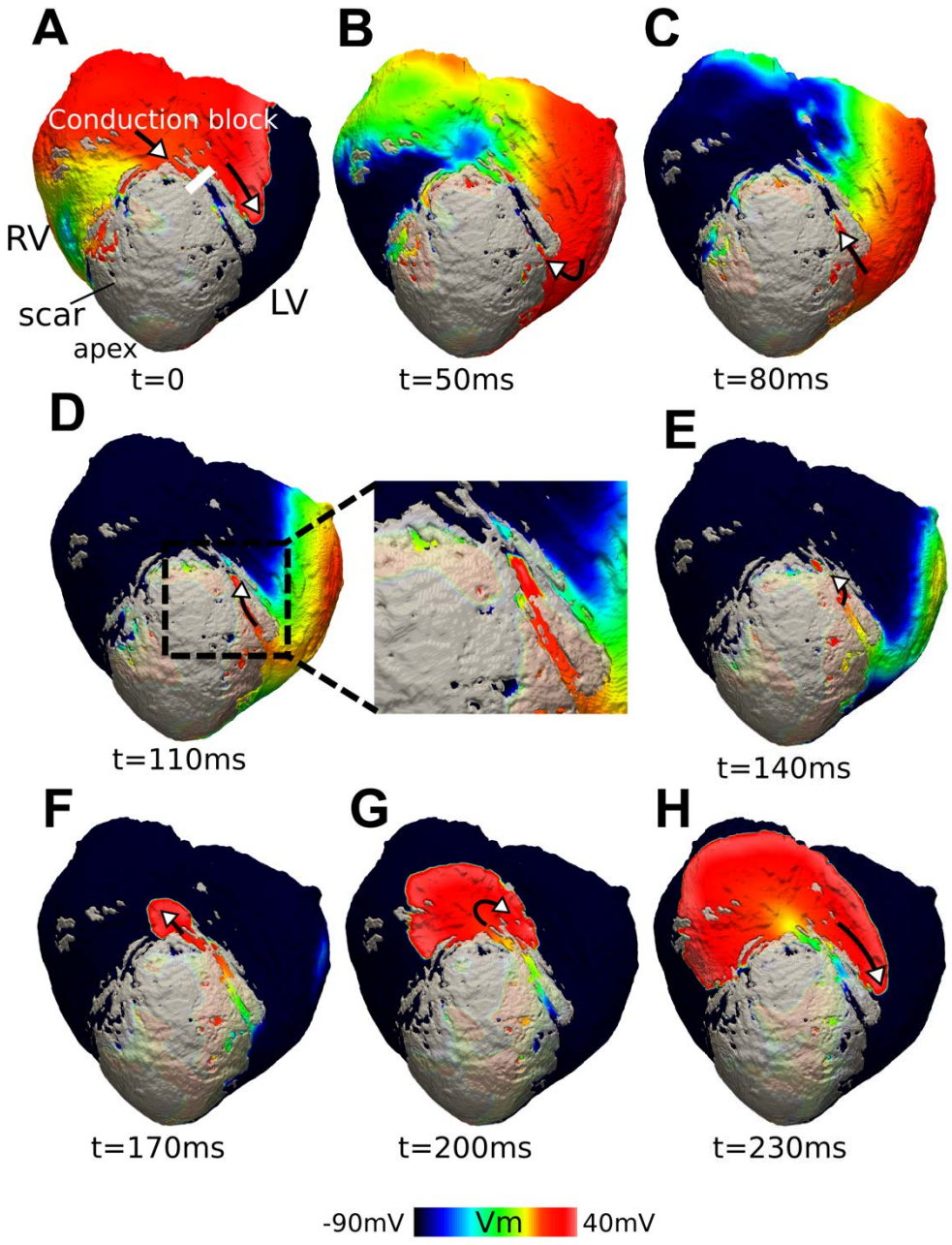

Figure 6.2: Formation of reentry through a sub-epicardial channel of viable tissue in heart 5. VT was induced by programmed stimulation from posterior wall (site 4). **(A)** Unidirectional block occurs at the location of white solid line in (A), **(B-E)** The wave enters the channel from the distal end and meanders inside the channel (dashed black box in D). **(F-H)** Wave exit and maintenance of reentry. VT cycle length is 220 ms. The length of the epicardial channel is approximately 30 mm and the path length is 74 mm.

In Figure 6.3 an example of a sub-endocardial VT is demonstrated (CL = 140ms). A major portion of the reentry pathway is located within a thin layer of surviving myocardium at the sub-endocardium of the infarct. MDVT map shows the heterogeneity in the thickness of these viable tissues throughout the infarct (Figure 6.3B). These sub-endocardial viable tissues were frequently observed in the hearts in this study.

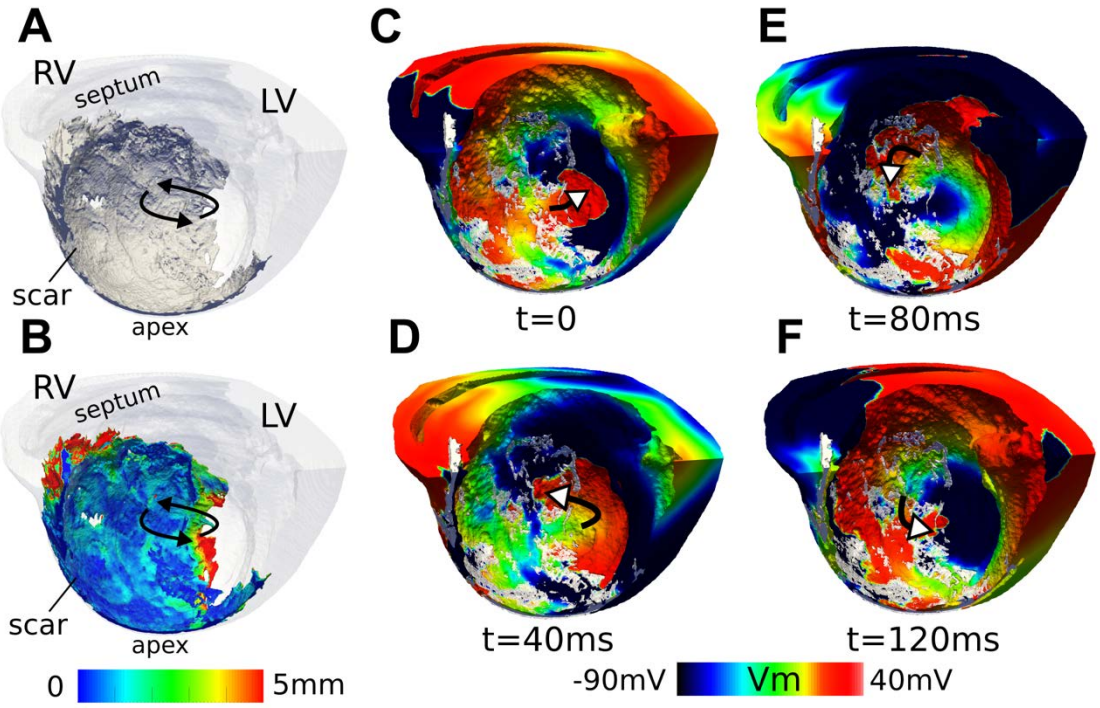

Figure 6.3: A representative reentry traveling through thin heterogeneous layer of sub-endocardial viable tissue in heart 6 (cycle length = 140 ms) **(A)** A septal cross section of the heart geometry demonstrating the scar (gray) and non-scar myocardium (white) as viewed from the endocardium. **(B)** Same view as (A) with the MDVT values mapped onto the scar geometry representing the thickness of viable tissue at the endocardium. **(C-F)** Voltage maps demonstrating the activation in one reentry cycle. The majority of the reentrant pathway is located within the thin viable tissue at the sub-endocardium (black arrows in A and B).

Five of the unique VT circuits traversed the scar transmurally and had breakthroughs at the epicardial and endocardial surfaces. An example of such reentry in heart 7 is presented in Figure 6.4 (CL = 240 ms). In this case, the activation wavefront travels through a region of viable tissue inside the infarct and has a breakthrough at the epicardium (Figure 6.4A). Despite the scar tissue being transmural and extending to the epicardial surface (Figure 6.4B), the surviving myocardium at the mid-layer provides a meandering pathway for the wave to travel from one side of the scar at the endocardium to an exit site and subsequently a breakthrough at the epicardium (Figure 6.4C,D).

Analysis of the location of all the simulated VT morphologies revealed that the majority of the VT circuits were fully or partially located at the sub-endocardium (52% and 78% respectively), while 22% (and 48%) of the VTs were fully (or partially) located at the sub-epicardium. In addition, as mentioned above, 26% of the simulated VTs traversed the scar transmurally and had breakthroughs at the sub-epicardium and sub-endocardium.

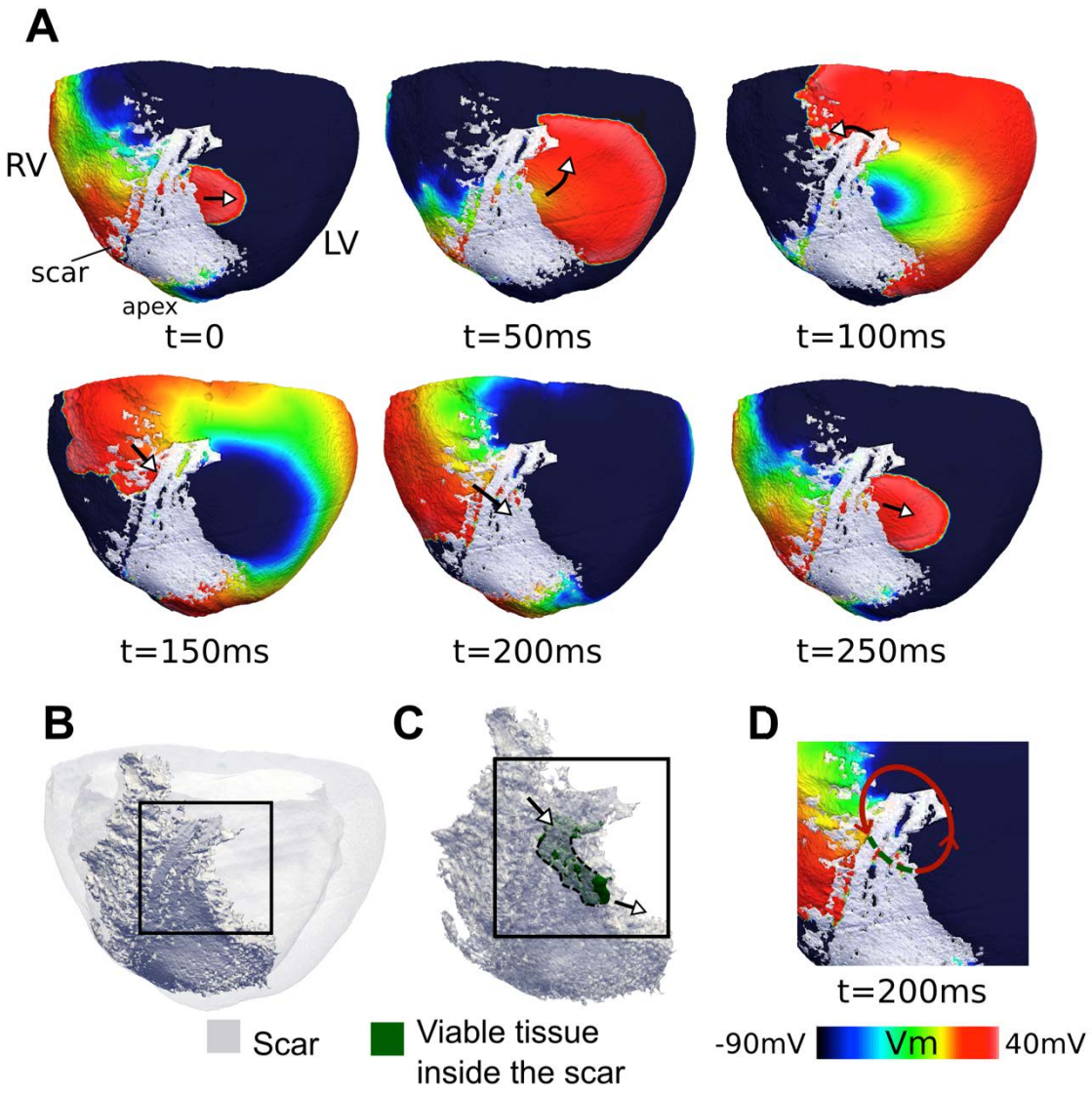

Figure 6.4: Transmural example of reentry circuit in heart 7 (cycle length = 240 ms). **(A)** Voltage maps demonstrate that the reentry traversing the viable tissue inside the infarct and has a breakthrough at the epicardium. **(B)** Anterior view of scar geometry **(C)** Delineation of a portion of a midwall viable tissue embedded inside the infarct (green) that participates in the reentry **(D** View of the black box in (C) showing the reentry cycle and the activation of the tissue within the infarct.

6.3.2 Identification of Viable Tissue Surrounding the Scar using LGE-MRI

As demonstrated above, the VTs were partially or completely located at the surviving myocardium surrounding the scar. Figure 6.5 delineates such viable tissues using short-axis slices of high-resolution LGE-MRI. In Figure 6.5A,C, there is a layer of sub-endocardial and sub-epicardial viable tissue with varying thickness. In Figure 6.5B, a thin viable tissue is located at the midwall providing a channel inside the infarct, similar to the structure in Figure 6.4 that contributed to the transmural reentry (heart 7).

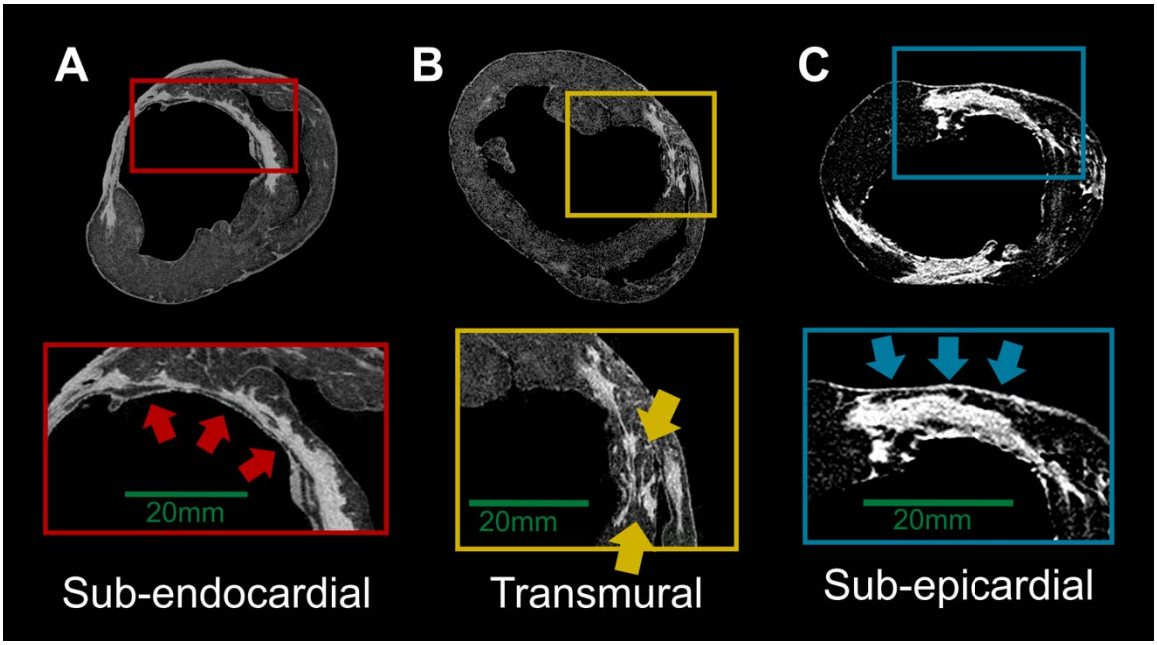

Figure 6.5: Delineation of viable tissues in the vicinity of the scar using short-axis slices of high-resolution LGE-MRI in hearts 5,7 and 8 **(A)** Thin sub-endocardial layer of viable tissue (red arrows), **(B)** transmural viable tissue located inside the infarct (yellow arrows) and **(C)** sub-epicardial layer of surviving myocardium (blue arrows). The layer of surviving myocardium at the sub-endocardium has heterogeneous thickness throughout the cavity.

6.3.3 Characteristics of Reentry Pathways

The 3D pathways of the reentry circuits were tracked as described in the Methods. The average path length in the 23 unique morphologies was 53 ± 14 mm. Figure 6.6 presents pathways associated with two VT morphologies in heart 5. These pathways are highlighted with dashed line on the MDVT maps in Figures 6.6A,D and illustrated separately in Figures 6.6B,E. The MDVT values along each pathway are primarily smaller than 2 mm (Figure 6.6C,F).

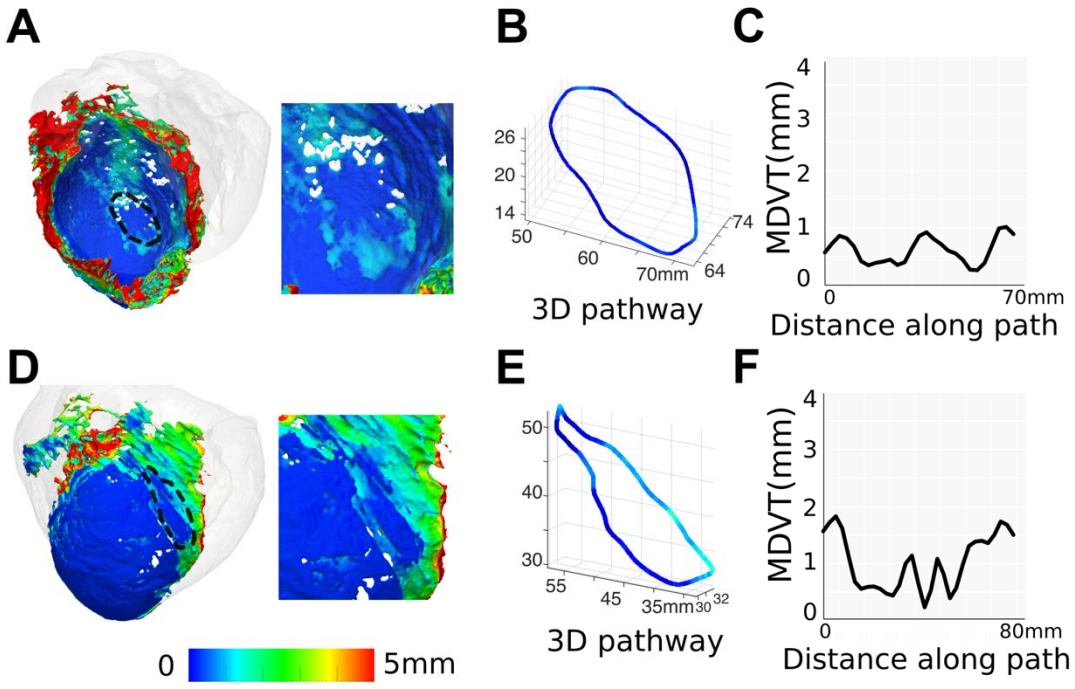

Figure 6.6: Reentry pathway characterization in two representative reentrant circuits. **(A)** MDVT map with the reentry pathway overlaid with dashed black line. The right panel shows the zoomed view of the region of reentry **(B)** The tracked reentry pathway as visualized in 3D and color-coded by MDVT values. **(C)** MDVT as a function of the distance along the reentry pathway. The reentry pathlength is ~ 65mm. **(D)-(F)** Similar to (A)-(C) but in a different VT in the same heart (no. 5) with pathlength of ~ 74mm.

To characterize the thickness of viable tissues contributing to VT in all the simulated VTs, the histogram of the MDVT values have been calculated and

presented in Figure 6.7. The MDVT distribution of all the reentry pathways (red) was compared to the MDVT values from all the nodes at the scar border in the eight hearts (blue). These results reveal a preferential localization of the values in the range of less than ~ 1.5mm for the both distributions. However, despite similarities in the shape of the two histograms, the red plot is marginally localized between 0.25 mm and 1.75 mm; 90% of the points on the reentry pathways have MDVT values of less than 2.3mm. Further, Kolmogorov-Smirnov (KS) statistical test showed that the two data points are not drawn from the same distribution and hence are statistically different (KS statistics = 0.164, p-value <0.001).

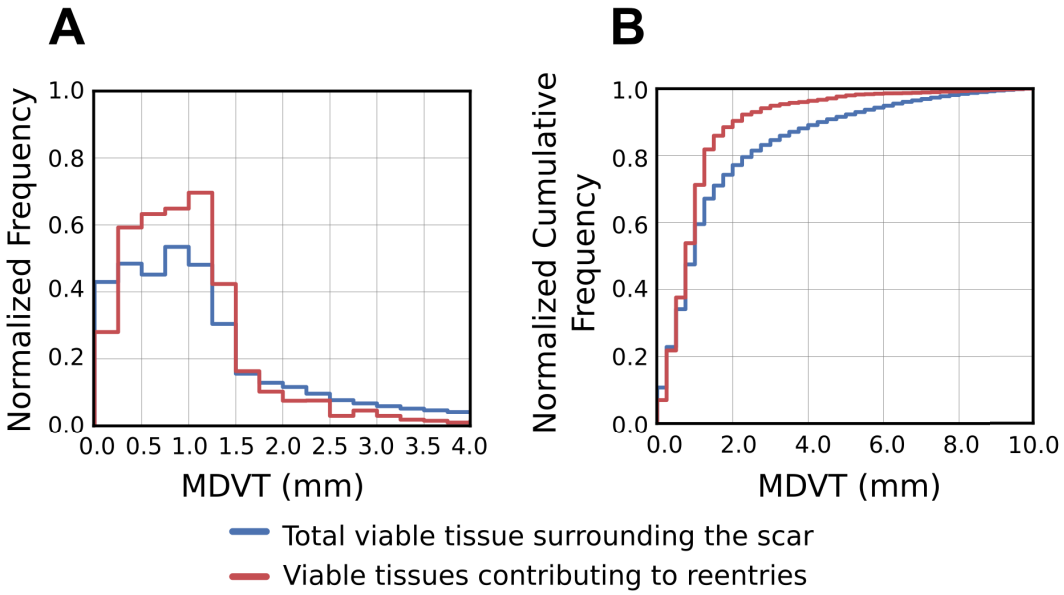

Figure 6.7: Distributions of the minimal dimension of the viable tissues (MDVT) contributing to reentry circuits and the comparison to that of the total tissue surrounding the scar. **(A)** Normalized histograms and **(B)** Cumulative histograms. Blue represents the MDVT distribution of all the viable tissues surrounding the scars in eight hearts, and red shows the distribution for the viable tissues contributing to the reentries (from n = 23 distinct reentry circuits). 90% of the reentry pathways traverse viable tissue of thickness of less than 2.3 mm.

6.4 Discussion

In this study, we constructed high-resolution models of infarcted hearts and employed them in simulations to investigate the contribution of the infarct microarchitecture to ventricular tachycardia. To the best of our knowledge this is the highest resolution biophysically detailed model of infarcted large animal hearts with image-based scar geometry and fiber orientation obtained from *ex vivo* LGE- and DT-MRI. The simulation results showed that the reentry circuits traverse thin viable tissue inside the infarct with complex geometries. The majority of reentries were located at the sub-endocardial layer of viable tissue with heterogeneous thickness distribution.

6.4.1 Modeling Methodology and *in-silico* VT Induction

The application of LGE-MRI *ex vivo* allowed us to image the heart at a much higher spatial resolution (400-fold) and higher image quality than *in vivo* contrast-enhanced techniques by avoiding the heart and respiratory motions. As it has been demonstrated previously [155, 156] a smaller imaging voxel size results in less partial volume averaging effect and therefore less number of mid-intensity voxels in the image. Consistently, we observed sharper boundaries between the scar and the non-scar tissues. We therefore classified the myocardial tissue into two regions of scar and non-scar. Further, to incorporate the electrophysiological remodeling observed at the boundary of the scar, the cell membrane kinetics of the tissue within one voxel (250 μm) outside the scar was modified, to achieve action potential waveforms with lower upstroke velocity and longer duration, consistent with reported values in the literature [46]. The detailed characterization of the electrophysiological remodeling at the border zone is not completely known and requires further investigations using intramural mapping techniques such as plunge electrode recordings. Here we used minimal modeling assumptions based on the

reported findings of the border zone electrophysiology that served our goal to induce reentry in the models and investigate the geometrical contributions to the reentry circuits at the whole heart level.

VT was induced using a programmed stimulation sequence similar to that in a clinical setting. Unlike clinical VT induction, we paced from 27 sites distributed throughout each heart. This aggressive pacing protocol assured induction of more VT morphologies than what would be induced using 3 pacing sites in a clinical setting, and therefore provided us with more data points to characterize the reentrant circuits. Indeed, while all the hearts were inducible using 27 sites pacing protocol, only 3 hearts were inducible when pacing was performed from typical LV apex, RV apex and RVOT locations.

6.4.2 Identification and Characterization of Viable Tissue Surrounding the Scar

A major contribution of this work is imaging and characterization of 3D architecture of viable myocardium surrounding the scar in intact hearts. The presence of viable myocardial fibers at the healed infarct has been shown using destructive histological methods [47, 157]. In agreement with these studies, we found complex regions of viable tissue embedded in the infarct; these regions generally surrounded the scar at the sub-endocardium or sub-epicardium or travelled inside the scar transmurally (Figure 6.5). Efficient visualization and characterization of the dimension of such regions is challenging due to their irregular 3D shape. The MDVT maps defined here, demonstrate the local thickness of viable tissue on the scar surface and provide a systematic way to identify and characterize these structures (Figures 6.3B and 6.6A,D). Using these 3D scar maps, we identified diverse morphologies of viable tissue surrounding the scar including: tube-like channels on the sub-epicardial layer (Figure 6.6D), small patches of viable tissues inside the scar connecting the endo- and epicardium (Figure 6.6A) and

sheets of surviving myocardium at the sub-endocardium or sub-epicardium with varying thickness at different locations of the scar surface (Figure 6.3B). Further, aggregation of the MDVT measurements over all the scar nodes in all the hearts allowed us to provide MDVT distribution plots that are unique determinants of the dimension of the complex underlying viable tissue structures surrounding the scar.

6.4.3 The Linkage between the Viable Tissue Structure Surrounding the Scar and VT

Previous studies have shown the role of small viable myocardium surrounding the scar in the formation of ventricular arrhythmias [157, 158]. We found that the reentry circuits were fully or partially localized in thin viable tissue embedded in the scar. The analysis of the MDVT values on the reentrant pathways demonstrates that the distribution is skewed toward smaller values of MDVT (90 percentile of 2.3 mm, red in Figure 6.7), equivalent to thinner viable tissues. The shape of this distribution is partially influenced by the underlying distribution of MDVT values on the scar (blue in Figure 6.7) of which the values on the reentry pathways are a subset. Further, despite similarities in the shape of the two distributions, we found them to be statistically different, with the reentry distribution having a marginal overhead in the interval of 0.25-1.75 mm. This observation suggests that viable tissues with MDVTs in this interval are more likely to participate in reentries.

In our study, the sub-endocardial viable tissue provided conducting pathways to the majority of the simulated reentrant circuits (78%). The sub-endocardial surviving tissue is believed to be the result of blood supply from the ventricular cavity [159] and have been shown to provide conducting pathways for reentry [160, 161]. This was consistent with our observation that thin layers of viable tissue at sub-endocardium (and sub-epicardium) provide potential pathways for electrical activation inside the scar and also could contribute to reentry. In addition, our

simulation results show that the spatial heterogeneity in the shape and dimension of sub-endocardial (and sub-epicardial) viable tissue could lead to complex activation patterns (Figure 6.3C-F) with heterogeneous conduction velocity and APD. Such electrical heterogeneity due to complex geometry increases the propensity of conduction blocks and hence the formation of reentries. The basic geometrical mechanism of unidirectional block due to steep changes in the tissue thickness has been demonstrated previously [162]. Our study suggests that because of the complexity of scar structure, changes in tissue depth and width could occur simultaneously as the wave travels through the viable tissue and therefore 3D characterization of local tissue structure is needed for a complete understanding of wave activation.

6.4.4 Clinical Implications

The structural information of the infarct obtained from LGE-MRI has been shown to predict the presence of VT substrates in vivo [146, 163]. Image-based simulations obtained from such data have demonstrated promising results on detection of the potential targets for cardiac ablations [164] and risk stratifications [131] in patients with MI. Our study provides further evidence on the important role of 3D infarct structure and particularly the structure of viable tissue on the pattern of electrical activity during VT. The detailed knowledge of the scar geometry and the viable tissue that contribute to VT can help interpret with greater accuracy the findings from electroanatomical mapping and clinical MRI and help to improve the detection of substrates for arrhythmias. A complete understanding of the high resolution details of infarcts in particular will assist in making the appropriate assumptions when modeling from lower resolution clinical images.

Limitations: The reperfusion infarct model used in this study represents the clinical setting in which a coronary occlusion is followed by a revascularization,

therefore the infarct characteristics could not represent the entire population of human infarcts. In addition, due to the limited spatial resolution, viable tissues with dimension of less than 250 μm could not be represented in our model.

Chapter 7

Future Directions

In this thesis we employed high-resolution MR techniques to acquire cardiac structural data at a spatial resolution and image quality that is unprecedented for large animal and human hearts. We further employed this data in computational models to explore the structural features that contribute to reentry. The findings from and the methodologies presented in this thesis could be utilized in various ways to advance clinical and basic cardiac research.

Detailed reconstructions of fiber architecture in human atria, presented in chapter 4, enable the generation of computational models with realistic fiber orientation. These models could be used to investigate basic mechanisms of electrical propagation and, in particular, the influence of anisotropic fibrous structure on the activation patterns at the whole organ level. Experimental studies have demonstrated the effect of atrial anisotropic structure on electrical activity. For instance, it has been shown that sharp changes in fiber orientation and wall thickness in the atrial could lead to conduction blocks even in the absence of structural remodeling [24, 25]. Despite the experimental evidences, the degree to which such features contribute to rhythm disorders has not been systematically studied. Our findings set the groundwork for future studies that address this gap in knowledge by either incorporating this data in modeling methodologies or correlating experimental findings with the fiber maps provided in chapter 4. For example, computational modeling could be used to single out the effect of fiber structure by performing simulation experiments with and without the tissue anisotropy, and study the differences in the electrical activity. Such experiments could be performed in normal condition as well as in the presence of structural remodeling to obtain a full understanding of the effect of the anisotropic structure on dynamics and localization of electrical disturbances particularly the atrial rotors. In addition, there is an increasing number of efforts to study the relationship between the LGE-MRI-derived fibrosis information and the location of substrates

for atrial arrhythmias, as potential targets for cardiac ablation therapy. It would be interesting to investigate whether certain features of fiber structure need to be also considered as targets for cardiac ablation of atrial fibrillation.

The high-resolution models of infarcted hearts with subject-specific fiber orientation and infarct geometry will open many avenues to explore the relationship between VT and structure. Our simulation results in chapter 6 demonstrated the complex viable tissues surrounding the scar that contribute to reentrant circuits and revealed the spatial extent and characterization of such features. One future work would be to use these models to find the structural and electrical characteristics of optimal ablation targets that terminate reentries. Given that this level of information regarding the scar geometry and the surrounding viable tissue is not available using in vivo imaging techniques, these models could serve as valuable tools to explain the high failure rate for cardiac ablations, and potentially propose novel ablation strategies [165].

Patient-specific models are being constructed with the goal of identifying optimal ablation targets and improved risk stratification in the atria and ventricles [108, 131]. The high-resolution data obtained in this thesis could be used in future work to validate and improve these models. Incorporation of realistic atrial fiber architecture data will lead to an improved accuracy over models with simplified fiber orientation. Further, despite increasing attempts at the in vivo acquisition of fiber orientation in the ventricles, such task remains particularly challenging in the atria. Driven by the data provided in this thesis, mathematical techniques (e.g. rule-based or morphing methodologies) need to be implemented to map fiber orientation onto the patients' atrial models based on purely geometrical information. Similar approaches have been adopted in mapping fiber orientation to models of ventricles. Despite the higher inter-subject variability in the geometry and a more complex fiber architecture in the atria, our study showed a remarkable

consistency in the orientation of major bundles in most of the hearts under study that could be promising for the aforementioned mapping techniques. Although future investigations of fiber architecture in larger number of hearts are needed to represent the true diversity in the fiber architecture in the population, the data from the hearts presented here could be served to create first virtual atlas of human atrial fiber architecture.

Lastly, a complete picture of the high-resolution details of infarcts will assist in making the appropriate assumptions when creating patient-specific models from lower resolution clinical images. The integration of realistic fiber orientation in the infarcted hearts, as obtained in chapter 5, could improve the accuracy of these clinical modeling efforts. The findings from chapter 5 suggest that the fiber remodeling in the infarct is highly affected by geometrical factors due to wall thinning. This could simplify building models of infarcted tissue for electrical and mechanical simulations. The exact effect of fiber orientation remodeling on the activity yet to be determined by future simulation studies that compare the results from models with DTMRI-derived fibers and those with fibers obtained from other mapping approaches such as rule-based methods.

Bibliography

[1] R. E. Klabunde., *Cardiovascular Physiology Concepts*, Second Edi. Lippincott Williams & Wilkins, a Wolters Kluwer buisness, 2012.

[2] M. S. Spach, Wt. Miller, P. C. Dolber, J. M. Kootsey, J. R. Sommer, C. E. Mosher, and R. Question, "The functional role of structural complexities in the propagation of depolarization in the atrium of the dog. Cardiac conduction disturbances due to discontinuities of effective axial resistivity.," *Circ. Res.*, vol. 50, no. 2, pp. 175–191, 1982.

[3] B. Taccardi, E. Macchi, R. L. Lux, P. R. Ershler, S. Spaggiari, S. Baruffi, and Y. Vyhmeister, "Effect of myocardial fiber direction on epicardial potentials.," *Circulation*, vol. 90, no. 6, pp. 3076–90, Dec. 1994.

[4] J. E. Saffitz, H. L. Kanter, K. G. Green, T. K. Tolley, and E. C. Beyer, "Tissue-specific determinants of anisotropic conduction velocity in canine atrial and ventricular myocardium," *Circ. Res.*, vol. 74, no. 6, pp. 1065–1070, Jun. 1994.

[5] L. Clerc, "Directional differences of impulse spread in trabecular muscle from mammalian heart.," *J. Physiol.*, vol. 255, no. 2, pp. 335–346, 1976.

[6] a Kanai and G. Salama, "Optical mapping reveals that repolarization spreads anisotropically and is guided by fiber orientation in guinea pig hearts.," *Circ. Res.*, vol. 77, no. 4, pp. 784–802, Oct. 1995.

[7] D. Matematica and U. Pavia, "Spread of Excitation in 3-D Models of the Anisotropic Cardiac Tissue . II . Effects of Fiber Architecture and Ventricular Geometry," *Math. Biosci.*, vol. 171, no. 1998, pp. 131–171, 1997.

[8] D. Roberts, L. Hersh, and A. Scher, "Influence of Cardiac Fiber Orientation on Wavefront Voltage, Conduction Velocity, and Tissue Resistivity in the Dog," *Circ. Res.*, vol. 44, pp. 701–712, 1979.

[9] I. J. LeGrice, B. H. Smaill, L. Z. Chai, S. G. Edgar, J. B. Gavin, and P. J. Hunter, "Laminar structure of the heart: ventricular myocyte arrangement and connective tissue architecture in the dog.," *Am. J. Physiol.*, vol. 269, no. 2 Pt 2, pp. H571–82, Aug. 1995.

[10] K. D. Costa, Y. Takayama, a D. McCulloch, and J. W. Covell, "Laminar fiber architecture and three-dimensional systolic mechanics in canine ventricular myocardium.," *Am. J. Physiol.*, vol. 276, no. 2 Pt 2, pp. H595–607, Feb. 1999.

[11] I. J. LeGrice, Y. Takayama, and J. W. Covell, "Transverse shear along myocardial cleavage planes provides a mechanism for normal systolic wall thickening," *Circ. Res.*, vol. 77, no. 1, pp. 182–193, 1995.

[12] L. K. Waldman, D. Nosan, F. Villarreal, and J. W. Covell, "Relation between transmural deformation and local myofiber direction in canine left ventricle.," *Circ. Res.*, vol. 63, no. 3, pp. 550–562, 1988.

[13] T. Arts, K. D. Costa, J. W. Covell, and A. D. McCulloch, "Relating myocardial laminar architecture to shear strain and muscle fiber orientation," *Am J Physiol Hear. Circ Physiol*, vol. 280, no. 5, pp. H2222–2229, 2001.

[14] M. Vendelin, P. H. M. Bovendeerd, J. Engelbrecht, and T. Arts, "Optimizing ventricular fibers: uniform strain or stress, but not ATP consumption, leads to high efficiency.," *Am. J. Physiol. Heart Circ. Physiol.*, vol. 283, no. 3, pp. H1072–81, Sep. 2002.

[15] D. Gil, A. Borràs, R. Aris, M. Vázquez, P. Lafortune, G. Houzeaux, J. Aguado, M. Ballester, C. H. Li, and F. Carreras, "What a difference in biomechanics cardiac fiber makes," *Lect. Notes Comput. Sci. (including Subser. Lect. Notes Artif. Intell. Lect. Notes Bioinformatics)*, vol. 7746 LNCS, pp. 253–260, 2013.

[16] A. Kadish, M. Shinnar, E. N. Moore, J. H. Levine, C. W. Balke, and J. F. Spear, "Interaction of fiber orientation and direction of impulse propagation with anatomic barriers in anisotropic canine myocardium.," *Circulation*, vol. 78, no. 6, pp. 1478–1494, 1988.

[17] P. S. Chen, Y. M. Cha, B. B. Peters, L. S. Chen, B. B. Peters, L. A. N. S. Chen, and B. Peters, "Effects of myocardial fiber orientation on the electrical induction of ventricular fibrillation Effects of myocardial fiber orientation on the electrical induction of ventricular fibrillation," *Artery*, 2012.

[18] B. Maesen, S. Zeemering, C. Afonso, J. Eckstein, R. a B. Burton, A. van Hunnik, D. J. Stuckey, D. Tyler, J. Maessen, V. Grau, S. Verheule, P. Kohl, et al., "Rearrangement of atrial bundle architecture and consequent changes in anisotropy of conduction constitute the 3-dimensional substrate for atrial fibrillation.," *Circ. Arrhythm. Electrophysiol.*, vol. 6, no. 5, pp. 967–75, Oct. 2013.

[19] F. Fenton and A. Karma, "Vortex dynamics in three-dimensional continuous myocardium with fiber rotation: Filament instability and fibrillation.," *Chaos*, vol. 8, no. 1, pp. 20–47, 1998.

[20] C. S. Henriquez, a L. Muzikant, and C. K. Smoak, "Anisotropy, fiber curvature, and bath loading effects on activation in thin and thick cardiac tissue preparations: simulations in a three-dimensional bidomain model.," *J. Cardiovasc. Electrophysiol.*, vol. 7, no. 5, pp. 424–44, 1996.

[21] N. Trayanova, K. Skouibine, F. Aguel, and K. Skoubie, "The role of cardiac tissue structure in defibrillation," *Chaos*, vol. 8, no. 1, pp. 221–233, 1998.

[22] M. Wellner, O. Berenfeld, J. Jalife, and A. M. Pertsov, "Minimal principle for rotor filaments.," *Proc. Natl. Acad. Sci. U. S. A.*, vol. 99, no. 12, pp. 8015–8018, 2002.

[23] N. Bursac, K. K. Parker, S. Iravanian, and L. Tung, "Cardiomyocyte cultures with controlled macroscopic anisotropy: a model for functional electrophysiological studies of cardiac muscle," *Circ Res*, vol. 91, no. 12, pp. e45–54, 2002.

[24] O. Berenfeld, A. V. Zaitsev, S. F. Mironov, A. M. Pertsov, and J. Jalife, "Frequency-dependent breakdown of wave propagation into fibrillatory conduction across the pectinate muscle network in the isolated sheep right atrium," *Circ. Res.*, vol. 90, no. 11, pp. 1173–1180, May 2002.

[25] M. Klos, D. Calvo, M. Yamazaki, S. Zlochiver, S. Mironov, J. Cabrera, D. Sanchez-quintana, J. Jalife, O. Berenfeld, and J. Kalifa, "Atrial Septopulmonary Bundle of the Posterior Left Atrium Provides a Substrate for Atrial Fibrillation Initiation in a Model of Vagally Mediated Pulmonary Vein Tachycardia of the Structurally Normal Heart," *Circ. Arrhythm. Electrophysiol.*, 2008.

[26] M. Valderrábano, M.-H. H. Lee, T. Ohara, a. C. Lai, M. C. Fishbein, S.-F. F. Lin, H. S. Karagueuzian, P.-S. S. Chen, M. Valderrabano, M.-H. H. Lee, T. Ohara, a. C. Lai, et al., "Dynamics of intramural and transmural reentry during ventricular fibrillation in isolated swine ventricles.," *Circ. Res.*, vol. 88, no. 8, pp. 839–848, Apr. 2001.

[27] R. H. Anderson, M. Smerup, D. Sanchez-Quintana, M. Loukas, and P. P. Lunkenheimer, "The three-dimensional arrangement of the myocytes in the ventricular walls," *Clin. Anat.*, vol. 22, no. 1, pp. 64–76, 2009.

[28] F. P. Mall, "On the muscular architecture of the ventricles of the human heart," *Am. J. Anat.*, vol. 11, no. 3, pp. 211–266, Mar. 1911.

[29] D. D. Streeter, H. M. Spotnitz, D. P. Patel, J. Ross, and E. H. Sonnenblick, "Fiber orientation in the canine left ventricle during diastole and systole.,"

Circ. Res., vol. 24, no. 3, pp. 339–47, Mar. 1969.

[30] D. F. Scollan, A. Holmes, R. Winslow, and J. Forder, "Histological validation of myocardial microstructure obtained from diffusion tensor magnetic resonance imaging," *Am. J. Physiol. Circ. Physiol.*, vol. 275, no. 6, pp. H2308–H2318, Dec. 1998.

[31] P. Savadjiev, G. J. Strijkers, A. J. Bakermans, E. Piuze, S. W. Zucker, and K. Siddiqi, "Heart wall myofibers are arranged in minimal surfaces to optimize organ function.," *Proc. Natl. Acad. Sci. U. S. A.*, vol. 109, no. 24, pp. 9248–53, Jun. 2012.

[32] B. Hall, V. Jeevanantham, R. Simon, J. Filippone, G. Vorobiof, and J. Daubert, "Variation in left atrial transmural wall thickness at sites commonly targeted for ablation of atrial fibrillation," *J. Interv. Card. Electrophysiol.*, vol. 17, no. 2, pp. 127–132, 2006.

[33] R. Kato, L. Lickfett, G. Meininger, T. Dickfeld, R. Wu, G. Juang, P. Angkeow, J. LaCorte, D. Bluemke, R. Berger, H. R. Halperin, and H. Calkins, "Pulmonary vein anatomy in patients undergoing catheter ablation of atrial fibrillation: lessons learned by use of magnetic resonance imaging.," *Circulation*, vol. 107, no. 15, pp. 2004–10, Apr. 2003.

[34] E. M. Marom, J. E. Herndon, Y. H. Kim, and H. P. McAdams, "Variations in pulmonary venous drainage to the left atrium: implications for radiofrequency ablation.," *Radiology*, vol. 230, no. 3, pp. 824–829, 2004.

[35] S. Y. Ho, J. A. Cabrera, and D. Sanchez-Quintana, "Left atrial anatomy revisited.," *Circ. Arrhythm. Electrophysiol.*, vol. 5, no. 1, pp. 220–8, Mar. 2012.

[36] A. L. Wit and R. Rosen, "Pathophysiologic mechanisms of cardiac arrhythmias," *Am. Heart J.*, vol. 106, no. 4, pp. 798–811, 1983.

[37] E. D. Grech, *ABC of Interventional Cardiology*, 2nd ed. John Wiley & Sons, 2011.

[38] S. L. Rutherford, M. L. Trew, G. B. Sands, I. J. Legrice, and B. H. Smaill, "High-Resolution 3-Dimensional Reconstruction of the Infarct Border Zone.," *Circ. Res.*, Jun. 2012.

[39] J. W. Holmes, Z. Laksman, and L. Gepstein, "Making better scar: Emerging approaches for modifying mechanical and electrical properties following infarction and ablation," *Prog. Biophys. Mol. Biol.*, vol. 120, no. 1–3, pp. 134–148, 2016.

[40] J. W. Holmes, J. a Nuñez, and J. W. Covell, "Functional implications of myocardial scar structure.," *Am. J. Physiol.*, vol. 272, no. 5 Pt 2, pp. H2123–H2130, 1997.

[41] G. M. Fomovsky, J. R. MacAdangdang, G. Ailawadi, and J. W. Holmes, "Model-based design of mechanical therapies for myocardial infarction," *J. Cardiovasc. Transl. Res.*, vol. 4, no. 1, pp. 82–91, 2011.

[42] A. P. Voorhees and H.-C. Han, "A model to determine the effect of collagen fiber alignment on heart function post myocardial infarction.," *Theor. Biol. Med. Model.*, vol. 11, no. Mi, p. 6, 2014.

[43] B. A. Koplan, W. G. Stevenson, and O. N. Cardiovascular, "Ventricular Tachycardia and Sudden Cardiac Death," *Mayo Clin. Proc.*, vol. 84, no. 3, pp. 289–297, 2009.

[44] M. E. Josephson, "Clinical Cardiac Electrophysiology: Techniques and Interpretations," Fourth Edi., Lippincott Williams & Wilkins, 2008, pp. 446–642.

[45] B. Benito and M. E. Josephson, "Ventricular tachycardia in coronary artery

disease.," *Rev. española Cardiol. (English ed.)*, vol. 65, no. 10, pp. 939–55, 2012.

[46] K. F. Decker and Y. Rudy, "Ionic mechanisms of electrophysiological heterogeneity and conduction block in the infarct border zone.," *Am. J. Physiol. Heart Circ. Physiol.*, vol. 299, no. 5, pp. H1588–H1597, 2010.

[47] J. M. de Bakker, F. J. van Capelle, M. J. Janse, S. Tasseron, J. T. Vermeulen, N. de Jonge, and J. R. Lahpor, "Slow conduction in the infarcted human heart. 'Zigzag' course of activation," *Circulation*, vol. 88, no. 3, pp. 915–926, Sep. 1993.

[48] R. Tung, N. G. Boyle, and K. Shivkumar, "Catheter Ablation of ventricular tachycardia," *Circulation*, vol. 123, no. 20, pp. 2284–2288, 2011.

[49] P. Santangeli and F. E. Marchlinski, "Substrate mapping for unstable ventricular tachycardia," *Hear. Rhythm*, vol. 13, no. 2, pp. 569–583, 2016.

[50] H. S. Gillespie, C. C. H. Lin, and J. M. Prutkin, "Arrhythmias in structural heart disease," *Curr. Cardiol. Rep.*, vol. 16, no. 8, p. 510, 2014.

[51] U. Schotten, S. Verheule, P. Kirchhof, and A. Goette, "Pathophysiological mechanisms of atrial fibrillation: a translational appraisal.," *Physiol. Rev.*, vol. 91, no. 1, pp. 265–325, Jan. 2011.

[52] P. a Wolf, R. D. Abbott, and W. B. Kannel, "Atrial Fibrillation as an Independent Risk Factor for Stroke : The Framingham Study," *Stroke*, vol. 22, pp. 983–988, 1991.

[53] R. Tung, E. Buch, and K. Shivkumar, "Catheter ablation of atrial fibrillation," *Circulation*, vol. 126, no. 2, pp. 223–229, 2012.

[54] H. Calkins, K. H. Kuck, R. Cappato, J. Brugada, A. J. Camm, S.-A. Chen, H. J. G. Crijns, R. J. Damiano, D. W. Davies, J. DiMarco, J. Edgerton, K.

Ellenbogen, et al., "2012 HRS/EHRA/ECAS Expert Consensus Statement on Catheter and Surgical Ablation of Atrial Fibrillation: Recommendations for Patient Selection, Procedural Techniques, Patient Management and Follow-up, Definitions, Endpoints, and Research Trial Design: A re," *Europace*, vol. 14, no. 4, pp. 528–606, 2012.

[55] M. Haïssaguerre, P. Jaïs, D. C. Shah, a Takahashi, M. Hocini, G. Quiniou, S. Garrigue, a Le Mouroux, P. Le Métayer, and J. Clémenty, "Spontaneous initiation of atrial fibrillation by ectopic beats originating in the pulmonary veins.," *N. Engl. J. Med.*, vol. 339, no. 10, pp. 659–666, 1998.

[56] E. J. Vigmond, F. Aguel, and N. A. Trayanova, "Computational techniques for solving the bidomain equations in three dimensions," *IEEE Trans. Biomed. Eng.*, vol. 49, no. 11, pp. 1260–1269, 2002.

[57] L. Tung, "A bi-domain model for describing ischemic myocardial dc potentials." Massachusetts Institute of Technology, 1978.

[58] R. H. Clayton, O. Bernus, E. M. Cherry, H. Dierckx, F. H. Fenton, L. Mirabella, A. V. Panfilov, F. B. Sachse, G. Seemann, and H. Zhang, "Models of cardiac tissue electrophysiology: Progress, challenges and open questions," *Prog. Biophys. Mol. Biol.*, vol. 104, no. 1–3, pp. 22–48, 2011.

[59] E. J. Vigmond, R. Weber dos Santos, A. J. Prassl, M. Deo, and G. Plank, "Solvers for the cardiac bidomain equations," *Prog. Biophys. Mol. Biol.*, vol. 96, no. 1–3, pp. 3–18, 2008.

[60] M. Potse, B. Dubé, A. Vinet, and R. Cardinal, "A comparison of monodomain and bidomain propagation models for the human heart," *Annu. Int. Conf. IEEE Eng. Med. Biol. - Proc.*, vol. 53, no. 12, pp. 3895–3898, 2006.

[61] P. J. Basser, J. Mattiello, and D. LeBihan, "Estimation of the effective self-diffusion tensor from the NMR spin echo," *J. Magn. Reson. Ser. B*, vol. 103,

no. 3, pp. 247–254, 1994.

[62] C. Pierpaoli and P. J. Basser, "Toward a quantitative assessment of diffusion anisotropy.," *Magn. Reson. Med.*, vol. 36, no. 6, pp. 893–906, Dec. 1996.

[63] D. Rohmer, A. Sitek, and G. T. Gullberg, "Reconstruction and Visualization of Fiber and Laminar Structure in the Normal Human Heart from Ex Vivo," *Invest. Radiol.*, vol. 42, no. 11, pp. 777–789, 2007.

[64] G. L. Kung, T. C. Nguyen, A. Itoh, S. Skare, N. B. Ingels, D. C. Miller, and D. B. Ennis, "The presence of two local myocardial sheet populations confirmed by diffusion tensor MRI and histological validation.," *J. Magn. Reson. Imaging*, vol. 34, no. 5, pp. 1080–91, Nov. 2011.

[65] H. Jiang, P. C. M. Van Zijl, and J. Kim, "DtiStudio : Resource program for diffusion tensor computation and fiber bundle tracking," vol. 1, pp. 106–116, 2005.

[66] S. Mori and P. C. M. van Zijl, "Fiber tracking: principles and strategies - a technical review.," *NMR Biomed.*, vol. 15, no. 7–8, pp. 468–80, 2002.

[67] F. B. Laun, L. R. Schad, J. Klein, and B. Stieltjes, "How background noise shifts eigenvectors and increases eigenvalues in DTI.," *MAGMA*, vol. 22, no. 3, pp. 151–8, Jun. 2009.

[68] D. K. Jones, "Determining and visualizing uncertainty in estimates of fiber orientation from diffusion tensor MRI.," *Magn. Reson. Med.*, vol. 49, no. 1, pp. 7–12, Jan. 2003.

[69] A. Prakosa, P. Malamas, S. Zhang, F. Pashakhanloo, H. Arevalo, D. A. Herzka, A. Lardo, H. Halperin, E. McVeigh, N. Trayanova, and F. Vadakkumpadan, "Methodology for image-based reconstruction of ventricular geometry for patient-specific modeling of cardiac

electrophysiology," *Prog. Biophys. Mol. Biol.*, vol. 115, no. 0, pp. 226–234, 2014.

[70] E. Ukwatta, H. Arevalo, M. Rajchl, J. White, F. Pashakhanloo, A. Prakosa, D. A. Herzka, E. Mcveigh, A. C. Lardo, N. A. Trayanova, F. Vadakkumpadan, and J. White, "Image-based reconstruction of three-dimensional myocardial infarct geometry for patient-specific modeling of cardiac electrophysiology," *Med. Phys.*, vol. 42, no. 8, pp. 4579–4590, 2015.

[71] F. Vadakkumpadan, H. Arevalo, F. Pashakhanloo, A. Alers, F. Dawoud, K. H. Schuleri, D. Herzka, E. McVeigh, A. C. Lardo, and N. Trayanova, "Estimation of ventricular fiber orientations in infarcted hearts for patient-specific simulations," *Proc. - Int. Symp. Biomed. Imaging*, pp. 636–639, 2013.

[72] F. Pashakhanloo, D. A. Herzka, H. Ashikaga, S. Mori, N. Gai, D. A. Bluemke, N. A. Trayanova, and E. R. McVeigh, "Myofiber Architecture of the Human Atria as Revealed by Submillimeter Diffusion Tensor Imaging," *Circ. Arrhythmia Electrophysiol.*, vol. 9, no. 4, p. e004133, 2016.

[73] M. S. Spach, Wt. Miller, P. C. Dolber, J. M. Kootsey, J. R. Sommer, and C. E. Mosher, "The functional role of structural complexities in the propagation of depolarization in the atrium of the dog. Cardiac conduction disturbances due to discontinuities of effective axial resistivity.," *Circ. Res.*, vol. 50, no. 2, pp. 175–191, 1982.

[74] M. S. Spach, "Anisotropic structural complexities in the genesis of reentrant arrhythmias.," *Circulation*, vol. 84, no. 3, pp. 1447–1450, 1991.

[75] M. Hocini, S. Y. Ho, T. Kawara, A. C. Linnenbank, M. Potse, D. Shah, P. Jais, M. J. Janse, M. Haissaguerre, and J. M. T. de Bakker, "Electrical conduction in canine pulmonary veins: electrophysiological and anatomic correlation," *Circulation*, vol. 105, no. 20, pp. 2442–2448, May 2002.

[76] M. Klos, D. Calvo, M. Yamazaki, S. Zlochiver, S. Mironov, J. Cabrera, D. Sanchez-quintana, J. Jalife, O. Berenfeld, and J. Kalifa, "Atrial Septopulmonary Bundle of the Posterior Left Atrium Provides a Substrate for Atrial Fibrillation Initiation in a Model of Vagally Mediated Pulmonary Vein Tachycardia of the Structurally Normal Heart," *Circ. Arrhythm. Electrophysiol.*, vol. 1, no. 3, pp. 175–183, 2008.

[77] O. Berenfeld, "Frequency-Dependent Breakdown of Wave Propagation Into Fibrillatory Conduction Across the Pectinate Muscle Network in the Isolated Sheep Right Atrium," *Circ. Res.*, vol. 90, no. 11, pp. 1173–1180, May 2002.

[78] S. Y. Ho, D. Sanchez-quintana, J. A. Cabrera, and R. H. Anderson, "Anatomy of the Left Atrium : Implications for Radiofrequency Ablation of Atrial Fibrillation," *J. Cardiovasc. Electrophysiol.*, vol. 10, no. 11, pp. 1525–1534, 1999.

[79] H. Nathan and M. Eliakim, "The junction between the left atrium and the pulmonary veins. An anatomic study of human hearts.," *Circulation*, vol. 34, no. 3, pp. 412–422, Sep. 1966.

[80] S. Y. Ho, R. H. Anderson, and D. Sánchez-Quintana, "Atrial structure and fibres: morphologic bases of atrial conduction.," *Cardiovasc. Res.*, vol. 54, no. 2, pp. 325–36, May 2002.

[81] K. Wang, S. Y. Ho, D. G. Gibson, and R. H. Anderson, "Architecture of atrial musculature in humans.," *Br. Heart J.*, vol. 73, no. 6, pp. 559–65, Jun. 1995.

[82] J. Zhao, T. D. Butters, H. Zhang, A. J. Pullan, I. J. LeGrice, G. B. Sands, and B. H. Smaill, "An image-based model of atrial muscular architecture: effects of structural anisotropy on electrical activation.," *Circ. Arrhythm. Electrophysiol.*, vol. 5, no. 2, pp. 361–70, Apr. 2012.

[83] E. O. Stejskal and J. E. Tanner, "Spin diffusion measurements: spin echoes in the presence of a time-dependent field gradient," *Chem. Phys.*, vol. 42, no. 1, pp. 288–292, 1965.

[84] P. J. Basser, J. Mattiello, and D. Lebihan, "MR diffusion tensor spectroscopy and imaging.," *Biophys. J.*, vol. 66, no. 1, p. 259, 1994.

[85] S. Mori and J. Zhang, "Principles of Diffusion Tensor Imaging and Its Applications to Basic Neuroscience Research," *Neuron*, vol. 51, no. 5, pp. 527–539, 2006.

[86] D. M. Koh and D. J. Collins, "Diffusion-weighted MRI in the body: Applications and challenges in oncology," *Am. J. Roentgenol.*, vol. 188, no. 6, pp. 1622–1635, 2007.

[87] D. E. Sosnovik, R. Wang, G. Dai, T. G. Reese, and V. J. Wedeen, "Diffusion MR tractography of the heart.," *J. Cardiovasc. Magn. Reson.*, vol. 11, no. 1, p. 47, Jan. 2009.

[88] P. A. Helm, L. Younes, M. F. Beg, D. B. Ennis, C. Leclercq, O. P. Faris, E. McVeigh, D. Kass, M. I. Miller, and R. L. Winslow, "Evidence of structural remodeling in the dyssynchronous failing heart.," *Circ. Res.*, vol. 98, no. 1, pp. 125–32, Jan. 2006.

[89] J. Chen, S.-K. Song, W. Liu, M. McLean, J. S. Allen, J. Tan, S. a Wickline, and X. Yu, "Remodeling of cardiac fiber structure after infarction in rats quantified with diffusion tensor MRI.," *Am. J. Physiol. Heart Circ. Physiol.*, vol. 285, no. 3, pp. H946–54, Sep. 2003.

[90] P. A. Helm, H.-J. Tseng, L. Younes, E. R. McVeigh, and R. L. Winslow, "Ex vivo 3D diffusion tensor imaging and quantification of cardiac laminar structure.," *Magn. Reson. Med.*, vol. 54, no. 4, pp. 850–9, Oct. 2005.

[91] H. Lombaert, J.-M. M. Peyrat, P. Croisille, S. Rapacchi, L. Fanton, F. Cheriet, P. Clarysse, I. Magnin, H. Delingette, and N. Ayache, "Human atlas of the cardiac fiber architecture: study on a healthy population.," *IEEE Trans. Med. Imaging*, vol. 31, no. 7, pp. 1436–47, Jul. 2012.

[92] E. W. Hsu, A. L. Muzikant, S. A. Matulevicius, R. C. Penland, and C. S. Henriquez, "Magnetic resonance myocardial fiber-orientation mapping with direct histological correlation," *Am. J. Physiol. Circ. Physiol.*, vol. 274, no. 5, pp. H1627–H1634, 1998.

[93] O. Bernus, A. Radjenovic, M. L. Trew, I. J. LeGrice, G. B. Sands, D. R. Magee, B. H. Smaill, and S. H. Gilbert, "Comparison of diffusion tensor imaging by cardiovascular magnetic resonance and gadolinium enhanced 3D image intensity approaches to investigation of structural anisotropy in explanted rat hearts," *J. Cardiovasc. Magn. Reson.*, vol. 17, no. 1, pp. 1–27, 2015.

[94] R. Wang, T. Benner, A. G. Sorensen, and V. J. Wedeen, "Diffusion Toolkit : A Software Package for Diffusion Imaging Data Processing and Tractography," *Proc. Intl. Soc. Mag. Reson. Med.*, vol. 15, p. 3720, 2007.

[95] J. W. Papez, "Heart musculature of the atria," *Am. J. Anat.*, vol. 27, no. 3, pp. 255–285, 1920.

[96] G. Bachmann, "The inter-auricular time interval," *Am J Physiol*, vol. 41, no. 309, p. 1016, 1916.

[97] P. M. Nielsen, I. J. Le Grice, B. H. Smaill, and P. J. Hunter, "Mathematical model of geometry and fibrous structure of the heart.," *Am. J. Physiol.*, vol. 260, no. 4 Pt 2, pp. H1365–78, Apr. 1991.

[98] A. Hamabe, Y. Okuyama, Y. Miyauchi, S. Zhou, H. N. Pak, H. S. Karagueuzian, M. C. Fishbein, and P. S. Chen, "Correlation between

anatomy and electrical activation in canine pulmonary veins," *Circulation*, vol. 107, no. 11, pp. 1550–1555, 2003.

[99] V. Markides, "Characterization of Left Atrial Activation in the Intact Human Heart," *Circulation*, vol. 107, no. 5, pp. 733–739, Feb. 2003.

[100] B. J. Hansen, J. Zhao, T. A. Csepe, B. T. Moore, N. Li, L. A. Jayne, A. Kalyanasundaram, P. Lim, A. Bratasz, K. A. Powell, O. P. Simonetti, R. S. D. Higgins, et al., "Atrial fibrillation driven by micro-anatomic intramural re-entry revealed by simultaneous sub-epicardial and sub-endocardial optical mapping in explanted human hearts," *Eur. Heart J.*, vol. 36, no. 35, pp. 2390–2401, 2015.

[101] J. Zhao, B. J. Hansen, T. A. Csepe, P. Lim, Y. Wang, M. Williams, P. J. Mohler, P. M. L. Janssen, R. Weiss, J. D. Hummel, and V. V. Fedorov, "Integration of High-Resolution Optical Mapping and 3-Dimensional Micro-Computed Tomographic Imaging to Resolve the Structural Basis of Atrial Conduction in the Human Heart," *Circ. Arrhythmia Electrophysiol.*, vol. 8, no. 6, pp. 1514–1517, 2015.

[102] M. Haissaguerre, M. Hocini, A. Denis, A. J. Shah, Y. Komatsu, S. Yamashita, M. Daly, S. Amraoui, S. Zellerhoff, M. Q. Picat, A. Quotb, L. Jesel, et al., "Driver domains in persistent atrial fibrillation," *Circulation*, vol. 130, no. 7, pp. 530–538, 2014.

[103] S. M. Narayan, D. E. Krummen, K. Shivkumar, P. Clopton, W. J. Rappel, and J. M. Miller, "Treatment of atrial fibrillation by the ablation of localized sources: CONFIRM (Conventional Ablation for Atrial Fibrillation with or Without Focal Impulse and Rotor Modulation) trial," *J. Am. Coll. Cardiol.*, vol. 60, no. 7, pp. 628–636, 2012.

[104] P. Lamata, R. Casero, V. Carapella, S. a Niederer, M. J. Bishop, J. E.

Schneider, P. Kohl, and V. Grau, "Images as drivers of progress in cardiac computational modelling.," *Prog. Biophys. Mol. Biol.*, vol. 115, no. 2–3, pp. 198–212, Aug. 2014.

[105] N. A. Trayanova, "Whole-heart modeling: applications to cardiac electrophysiology and electromechanics.," *Circ. Res.*, vol. 108, no. 1, pp. 113–28, Jan. 2011.

[106] S. Labarthe, J. Bayer, Y. Coudière, J. Henry, H. Cochet, P. Jaïs, and E. Vigmond, "A bilayer model of human atria: mathematical background, construction, and assessment.," *Europace*, vol. 16 Suppl 4, pp. iv21–iv29, Nov. 2014.

[107] G. Seemann, C. Höper, F. B. Sachse, O. Dössel, A. V Holden, and H. Zhang, "Heterogeneous three-dimensional anatomical and electrophysiological model of human atria.," *Philos. Trans. A. Math. Phys. Eng. Sci.*, vol. 364, no. 1843, pp. 1465–81, Jun. 2006.

[108] K. S. McDowell, F. Vadakkumpadan, R. Blake, J. Blauer, G. Plank, R. S. MacLeod, and N. a Trayanova, "Methodology for patient-specific modeling of atrial fibrosis as a substrate for atrial fibrillation.," *J. Electrocardiol.*, vol. 45, no. 6, pp. 640–5, 2012.

[109] M. W. Krüger, *Personalized Multi-Scale Modeling of the Atria*, vol. 19. KIT Scientific Publishing, 2013.

[110] M. J. Gonzales, K. P. Vincent, W.-J. Rappel, S. M. Narayan, and A. D. McCulloch, "Structural contributions to fibrillatory rotors in a patient-derived computational model of the atria.," *Europace*, vol. 16 Suppl 4, pp. iv3–iv10, Nov. 2014.

[111] M. F. Beg, P. A. Helm, E. McVeigh, M. I. Miller, and R. L. Winslow, "Computational cardiac anatomy using MRI.," *Magn. Reson. Med.*, vol. 52,

no. 5, pp. 1167–74, Nov. 2004.

[112] S. Nielles-Vallespin, C. Mekkaoui, P. Gatehouse, T. G. Reese, J. Keegan, P. F. Ferreira, S. Collins, P. Speier, T. Feiweier, and R. Silva, "In vivo diffusion tensor MRI of the human heart: Reproducibility of breath-hold and navigator-based approaches," *Magn. Reson. Med.*, vol. 70, no. 2, pp. 454–465, 2013.

[113] C. Nguyen, Z. Fan, B. Sharif, Y. He, R. Dharmakumar, D. S. Berman, and D. Li, "In vivo three-dimensional high resolution cardiac diffusion-weighted MRI: A motion compensated diffusion-prepared balanced steady-state free precession approach," *Magn. Reson. Med.*, vol. 1267, pp. 1257–1267, 2013.

[114] U. Gamper, P. Boesiger, and S. Kozerke, "Diffusion imaging of the in vivo heart using spin echoes--considerations on bulk motion sensitivity.," *Magn. Reson. Med.*, vol. 57, no. 2, pp. 331–7, Feb. 2007.

[115] D. Mozaffarian, E. J. Benjamin, A. S. Go, D. K. Arnett, M. J. Blaha, M. Cushman, S. R. Das, S. de Ferranti, J. P. Després, H. J. Fullerton, V. J. Howard, M. D. Huffman, et al., *Heart Disease and Stroke Statistics—2016 Update: A Report From the American Heart Association*. 2015.

[116] G. Ertl and S. Frantz, "Healing after myocardial infarction.," *Cardiovasc. Res.*, vol. 66, no. 1, pp. 22–32, Apr. 2005.

[117] G. J. Strijkers, A. Bouts, W. M. Blankesteijn, T. H. J. M. Peeters, A. Vilanova, M. C. van Prooijen, H. M. H. F. Sanders, E. Heijman, and K. Nicolay, "Diffusion tensor imaging of left ventricular remodeling in response to myocardial infarction in the mouse.," *NMR Biomed.*, vol. 22, no. 2, pp. 182–90, Feb. 2009.

[118] M. Pop, N. R. Ghugre, V. Ramanan, L. Morikawa, G. Stanisz, A. J. Dick, and G. a Wright, "Quantification of fibrosis in infarcted swine hearts by ex

vivo late gadolinium-enhancement and diffusion-weighted MRI methods.," *Phys. Med. Biol.*, vol. 58, no. 15, pp. 5009–28, Aug. 2013.

[119] G. L. Kung, O. Ajijola, R. J. Ramirez, J. K. Gahm, W. Zhou, N. Wisniewski, A. Mahajan, A. Garfinkel, K. Shivkumar, and D. Ennis, "Microstructural remodeling in the post-infarct porcine heart measured by diffusion tensor MRI and T1-weighted late gadolinium enhancement MRI," *J. Cardiovasc. Magn. Reson.*, vol. 14, no. Suppl 1, pp. 2–4, 2012.

[120] M.-T. Wu, W.-Y. I. Tseng, M.-Y. M. Su, C.-P. Liu, K.-R. Chiou, V. J. Wedeen, T. G. Reese, and C.-F. Yang, "Diffusion tensor magnetic resonance imaging mapping the fiber architecture remodeling in human myocardium after infarction: correlation with viability and wall motion.," *Circulation*, vol. 114, no. 10, pp. 1036–45, Sep. 2006.

[121] E. X. Wu, Y. Wu, J. M. Nicholls, J. Wang, S. Liao, S. Zhu, C.-P. Lau, and H.-F. Tse, "MR diffusion tensor imaging study of postinfarct myocardium structural remodeling in a porcine model.," *Magn. Reson. Med.*, vol. 58, no. 4, pp. 687–95, Oct. 2007.

[122] S. Zhang, J. A. Crow, X. Yang, J. Chen, A. Borazjani, K. B. Mullins, W. Chen, R. C. Cooper, R. M. McLaughlin, and J. Liao, "The correlation of 3D DT-MRI fiber disruption with structural and mechanical degeneration in porcine myocardium.," *Ann. Biomed. Eng.*, vol. 38, no. 10, pp. 3084–95, Oct. 2010.

[123] J. C. Walker, J. M. Guccione, Y. Jiang, P. Zhang, A. W. Wallace, E. W. Hsu, and M. B. Ratcliffe, "Helical myofiber orientation after myocardial infarction and left ventricular surgical restoration in sheep.," *J. Thorac. Cardiovasc. Surg.*, vol. 129, no. 2, pp. 382–90, Feb. 2005.

[124] C. Mekkaoui, S. Huang, H. H. Chen, G. Dai, T. G. Reese, W. J. Kostis, A.

Thiagalingam, P. Maurovich-horvat, J. N. Ruskin, U. Hoffmann, M. P. Jackowski, and D. E. Sosnovik, "Fiber architecture in remodeled myocardium revealed with a quantitative diffusion CMR tractography framework and histological validation.," *J. Cardiovasc. Magn. Reson.*, vol. 14, no. 1, p. 70, Oct. 2012.

[125] S. Winklhofer, C. T. Stoeck, N. Berger, M. Thali, R. Manka, S. Kozerke, H. Alkadhi, and P. Stolzmann, "Post-mortem cardiac diffusion tensor imaging: detection of myocardial infarction and remodeling of myofiber architecture," *Eur. Radiol.*, pp. 2810–2818, 2014.

[126] M.-T. Wu, M.-Y. M. Su, Y.-L. Huang, K.-R. Chiou, P. Yang, H.-B. Pan, T. G. Reese, V. J. Wedeen, and W.-Y. I. Tseng, "Sequential changes of myocardial microstructure in patients postmyocardial infarction by diffusion-tensor cardiac MR: correlation with left ventricular structure and function.," *Circ. Cardiovasc. Imaging*, vol. 2, no. 1, pp. 32–40, 6 p following 40, Jan. 2009.

[127] J. W. Holmes and J. W. Covell, "Collagen fiber orientation in myocardial scar tissue," *Cardiovasc. Pathobiol.*, vol. 1, no. 1, pp. 15–22, 1996.

[128] D. E. Sosnovik, R. Wang, G. Dai, T. Wang, E. Aikawa, M. Novikov, A. Rosenzweig, R. J. Gilbert, and V. J. Wedeen, "Diffusion spectrum MRI tractography reveals the presence of a complex network of residual myofibers in infarcted myocardium.," *Circ. Cardiovasc. Imaging*, vol. 2, no. 3, pp. 206–12, May 2009.

[129] S. D. Zimmerman, W. J. Karlon, J. W. Holmes, J. H. Omens, and J. W. Covell, "Structural and mechanical factors influencing infarct scar collagen organization.," *Am. J. Physiol. Heart Circ. Physiol.*, vol. 278, no. 1, pp. H194–200, Jan. 2000.

[130] G. M. Fomovsky, A. D. Rouillard, and J. W. Holmes, "Regional mechanics determine collagen fiber structure in healing myocardial infarcts," *J. Mol. Cell. Cardiol.*, vol. 52, no. 5, pp. 1083–1090, 2012.

[131] H. J. Arevalo, F. Vadakkumpadan, E. Guallar, A. Jebb, P. Malamas, K. C. Wu, and N. A. Trayanova, "Arrhythmia risk stratification of patients after myocardial infarction using personalized heart models," *Nat. Commun.*, vol. 7, no. May, p. 11437, 2016.

[132] D. Deng, H. Arevalo, F. Pashakhanloo, A. Prakosa, H. Ashikaga, E. McVeigh, H. Halperin, and N. Trayanova, "Accuracy of prediction of infarct-related arrhythmic circuits from image-based models reconstructed from low and high resolution MRI," *Front. Physiol.*, vol. 6, no. OCT, pp. 1–12, 2015.

[133] S. Zahid, H. Cochet, P. M. Boyle, E. L. Schwarz, K. N. Whyte, E. J. Vigmond, R. Dubois, M. Hocini, M. Haïssaguerre, P. Jaïs, and N. A. Trayanova, "Patient-derived models link reentrant driver localization in atrial fibrillation to fibrosis spatial pattern.," *Cardiovasc. Res.*, p. cvw073–, 2016.

[134] H. Arevalo, G. Plank, P. Helm, H. Halperin, and N. Trayanova, "Tachycardia in post-infarction hearts: insights from 3D image-based ventricular models.," *PLoS One*, vol. 8, no. 7, p. e68872, Jan. 2013.

[135] S. Zahid, K. N. Whyte, E. L. Schwarz, R. C. Blake, P. M. Boyle, J. Chrispin, A. Prakosa, E. G. Ipek, F. Pashakhanloo, and H. R. Halperin, "Feasibility of using patient-specific models and the 'minimum cut' algorithm to predict optimal ablation targets for left atrial flutter," *Hear. Rhythm*, 2016.

[136] V. Y. Wang, P. M. F. Nielsen, and M. P. Nash, "Image-Based Predictive Modeling of Heart Mechanics," *Annu. Rev. Biomed. Eng.*, pp. 351–383, 2015.

[137] S. M. Dillon, M. A. Allessie, P. C. Ursell, A. L. Wit, S. M. Dillon, M. A.

Allessie, P. C. Ursell, and A. L. Wit, "Influences of anisotropic tissue structure on reentrant circuits in the epicardial border zone of subacute canine infarcts SM Dillon, MA Allessie, PC Ursell and AL Wit Circulation Research 1988, 63:182-206," *Circ. Res.*, pp. 182–206, 1988.

[138] R. Mazumder, S. Choi, B. D. Clymer, R. D. White, and A. Kolipaka, "Diffusion Tensor Imaging of Healthy and Infarcted Porcine Hearts: Study on the Impact of Formalin Fixation," *J. Med. Imaging Radiat. Sci.*, vol. 47, no. 1, pp. 74–85, 2016.

[139] R. M. (Brigham and W. John, U. B. (Brigham and W. Tedrow, B. A. (Brigham and W. Koplan, C. M. (Brigham and W. Albert, L. M. (Brigham and W. Epstein, M. O. (Brigham and W. Sweeney, A. L. (Brigham and W. Miller, G. F. (Brigham and W. Michaud, and W. G. (Brigham and W. Stevenson, "Ventricular arrhythmias and sudden cardiac death," *Lancet*, vol. 380, no. 9852, pp. 1520–1529, 2012.

[140] M. J. Janse and A. L. Wit, "Electrophysiological mechanisms of ventricular arrhythmias resulting from myocardial ischemia and infarction.," *Physiol. Rev.*, vol. 69, pp. 1049–1169, 1989.

[141] A. G. Kléber and Y. Rudy, "Basic Mechanisms of Cardiac Impulse Propagation and Associated Arrhythmias," pp. 431–488, 2009.

[142] P. Kellman and A. E. Arai, "Cardiac imaging techniques for physicians: late enhancement.," *J. Magn. Reson. Imaging*, vol. 36, no. 3, pp. 529–42, Sep. 2012.

[143] A. Schmidt, C. F. Azevedo, A. Cheng, S. N. Gupta, D. a Bluemke, T. K. Foo, G. Gerstenblith, R. G. Weiss, E. Marbán, G. F. Tomaselli, J. a C. Lima, K. C. Wu, et al., "Infarct tissue heterogeneity by magnetic resonance imaging identifies enhanced cardiac arrhythmia susceptibility in patients

with left ventricular dysfunction.," *Circulation*, vol. 115, no. 15, pp. 2006–14, Apr. 2007.

[144] S. D. Roes, C. J. W. Borleffs, R. J. Van Der Geest, J. J. M. Westenberg, N. A. Marsan, T. A. M. Kaandorp, J. H. C. Reiber, K. Zeppenfeld, H. J. Lamb, A. De Roos, M. J. Schalij, and J. J. Bax, "Infarct tissue heterogeneity assessed with contrast-enhanced mri predicts spontaneous ventricular arrhythmia in patients with ischemic cardiomyopathy and implantable cardioverter-defibrillator," *Circ. Cardiovasc. Imaging*, vol. 2, no. 3, pp. 183–190, 2009.

[145] A. T. Yan, A. J. Shayne, K. a Brown, S. N. Gupta, C. W. Chan, T. M. Luu, M. F. Di Carli, H. G. Reynolds, W. G. Stevenson, R. Y. Kwong, W. Chan, M. F. Di Carli, et al., "Characterization of the peri-infarct zone by contrast-enhanced cardiac magnetic resonance imaging is a powerful predictor of post-myocardial infarction mortality.," *Circulation*, vol. 114, no. 1, pp. 32–9, Jul. 2006.

[146] H. L. Estner, M. M. Zviman, D. Herzka, F. Miller, V. Castro, S. Nazarian, H. Ashikaga, Y. Dori, R. D. Berger, H. Calkins, A. C. Lardo, and H. R. Halperin, "The critical isthmus sites of ischemic ventricular tachycardia are in zones of tissue heterogeneity, visualized by magnetic resonance imaging.," *Heart Rhythm*, vol. 8, no. 12, pp. 1942–9, Dec. 2011.

[147] L. Ching-Hsing and Y. Rudy, "A Dynamic Model of the Cardiac Ventricular Action Potential Simulations of Ionic Currents and Concentration Changes," *Circulation*, vol. 74, no. 6, pp. 1071–1098, 1994.

[148] H. Arevalo, B. Rodriguez, and N. Trayanova, "Arrhythmogenesis in the heart: multiscale modeling of the effects of defibrillation shocks and the role of electrophysiological heterogeneity," *Chaos An Interdiscip. J. Nonlinear Sci.*,

vol. 17, no. 1, p. 15103, 2007.

[149] Z. Qu, J. N. Weiss, and A. Garfinkel, "Cardiac electrical restitution properties and stability of reentrant spiral waves: a simulation study," *Am. J. Physiol. Circ. Physiol.*, vol. 276, no. 1, pp. H269–H283, 1999.

[150] B. Rodriguez, B. M. Tice, J. C. Eason, F. Aguel, J. M. Ferrero, and N. Trayanova, "Effect of acute global ischemia on the upper limit of vulnerability: a simulation study," *Am. J. Physiol. Circ. Physiol.*, vol. 286, no. 6, pp. H2078–H2088, 2004.

[151] J. Pu and P. A. Boyden, "Alterations of Na+ currents in myocytes from epicardial border zone of the infarcted heart a possible ionic mechanism for reduced excitability and postrepolarization refractoriness," *Circ. Res.*, vol. 81, no. 1, pp. 110–119, 1997.

[152] W. Dun, S. Baba, T. Yagi, and P. A. Boyden, "Dynamic remodeling of K+ and Ca2+ currents in cells that survived in the epicardial border zone of canine healed infarcted heart," *Am. J. Physiol. Circ. Physiol.*, vol. 287, no. 3, pp. H1046–H1054, 2004.

[153] M. Jiang, C. Cabo, J. A. Yao, P. A. Boyden, and G. N. Tseng, "Delayed rectifier K currents have reduced amplitudes and altered kinetics in myocytes from infarcted canine ventricle," *Cardiovasc. Res.*, vol. 48, no. 1, pp. 34–43, 2000.

[154] E. J. Vigmond, M. Hughes, G. Plank, and L. J. Leon, "Computational Tools for Modeling Electrical Activity in Cardiac Tissue," *J. Electrocardiol.*, vol. 36, no. SUPPL., pp. 69–74, 2003.

[155] E. B. Schelbert, L. Hsu, S. A. Anderson, B. D. Mohanty, S. M. Karim, P. Kellman, A. H. Aletras, and A. E. Arai, "Late gadolinium-enhancement cardiac magnetic resonance identifies postinfarction myocardial fibrosis and

the border zone at the near cellular level in ex vivo rat heart.," *Circ. Cardiovasc. Imaging*, vol. 3, no. 6, pp. 743–52, Nov. 2010.

[156] K. H. Schuleri, M. Centola, R. T. George, L. C. Amado, K. S. Evers, K. Kitagawa, A. L. Vavere, R. Evers, J. M. Hare, C. Cox, E. R. McVeigh, J. A. C. Lima, et al., "Characterization of Peri-Infarct Zone Heterogeneity by Contrast-Enhanced Multidetector Computed Tomography. A Comparison With Magnetic Resonance Imaging," *J. Am. Coll. Cardiol.*, vol. 53, no. 18, pp. 1699–1707, 2009.

[157] J. M. de Bakker, F. J. van Capelle, M. J. Janse, A. A. Wilde, R. Coronel, A. E. Becker, K. P. Dingemans, N. M. van Hemel, and R. N. Hauer, "Reentry as a cause of ventricular tachycardia in patients with chronic ischemic heart disease: electrophysiologic and anatomic correlation," *Circulation*, vol. 77, no. 3, pp. 589–606, 1988.

[158] H. Ashikaga, T. Sasano, J. Dong, M. M. Zviman, R. Evers, B. Hopenfeld, V. Castro, R. H. Helm, T. Dickfeld, S. Nazarian, J. K. Donahue, R. D. Berger, et al., "Magnetic resonance-based anatomical analysis of scar-related ventricular tachycardia: Implications for catheter ablation," *Circ. Res.*, vol. 101, no. 9, pp. 939–947, Oct. 2007.

[159] J. J. Fenoglio, T. D. Pham, a H. Harken, L. N. Horowitz, M. E. Josephson, and a L. Wit, "Recurrent sustained ventricular tachycardia: structure and ultrastructure of subendocardial regions in which tachycardia originates.," *Circulation*, vol. 68, no. 3, pp. 518–533, 1983.

[160] J. Fernández-Armenta, A. Berruezo, D. Andreu, O. Camara, E. Silva, L. Serra, V. Barbarito, L. Carotenutto, R. Evertz, J. T. Ortiz-Pérez, T. M. De Caralt, R. J. Perea, et al., "Three-dimensional architecture of scar and conducting channels based on high resolution ce-CMR: insights for

ventricular tachycardia ablation.," *Circ. Arrhythm. Electrophysiol.*, vol. 6, no. 3, pp. 528–37, Jun. 2013.

[161] S. Nayyar, L. Wilson, A. N. Ganesan, T. Sullivan, P. Kuklik, D. Chapman, A. G. Brooks, R. Mahajan, M. Baumert, G. D. Young, P. Sanders, and K. C. Roberts-Thomson, "High-density mapping of ventricular scar: a comparison of ventricular tachycardia (VT) supporting channels with channels that do not support VT.," *Circ. Arrhythm. Electrophysiol.*, vol. 7, no. 1, pp. 90–8, Feb. 2014.

[162] E. J. Ciaccio, J. Coromilas, H. Ashikaga, D. O. Cervantes, A. L. Wit, N. S. Peters, E. R. McVeigh, and H. Garan, "Model of unidirectional block formation leading to reentrant ventricular tachycardia in the infarct border zone of postinfarction canine hearts," *Comput. Biol. Med.*, vol. 62, pp. 254–263, 2015.

[163] S. Nazarian, D. a Bluemke, A. C. Lardo, M. M. Zviman, S. P. Watkins, T. L. Dickfeld, G. R. Meininger, A. Roguin, H. Calkins, G. F. Tomaselli, R. G. Weiss, R. D. Berger, et al., "Magnetic resonance assessment of the substrate for inducible ventricular tachycardia in nonischemic cardiomyopathy.," *Circulation*, vol. 112, no. 18, pp. 2821–5, Nov. 2005.

[164] H. Ashikaga, H. Arevalo, F. Vadakkumpadan, R. C. Blake, J. D. Bayer, S. Nazarian, M. Muz Zviman, H. Tandri, R. D. Berger, H. Calkins, D. a Herzka, N. a Trayanova, et al., "Feasibility of image-based simulation to estimate ablation target in human ventricular arrhythmia.," *Heart Rhythm*, vol. 10, no. 8, pp. 1109–16, Aug. 2013.

[165] J. D. Bayer, C. H. Roney, A. Pashaei, P. Jaïs, and E. J. Vigmond, "Novel radiofrequency ablation strategies for terminating atrial fibrillation in the left atrium: a simulation study," *Front. Physiol.*, vol. 7, no. April, p. 108, 2016.

Vita

Farhad Pashakhanloo was born in Tehran, Iran on March 22, 1986. Farhad received his B.Sc. with a double major in Electrical Engineering and Physics from Sharif University of Technology in 2009. Farhad enrolled at The Johns Hopkins School of Medicine in 2009 to pursue a PhD in Biomedical Engineering. Farhad's PhD research has led to 7 peer-reviewed journal articles and 13 conference abstracts, and has been featured in *Circulation: Arrhythmia and Electrophysiology* and *Heart Rhythm*. During his PhD, Farhad designed and taught an intersession course at The Johns Hopkins University on cardiac imaging and modeling. Farhad was awarded a silver medal in the 2004 International Physics Olympiad and was the recipient of the Best Presentation Award at the Gordon Research Seminar on Cardiac Arrhythmia Mechanisms in 2015.